N d'ordre :42144

UNIVERSITE DE LILLE 1 - SCIENCES ET TECHNOLOGIES

Thèse

pour obtenir le grade de

Docteur de l'Université de Lille 1

Spécialité Microondes et Microtechnologies

Présentée par

Jianping HAO

BROAD BAND ELECTROMAGNETIC PERFECT METAMATERIAL ABSORBERS

Soutenance le 05 Octobre 2016

M. B. Sauviac, Professeur, Université de Saint Etienne, Rapporteur

M. E. Akmansoy, Maître de Conférence, Université de Paris Sud, Rapporteur

Mme. D. Seetharamdoo, Chargée de Recherche, IFSTTAR-LEOST, Examinatrice

M. D. Bourreau, Maître de Conférence, Telecom Bretagne, Examinateur

M. D. Lippens, Professeur, IEMN-Université de Lille, Directeur de thèse

M. E. Lheurette, Professeur, IEMN-Université de Lille, Co-directeur de thèse

M. S. Arscott, Directeur de Recherche CNRS, IEMN-Université de Lille, Invité

M. G. Ducournau, Maître de Conférence, IEMN-Université de Lille, Invité

Résumé

Ce travail de thèse concerne les structures artificielles à base de métamatériaux permettant la réalisation d'absorbants parfaits. Après une brève introduction des métamatériaux, de leur fonctionnement en tant qu'absorbants et de l'état de l'art, quatre types de structures fonctionnant en bandes centimétrique ou millimétrique ont été conçus puis fabriqués à savoir (i) des réseaux de cubes $BaSrTiO_3$ (BST) basés sur les résonances de Mie, (ii) des réseaux désordonnés composés d'anneaux métalliques mettant en jeu des effets de résonance semblables aux systèmes plasmoniques (iii) des absorbants à quatre résonateurs élémentaires sur substrat flexible et (iv) des réseaux multicouches métal-diélectrique de forme pyramidale. Pour l'ensemble, des simulations numériques, corroborées par l'expérience en guide d'onde ou en espace libre, montrent l'existence d'un moment magnétique. Celui-ci est induit par une boucle des courants de déplacement et de conduction. Pour les structures périodiques, les conditions de grande largeur de bande d'absorption ont été établies sur la base du piégeage et de la dissipation de l'énergie incidente. Pour les réseaux désordonnés, il est montré le rôle capital des couplages entre résonateurs. Des structures périodiques à base de ferroélectrique de dimensions sous longueur d'onde ont été assemblées avec succès tandis que des absorbants flexibles ont été réalisés par technique d'impression jet d'encre montrant l'amélioration d'un facteur quatre de la bande d'absorption. Des améliorations comparables ont été obtenues à l'aide de réseaux d'anneaux, dont les positions dans le plan sont désordonnées, résultant de la distribution des fréquences de résonance par effet de couplage fort entre les résonateurs.

Abstract

In this thesis broadband Metamaterial Perfect Absorbers (MPAs) have been investigated. Following a brief introduction of metamaterials, operating mechanisms and state of the art of MPA, four absorber types operating either at centimeter or millimeter wavelengths have been designed and fabricated namely :(i) Mie-resonance based $BaSrTiO_3$ (BST) arrays operating at microwaves, (ii) plasmonic-type disordered ring-shaped MPA, (iii) four patches millimeter wave flexible absorbers (iv) Pyramidal metal/dielectric stacked resonator arrays. For all the structures, it was demonstrated, through numerical modeling, assessed by characterization in a waveguide configuration or in free space, that unit absorbance relies on magnetic resonances induced by a current loop combining displacement and conduction currents. For periodic arrays, the condition for a broad band operation was established via the optimization of dissipation and trapping of electromagnetic energy in the resonators. For disordered metamaterials, it was shown the major role played by the magnetic dipole-dipole interaction. From the technological side, Ferroelectrics cube arrays with subwavelength dimensions were assembled onto a metal plate while flexible multi-resonators periodic arrays were successfully fabricated by ink-jet printing showing a fourfold enhancement of the absorbance bandwidth thanks to the overlapping of resonance frequencies. Comparable improvement in the bandwidth was also pointed out with randomly position metal ring arrays due to the distribution of resonance frequencies that result from tight in-plane resonator coupling

Key words: Metamaterials perfect absorber, Mie-resonance, BST cubes, Plasmonic, Resonators, Pyramid.

Acknowledgements

How time flies! Together with my master training section this is already the fifth year of my studying and living in Lille, the one of the most biggest and beautiful cites in the worldly well-known romantic country. I still clearly remember that when I just landed on this strange land in 2011, everything was so fresh and strongly attracted me. While the reality dramatically dragged me to an embarrassed situation--I could not speak French, the most beautiful language over the world. With generous assistances from these graceful people around me, I finished my 6 month training period, which also makes me addict to the environment, life, colleagues and lovely friends here and firmly decide to come back again for a PhD research. Luckily I got this chance, but gradually I realized in such research level it is full of various challenges. I could not imagine how difficult it would be without the support from professors, colleagues, friends and my family, the forever solid background. I would like to thank all of you for guiding me in the research field and helping me in my daily life.

First and foremost, I would like to express my sincerest gratitude to my promotor, Prof. Dr. Didier Lippens for approving my work in the training session and providing me this PhD opportunity. I am grateful for his endless and patient guidance, which could be found in every discussion and the long emails with explanation in detail and clearly to-do list. His passion and rigorous attitude on the scientific research was deeply impressed me.

Many thanks to my co-promotor Prof. Dr, Eric Lheurette who is not only like a professor but a friend in both my research and my daily life. In the discussions, he could always explain some kind of ‘boring’ stuff in a vivid version. Having lunch together with so many interesting story and French common sense from him made me more love this country and feel a sense of belonging.

I would like to thank Prof. Dr. Ludovic Burgnies and Prof. Dr. Veronique Sadaune for guiding me in the simulation and experimental demonstration,

respectively. Their constant and precious support helped me a lot in my PhD research. I also received a lot of support from our group members:

Thanks to the engineers Guillaume Ducournau, Sylvie Laby, Vanessa Avramovic, Etienne Okada, Colin Mismer and et. al.. who helped me fabricate the sample, built the setup and conducted the experiments. I learnt a lot of practical skills from them which will be surely helpful in my future career.

Thank Malika Habba, Valerie Mikolajczy and et. al. for devoting your time to fix my troubles.

I would like to thank my former master supervisor Prof. Dr. Hou Jianping and Prof. Dr. Zhang Fuli for assisting me to grasp the chance of the master training in Prof. Dr. Didier Lippens' group.

A special section goes to our big chinese group in IEMN: Zhu Tianqi, Gu Sijia, Ding Xiaokun, Weiwei & Zhou Di, Zhang Tianchen, Lin Tianjun, Li Shuo. Chen Shiqi, Xu Tao and et. al.. Thank you all for making me feel like living in a family.

Finally, heartfelt thanks to my family for their endless love and moral support. They always raise me up when I was low. Any of my success contains their devotions and they deserve any of the honors I received. Thanks to my husband, Zhang Jing for encouraging me all the time. I would not focus on my work without his great effort on dealing with all the issues in my life. Thanks to my little girl, Zhang YiXin who bring me so much happy time in the last period of my PhD.

Jiaping HAO
In Lille France
05/10/2016

Contents

List of figures

List of tables

Introduction

Metamaterials are artificial microstructures that exhibit singular properties not found with natural materials. For electromagnetic metamaterials, the most famous property is the possibility to synthesize a composite material whose effective refractive index that can be defined owing to the deep sub-wavelength structuring relevant dimension, is negative. Under this condition, a wave impinging onto a flat interface between a positive/negative index under tilted incidence exhibits a negative refraction The incident wave is transmitted with a negative angle with respect to the incident one. For a flat lens made of a negative index material also called DNG for Double NeGative material, facing a diverging-ray source, this negative refraction leads to a focusing point inside and outside the lens whatever the position of the source. This singular property, namely focusing of electromagnetic waves with a flat lens with uniform negative index was reported theoretically in the seminal article of Veselago in 1968. In practice however, it was in the 2000s that such negative refraction was further studied theoretically by Pendry with the super lens concept and was demonstrated experimentally by Smith et al. For this experimental verification Negative Index Materials (NIMs), operating at microwaves, were fabricated with periodic arrays of continuous or cut wires and the so-called Split Ring Resonators (SRR). It can be shown that the latter ensures a negative effective permeability by exploiting the π phase shift above the resonant frequency. Since these pioneering works, many other 'metadevices' were reported in the literature exploiting the electromagnetic properties of metamaterials and notably the so-called Perfect Metamaterial Absorbers (PMA) that is the main concern of this thesis.

By the term perfect, we mean a device that totally absorbs the incident wave energy and thus without any backscattered and transmitted waves. Such an overall absorption of 100 % can be achieved with conventional technology and notably by using the so-called Dallenbach screen made of natural dielectric material (electric or

magneto-electric material) grounded with a uniform metal plate. For these conventional absorbers, which are widely used in the current systems, it can be shown that their thickness has to fit a quarter wavelength. This design criterion is particularly penalizing for absorber operating in the low frequency part of the microwave spectrum. The drawback of rather thick absorbers has thus motivated to look for solutions making use of metamaterial technology by reminding that their relevant dimensions are very small with respect to the operating wavelength. As a consequence, low profile absorber with ultra-thin dielectric layer can be foreseen with also improvements in terms of weight and conformability.

In addition the fact that metamaterial are made of resonator array has opened the way to enhance absorption properties at a specific resonant frequency even if the background loss sources is small (in practice a loss tangent of a few percent for microwave absorbers dominated by dielectric losses). In counterpart, conventional PMA's absorb in a narrow band. This can be a critical issue notably for radar application systems that require a broad absorbance window. In this context, the main objective of this thesis is to provide solutions to this broadband operation issue targeting also the fabrication of low profile, light weight and flexible absorbers

Towards these goals we will investigate two kinds of technology (plasmonic– and Mie resonance–type) and several solutions notably based on periodic and disordered arrays by according to the following approach:

After a brief introduction where the two technologies and their underlying physical effects are outlined along with a review of the state of the art (chapter 1) Mie resonance based absorbers will be considered in chapter 2. In a first section, millimeter-sized ferroelectric cubes array with a permittivity in excess of 100 will be designed for the achievement of a unit absorbance at centimeter wave length (in practice at X band). Despite the fact that the incident wave is absorbed locally in a long wave length regime, surprisingly in these preliminary studies, it will be shown

that the period of the array plays a major role. Its influence will be clarified on the basis of the balance between the coupling of the incident wave and of the dissipation processes when the energy is trapped in the full dielectric resonators. An experimental assessment, which will be carried out in a wave guide configuration, will demonstrate a unit absorption window in agreement with theoretical prediction. In a second stage we will study the possibility to broaden the band by a distribution of the longitudinal resonator dimension. This solution, termed giant's causeway absorber in this thesis, owing that a 3-D disordered configuration resembles to that of the balsamic stone field in Ireland, is also assessed experimentally by means of free space measurements.

Chapter 3-4 and 5 are devoted to plasmonic PMA's. For broadening the absorbance bandwidth, we first study the effect of position disorder in metal /dielectric/metal layer that will be the generic structures all along these three chapters. By introducing some disorder in the position of resonators, we strengthen their coupling. It results from the magnetic and electric dipole coupling, a distribution of the resonant frequencies and hence an improvement of the absorbance window. These coupling effects, at the origin of the bandwidth enhancement, are illustrated via numerical simulations and experimentally assessed via the measurement of the frequency dependence of the return loss in free space. In Chapter 4, we will investigate how to broaden the transmission window of an absorber operating at W band (75-110 GHz), targeting the realization of flexible perfect absorber at millimeter wave length. Beside this increase in operating frequencies the solution developed here will be to introduce a multi-size basic cell with slightly different resonant dimension, so that the overlap of the absorbance window broadens the absorption spectrum. Here again an experimental assessment in free space will be carried out for PMA fabricated by ink jet printing technologies. This idea of multi-size absorber will be at last investigated numerically in chapter 5 by considering pyramidal–shaped structures designed for the V and W bands. The specificity of the operation of such stacked structure will be illustrated with a sequential energy trapping pointed out in the field

maps plotted in the cross section along the incidence direction.

At last, chapter 6 is very prospective aiming at investigating the technological possibilities recently afforded by the so-called additive technology namely 3D printing. For this preliminary technological study, we chose the example of a wood pile structure whose frequencies cut-off engineering can be used for tailoring the refractive index. Some connections can be established with the development of absorbing metasurfaces notably the possibility to realize ultra-thin meta-device but this is mainly the technological common denominator that are seek.

Chapter 1 Background and context

1.1 Motivations

In this first part, we will point out the motivation of the whole thesis. In recent years, stealth devices have attracted great interest, the stealth devices also called cloak devices is a theoretical or future technology that can make objects invisible by guiding the incident energy around the object to be hidden or with total absorption. The first experimental electromagnetic cloaking of invisibility at microwave frequency was demonstrated by D. Schuring et al. [1], the cloak was constructed according to use of artificially structured metamaterials by using transformation optics method to control the electromagnetic wave [2-3]. Since then, many other groups have reported a large number of works on this topic [4], including a full dielectric cloak device investigated by D. P. Gaillot et al. by employing BST rod working in microwave and terahertz frequency [5].

However, it is well known that the main drawbacks of cloaking devices are (i) their very narrow band, (ii) their difficulty of realization with extreme values of the permittivity and permeability tensors and (iii) their modest result in terms of Scattering Cross Section reduction. This has motivated the so-called ground cloak which permits one to mimic the reflection of flat surface by mirage effects [6].

However the more classical mean for stealth is the use of absorbers which is the conventional solution used up to now in real life application and which will be used all along this thesis.

1.2 Introduction of meta-materials

Metamaterial are artificial structures that extend the range of electromagnetic properties beyond those available in conventional naturally materials. Such kinds of materials are usually made of assemblies of multiple elements at scales that are much

smaller than the wavelength, and exhibit singular dispersion properties such as negative permittivity (ε_{eff}) and permeability (μ_{eff}) [7-9]. Thanks to these beneficial properties, metamaterial can be used to manipulate electromagnetic waves by absorbing, filtering, enhancing or bending waves. As a consequence, extensive potential applications are foreseen as microwave and optical filters, high sensitivity detectors, low profile directive antennas, right- and left handed phase shifters, invisibility cloaks, ultra-thin total absorbers and so on [10-39].

Obviously, ε_{eff} and μ_{eff} are the fundamental parameters which determine the propagation of electromagnetic waves in these artificial composite materials. For metamaterials both effective permittivity and permeability can be negative and the pioneering work on such Double NeGative (DNG) materials was reported by Veselago in 1968 [40]. In this work, Veselago demonstrated that such DNG material exhibits negative refractive index, thus negative phase velocity and named them Left Hand Material (LHM). However at that time there was no materials manifest both negative permittivity and permeability, as it is well known that nature dielectric materials have positive permittivity and permeability, and plasma-type materials exhibit negative permittivity. Until the year 2000, left handed materials were experimentally realized from metallic structures such as periodic arrays of thin metallic wires and open metallic rings (called SRR or Split Ring Resonators) [9, 41-43]. Among these structures, the thin wires gave negative permittivity, and the split rings provided negative permeability. As a kind of renewed artificial materials, metamaterials have been developed rapidly during the two decades. How the realization of metamaterials is one of the most challenging topics, and common metamaterials structure are listed below.

Normally, metamaterials can be realized through several kinds of structures: such as photonic crystal structures [45-49], Transmission line (TL) based structures [50-56], resonant structures [40-44], and full dielectric materials [57-58].

Generally, photonic crystals are composed of dielectrics, metals, superconductor and semiconductor microstructures, periodically arrayed in one-, two- or three dimensions of space. By this periodic structuring, control of electromagnetic wave propagation can be achieved notably by introducing a forbidden band gap in the dispersion band diagram. As pointed out in Ref. 48 photonic crystal structures have pass–bands with parallel or anti parallel configuration of the phase and group velocity and stop- bands.

In Transmission Line (TL) structures, a negative phase velocity regime can also be obtained by loading a conventional printed circuit board TL with series capacitances and shunt inductances. It results from this effective permittivity and permeability simultaneously negative as analytically and experimentally demonstrated by G. Eleftheriades.

Resonant structures involve electric and magnetic resonances. For the latter below the electric plasma resonance frequency, the induced magnetic field (**B**) created by a current loop resulting from the incident magnetic field (H) yields a negative permeability μ ($B = -|\mu|H$). By the same principle, electric resonance structures can provide negative permittivity [7, 44]. Therefore, combining electric and magnetic resonances can give simultaneously both negative permittivity and permeability [9].

1.3 Principle of perfect meta-material absorbers

Perfect metamaterial absorbers (PMA) have attracted great interest due to the fact that they give the possibility to achieve unit absorptivity of electromagnetic wave at desired frequencies by using thin absorbing layers. Since the first experiment demonstration of PMA in 2008 by N. I. Landy et al. [59], this research topic has progressed rapidly from radio frequencies to visible optics, from single band to double band or broadband absorbers. In this section, we will report on the main principles of two kinds of PMA, Mie-resonance based PMA and plasmonic based

PMAA, which are employed all along our works.

1.3.1 Mie-resonance based perfect meta-material absorber

Mie resonance of particles

From the point view of Mie theory, a mathematical and physical theory of scattering particles properties, the scattered 2^m-pole term of the electric and magnetic fields of particle (here we think about an isolated dielectric sphere) can be proposed as follows[59]:

$$a_m = \frac{n\psi_m(nx)\psi_m'(x) - \psi_m(x)\psi_m'(nx)}{n\psi_m(nx)\xi_m'(x) - \xi_m(x)\psi_m'(nx)} \quad 1\text{-}1$$

$$b_m = \frac{\psi_m(nx)\psi_m'(x) - n\psi_m(x)\psi_m'(nx)}{\psi_m(nx)\xi_m'(x) - n\xi_m(x)\psi_m'(nx)} \quad 1\text{-}2$$

Where n is the relative index of dielectric sphere, $x=k_0r_0$, k_0 is the free space wave number, and $\psi_m(x)$ and $\xi_m(x)$ are the Riccati-Bessel functions. The scattering coefficient a_m and b_m indicate the electric and magnetic behaviors of the sphere-shaped scatter. At the lowest order Mie resonance frequency, the sphere exhibits electric and magnetic dipoles. The effective permittivity and permeability of spherical scattering particles with parameters (ε_1, μ_1) embedded periodically in a host medium (ε_2, μ_2) can be written as follows [60, 61]:

$$\varepsilon_{eff} = \varepsilon_1\left(1 + \frac{3\omega_f}{\frac{F(\theta) + 2b_e}{F(\theta) - b_e} - V}\right) \quad 1\text{-}3$$

$$\mu_{eff} = \mu_1 \left(1 + \frac{3\omega_f}{\frac{F(\theta) + 2b_m}{F(\theta) - b_m} - V} \right) \quad 1\text{-}4$$

$$F(\theta) = \frac{2(\sin\theta - \theta\cos\theta)}{(\theta^2 - 1)\sin\theta + \theta\cos\theta} \quad 1\text{-}5$$

where $b_e = \varepsilon_1/\varepsilon_2$, $b_m = \mu_1/\mu_2$, $V = \frac{4}{3}\pi\left(\frac{r_0}{p}\right)^3$, $\theta = k_0 r_0 \sqrt{\varepsilon_2\mu_2}$, V is the volume fraction of the spherical particles, r_0 is the radius of the spherical particles, p is the lattice constant. $F(\theta)$ is a resonant function and can be negative or positive at certain range of θ, which can provide negative permitivity and permeability.

Mie resonance applied in BST cube absorbers

Turning now to the first Mie resonance in BST ($Ba_xSr_{1-x}TiO_3$) cubes with relavite permittivity $\varepsilon_r = 132$, loss tangent $\tan\delta = 0.025$, respectively, it can be pointed out that the ground resonance is magnetic. This is shown in Fig. 1.1 that illustrates the confinement of the H field inside the cube while the electric field contours are wrapped along the H oriented symmetry axis. By means of this resonance, the surface impedance of the metamaterial absorber matches the free space impedance, thus minimizing the reflectance at the first Mie resonance mode around 11 GHz. At the same time putting a metallic plate on the bottom of the BST cube, which cuts off all the transmission waves, from the equation $A = 1\text{-}R\text{-}T$, one can have a unit absorption.

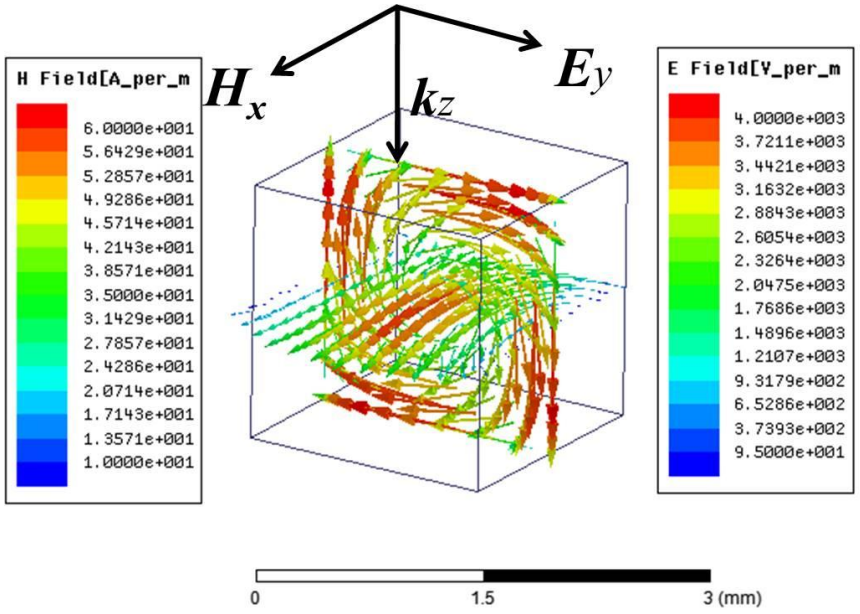

Fig. 1.1 Electric (*y*-*z* plane) and magnetic (*x*-*z* plane) field distributions in a dielectric cube with sidewidth a = 1.8 mm at the first Mie resonance frequency 11.14 GHz.

1.3.2 Plasmonic based perfect meta-material absorber

Throughout the development of the PMA, the plasmonic resonant based PMAs have grown rapidly during the last decade due to the fact that they can possess broadband behaviors and other useful properties for real applications. Most of the PMAs are composed of three layers: (i) periodically metallic structured patterns, (ii) dielectric layer, (iii) continuous metallic plate [62].

The periodically-arranged metallic layers should be carefully designed to provide a certain resonance at the targeted frequency. Fulfilling the impedance matching condition to the free space is achieved by varying the dimensions of the resonators which can have various shapes such as ring, cross, patch, snowflake and so on. Under this impedance matching condition so that reflectivity on the device vanishes and all the incidence EM waves should be coupled to the device.

The second dielectric layer plays a basic role by trapping the incident EM wave. At the resonant frequency of the absorber the EM waves are bouncing back and forth

inside the resonator so that the EM energy is dissipated efficiently. In other words the generic metal-dielectric-metal structure plays a role of resonant cavity with lifetime in the cavity related to frequency selectivity of the resonance through the quality factor.

The primary role of the third metallic layer is to stop any transmission of the impinging wave. Also we will see in the following chapters devoted to plasmonic-type structures that the metallic regions facing the structured top metal layers support backside local currents flowing in the opposite direction to the top ones.

To sum up when an electromagnetic wave is impinging on such a tri-layered medium, the fact that the transmission is zero and the reflection vanishes at the resonance means that all the EM energy is absorbed justifying the term of Perfect Metamaterial Absorber.

1.4 Overview of the state of the art

As aforementioned the first theoretical and experimental demonstration of PMA was reported by Landy et al.. For this work the absorber was composed of three layers [58] with two metallic patterns separated by a dielectric layer. The authors of this article demonstrated a simulated absorptivity near unity at 11.48 GHz [63]. Since this first demonstration, a large number of optimized PMA have been proposed addressing different frequency bands for different application areas. In this last section, a brief overview of the state of the art, summarized in table 1, is reported. While further details can be found in the reference listed in column 1, the second column gives some brief indications about the employed technology, D and M standing for full dielectric and metal respectively. Also the type of metal is specified. One can note that copper is currently used for microwave absorbers whereas the devices that operate in optics are often fabricated with silver or gold layers. The third column indicates the pattern type. When a pyramidal shape is specified this means the stacking of multilayered patches. In the subsequent columns are reported the central frequency (f_c) corresponding generally to the maximum of absorbance and the fractional bandwidth (FB) which is defined by

using the FWHM frequency offset ($\Delta f/f_{c\mathrm{FWHM}}$). The last column gives some indications about sensitivity to the incidence angle (θ) by considering an absorbance in excess of 90 %.

Table 1 Overview of the state of the art of the broadband absorbers.

Reference	Technology	pattern	f_c	$\Delta f/f_c$	Angle sensitivity
[63] D. Feng APL	M-Cu	Pyramid	9.75 GHz	66.7 %	A > 90% θ = 40 ° A > 80% θ = 60 °
[64] Q. Liang Advanced material	M-Cu	Pyramid	7.5 μm	86.7 %	A > 90% θ = 45 ° A > 80% θ = 70 °
[65] J. Yang *Xplore*	M-Cu	Double square loop	4 GHz	80 %	
[66] Y. Cui, APL	M-Au D-Ge	Nanoantennas	10 μm	30 %	
[67] L. Sun, OE	M	Patch Crisscross Ring	12 GHz	92 %	Independent angle
[68] Q. Feng, OL	M-Ni	Cross	32.5 THz	107.7 %	A > 90% θ = 60 °
[69] J. Grant, OL	M-Cu	Cross	5 THz	48 %	A > 90% θ = 80 °
[70] C. Cheng, OE	M-Ag	Disk	3.25 μm	24.6 %	A > 60% θ = 15 °
[71] M. Li *Xplore*	M	Loop	19.8 GHz	92 %	A > 90% θ = 90 °
[72] K. B. Alici, OE	M-Au	Split Ring	205 THz	150.1 %	A > 90% θ = 40 °
[73] K. Aydin Nature C.	M-Ag	Strip (taper)	550 nm	79.6 %	A >90% θ = 70 °
[74] N. R. Han, OE	M-Cu	Split Ring	0.5 THz	79.6 %	
[75] B. X. Wang, IEEE Xplore	M-	Patch (layers)	2.9 THz	42.1 %	A > 90% θ = 50 °
[76] D. H. Kim, OE	D-Si	Pyramid (flexible)	1.23 THz	FWHM: A > 90%: 125.2 %	Bent R = 2 cm
[77] C. Shi, APL	D-Si	Patch	1.5 THz	133.3 %	A > 90% θ = 60 °
[78] Z. Lu, JLT	M-Al	triple-helix array	0.8 μm	142 %	
[79] J. Zhu, APL	M-Cr	Patch (layers)	1.7 THz	135 %	A > 90% θ = 40 °
[11] H. Xiong, APL	M-Cu	Split ring (layers)	14.6 GHz	102 %	
[80] D. Ji, Nature	Ag-SiO_2	Taper (HMM)	4 μm	101 %	
[81] M. R. Soheilifar, Int. J. Electron. Commun.	M-Cu	Split ring	13.5 GHz	111 %	A > 90% θ = 45 °
[82] B. X. Wang,	Al–Si–Mg	Ring	3.35 THz	118 %	A > 90% θ = 90 °

APE					
[83] Y. Yang, Nano Lett.	D-Si	Patch	1550 nm	20 %	θ = 90 °
[84] T. Cao, Science	M-Au	Patch	770 nm	41 %	A > 80% θ = 80 °
[85] B. Y. Wang, JAP	M-Ag	Patch	12 GHz	57.3 %	
[86] B. X. Wang, Phys. Scr.	M-D	Two layers	1.8 THz	33 %	A > 80% θ = 60 °
[87] J. Zhou, Photonics	Au−Al_2O_3	Taper(HMM)	2 μm	75%	
[88] J. Ma, Prog. Electromagn. Res. Lett.		Tree Structure	8.7 GHz	87 %	A > 90% θ = 90 °
[89] M. Lobet, OE	Cu-Ge	Pyramid	3 μm	186 %	A > 90% θ = 75 °

References

[1] D. Shuring, J. J. Mock, B. J. Justice, S. A. Cummer, J. B. Pendry, A. F. Starr and D. R. Smith, Metamaterial electromagnetic cloak at microwave frequency, Science, Vol. 314, 977-980, 2006.

[2] J. B. Pendry, D. Shuring and D. R. Smith, Controlling electromagnetic fields, Science, Vol. 312, 1780-1782, 2006.

[3] D. Shuring, J. B. Pendry, D. R. Smith, Calculation of material properties and ray tracing in transformation media, Opt. Express, Vol. 14, 9794-9804, 2006.

[4] M. Fridman, A. Farsi, Y. Okawachi and A. L. Gaeta, Demonstration of temporal cloaking, Nature, Vol. 481, 62-65, 2012.

[5] D. P. Gaillot, C. Croenne and D. Lippens, An all-dielectric route for terahertz cloaking, Opt. Express, Vol. 16, 3986-3992, 2008.

[6] R. Liu, C. Ji, J. J. Mock, J.Y. Chin, T. J. Cui and D. R. Smith, Broadband ground-plane cloak, Science, Vol. 323, 366-369, 2009.

[7] J. B. Pendry, A. J. Holden, D. J. Robbins, and W. J. Stewart, Magnetism from Conductors, and Enhanced Non-Linear Phenomena, IEEE Trans. Microw. Theory

Tech., Vol.47, 2075-2084, 1999.

[8] D. R. Smith, S. Schultz, P. Markoš, and C. M. Soukoulis, Determination of effective permittivity and permeability of metamaterials from reflection and transmission coefficients, Phys. Rev. B, 65, 195104, 2002.

[9] R. A. Shelby, D. R. Smith and S. Schultz, Experimental verification of a negative index of refraction, Science 292, 77-79, 2001.

[10] F. Capolino, Application of metamaterials, ISBN 978-1-4200-5423-1, 2009.

[11] W. Adams, A. Vora, J. Gwamuri, J. Pearce and D. Güney, Controlling Optical Absorption in Metamaterial Absorbers for Plasmonic Solar Cells, Proc. of SPIE Vol. 9546, 2015.

[12] S. Rudykh and Mary C. Boyce, Transforming wave propagation in layered media via instability-induced interfacial wrinkling, Phys. Rev. Lett., Vol. 112, 034301, 2014.

[13] G. Singh, Rajni, A. Marwaha, A Review of Metamaterials and its Applications, IJETT, Vol.19, 2231-5381, 2015.

[14] J. B. Pendry, Negative Refraction Makes a Perfect Lens, Phys. Rev. Lett., Vol. 85, 18, 2000.

[15] W. Li and J. Valentine, Metamaterial Perfect Absorber Based Hot Electron Photodetection, Nano Lett., Vol. 14, 3510 - 3514, 2014.

[16] A. Vora, J. Gwamuri, N. Pala, A. Kulkarni, J. Pearce and D. Güney, Exchanging Ohmic Losses in Metamaterial Absorbers with Useful Optical Absorption for Photovoltaics, Sci. Rep., Vol. 10, 1038, 2014.

[17] B. Wu, W. Wang, J. Pacheco, X. Chen, T. Grzegorczyk and J. A. Kong, A study of using metamaterial as antenna substrate to enhance gain, PIER, Vol. 51, 295-328, 2005.

[18] S. Enoch, G. Tayeb, P. Sabouroux, N. Guerin and P. Vincent, A metamaterial for directive emission, Phys. Rev. Lett., Vol. 89, 213902, 2002.

[19] W. W. Salisbury, Absorbent body for electromagnetic waves, US Patent, 2599 944, 1952.

[20] W. H. Emerson, Electromagnetic wave absorbers and anechoic chambers through the years, IEEE Trans. Antennas Propag., Vol. 21, 484-490, 1973.

[21] Y. Zhang, R. Mittra, B.-Z. Wang and N.-T. Huang, AMCs for ultra-thin and broadband RAM design, Electron. Lett., Vol. 45, 484-485, 2009.

[23] A. Alù, and N. Engheta, Achieving transparency with plasmonic and metamaterial coatings, Phys. Rev. E, Vol.72, 016623, 2005.

[24] J. B. Pendry, D. Schurig, D. R. Smith, Controlling electromagnetic fields, Science, Vol. 312, 1780-1782, 2006.

[25] A. J. Ward and J. B. Pendry, Refraction and geometry in Maxwell's equations, J. Mod. Opti., Vol. 43, 773-793, 1996.

[26] D. Schurig, J. J. Mock, B. J. Justice, S. A. Cummer, J. B. Pendry, A. F. Starr, and D. R. Smith, Metamaterial Electromagnetic Cloak at Microwave Frequencies, Science, Vol. 314, 977-980, 2006.

[27] A. Alù and N. Engheta, Cloaking and transparency for collections of particles with metamaterial and plasmonic covers, Opt. Express, Vol. 15, 7578-7590, 2007.

[28] A. Alù and N. Engheta, Plasmonic materials in transparency and cloaking problems: mechanism, robustness, and physical insights, Opt. Express, Vol. 15, 3318-3332, 2007.

[29] M. A. Antoniades, and G. V. Eleftheriades, Compact Linear Lead/Lag Metamaterial Phase Shifters for Broadband Applications, IEEE Antennas Wirel.

Propag. Lett., Vol. 2, 103-106, 2003.

[30] E. L. Ginzton, W. R. Hewlett, J. H. Jasburg, and J. D. Noe, Distributed amplification, PIRE, Vol. 36, 956-969, 1948.

[31] C. Caloz, F. P. Casares-Miranda, and C. Camacho-Penalosa, Active Metamaterial Structures and Antennas, IEEE MELECON, 268-271, 2006.

[32] A. Grbic and G. V. Eleftheriades, A backward-wave antenna based on negative refractive index L-C networks, AP-S/URSI, Vol. 4, 340-343, 2002.

[33] L. Lei, C. Caloz, and T. Itoh, Dominant mode leaky-wave antenna with backfire-to-endfire scanning capability, Electron. Lett., Vol. 38, 1414-1416, 2002.

[34] A. Grbic and G. V. Eleftheriades, Experimental verification of backward wave radiation from a negative refractive index metamaterial, J. Appl. Phys., Vol. 92, 5930-5935, 2002.

[35] J. R. James and P. S. Hall, Handbook of Microstrip Antennas. London, U.K. Peter Peregrinus, 1989.

[36] M. Pozar and D. H. Schaubert, Microstrip Antennas: The Analysis and Design of Microstrip Antennas and Arrays, New York: IEEE Press, 1995.

[37] S. Maci, G. Biffi Gentili, P. Piazzesi, and C. Salvador, Dual-band slot-loaded patch antenna, IEE Proc. Microw. Antennas Propag., Vol. 142, 225-232, 1995.

[38] R. Porath, Theory of miniaturized shorting-post microstrip antennas, IEEE Trans. Antennas Propag., Vol. 48, 41-47, 2000.

[39] A. Alù , F. Bilotti, N. Engheta, and L. Vegni, Subwavelength, Compact, Resonant Patch Antennas Loaded With Metamaterials, IEEE Trans. Antennas Propag., Vol. 55, 13-25, 2007.

[40] V. G. Veselago, The electrodynamics of substances with simultaneously negative

values of ε and μ, Sov. Phys. Usp., Vol. 10, 509, 1968.

[41] D. R. Smith, W. J. Padilla, D. C. Vier, S. C. Nemat-Nasser and S. Schultz, Composite Medium with Simultaneously Negative Permeability and Permittivity, Phys. Rev. Lett., Vol.84, 4184, 2000.

[42] J. B. Pendry, A. J. Holden, D. J. Robbins and W. J. Stewart, Magnetism from Conductors, and Enhanced Non-Linear Phenomena, IEEE Trans. Microwave Theory Tech. Vol.47, 2075, 1999.

[43] J. B. Pendry, A. J. Holden, W. J. Stewart and I. Youngs, Extremely Low Frequency Plasmons in Metallic Mesostructures, Phys. Rev. Lett., Vol. 76, 4773, 1996.

[44] C.L. Holloway , E.F. Kuester, J. Baker-Jarvis and P. Kabos, A double negative (DNG) composite medium composed of magnetodielectric spherical particles embedded in a matrix, IEEE Trans. Antennas Propag., Vol. 51, 2596-2603, 2003.

[45] B. Seo, T. Ueda, T.Itoh and H. Fetterman, Isotropic left handed material at optical frequency with dielectric spheres embedded in negative permittivity medium, Appl. Phys. Lett., Vol. 88, 161122, 2006.

[46] A. Rennings, C. Caloz and I. Wolff, A Novel Clustered Dielectric Cubes Metamaterial (CDC-MTM), IEEE AP-S/URSI, 483-486, 2006.

[47] J. D. Shumpert, W. J. Chappell and L.P. B. Katehi, Parallel-plate mode reduction in conductor-backed slots using electromagnetic bandgap substrates, IEEE Trans. Microw. Theory Tech., Vol. 47, 2099-2104, 1999.

[48] J. B. Pendry, L. Martin-Moreno and F. J. Garcia-Vidal, Mimicking surface plasmons with structured surface, Science, Vol. 305, 847-848, 2004.

[49] J. D. Baena, J. Bonache, F. Mart ń, R. M. Sillero, F. Falcone, T. Lopetegi, M. A. G. Laso, J. Garc á–Garc á, I. Gil, M. F. Portillo and M. Sorolla,

Equivalent-circuit models for split-ring resonators and complementary split-ring resonators coupled to planar transmission lines, IEEE Trans. Microw. Theory Tech., Vol. 53, 1451-1461, 2005.

[50] C. Caloz, H. Okabe, T. Iwai, and T. Itoh, Transmission line approach of left-handed (LH) materials, IEEE AP-S/URSI., Vol. 1, 39, 2002.

[51] G. V. Eleftheriades, A. K. Iyer and P. C. Kremer, Planar negative refractive index media using periodically L-C loaded transmission lines, IEEE Trans. Microw. Theory Tech., Vol. 50, 2702-2712, 2002.

[52] A. Grbic and G. V. Eleftheriades, Periodic analysis of a 2-D negative refractive index transmission line structure, IEEE Trans. Antennas Propag., Vol. 51, 2604-2611, 2003.

[53] C. Caloz, Dual composite right/left-handed (D-CRLH) transmission line metamaterial, IEEE Microw. Wirel. Compon. Lett., Vol. 16, 585-587, 2006.

[54] S. Lim, C. Caloz and T. Itoh, Fellow, IEEE, Metamaterial-based electronically controlled transmission-line structure as a novel leaky-wave antenna with tunable radiation angle and beam width, IEEE Trans. Microw. Theory Tech., Vol. 52, 2678-2690, 2004.

[55] R. S. Kshetrimayum, L. Zhu, Guided-wave characteristics of waveguide based periodic structures loaded with various FSS strip layers, IEEE Trans. Antennas Propag., Vol. 53, 120-124, 2005.

[56] Q. Zhao, J. Zhou, F. Zhang, D. Lippens, Mie resonance-based dielectric metamaterials, Mater. Today, Vol. 12, 2009.

[57] C. Vandenbem and J. Vigneron, Mie resonances of dielectric spheres in face-centered cubic photonic crystals, J. Opt. Soc. Am. A, Vol. 22, 1042-1047, 2005.

[58] N. I. Landy, S. Sajuyigbe, J. J. Mock, D. R. Smith and W. J. Padilla, Perfect Metamaterial Absorber, Phys. Rev. Lett., Vol. 100, 207402, 2008.

[59] Jackson, J. D., Classical Electrodynamics, 2nded., Wiley, New York, USA, 1999.

[60] Zhao, Q., et al., Experimental Demonstration of Isotropic Negative Permeability in a Three-Dimensional Dielectric Composite, Phys. Rev. Lett., Vol. 101, 027402, 2008.

[61] Q. Zhao, J. Zhou, F. Zhang, D.r Lippens, Mie resonance-based dielectric metamaterials, Mater. Today, Vol. 12, No 12, 2009.

[62] C. M. Watts, X. Liu and W. J. Padilla, Metamaterial electromagnetic wave absorber, Adv. Mater., Vol. 24, 98-120, 2012.

[63] F. Ding, Y. Cui, X. Ge, Y. Jin and S. He, Ultra-broadband microwave metamaterial absorber, Appl. Phys. Lett., Vol. 100, 103506, 2012.

[64] Q. Liang, T. Wang, Z. Lu, Q. Sun, Y. Fum and W. Yu, Metamaterial-based Two Dimensional Plasmonic Subwavelength Structures Offer the Broadest Waveband Light Harvesting, Adv. Opti. Mater., Vol. 1, 43-49, 2013.

[65] J. Yang and Z. Shen, A Thin and Broadband Absorber Using Double-Square Loops, IEEE Antennas Wirel. Propag. Lett., Vol. 6, 388-391, 2007

[66] Y. Cui, J. Xu, K. Fung, Y. Jin, A. Kumar, S. He, and N. X. Fang, A thin film broadband absorber based on multi-sized nanoantennas , Appl. Phys. Lett., Vol. 99, 253101, 2011.

[67] L. Sun, H. Cheng, Y. Zhou and J. Wang, Broadband metamaterial absorber based on coupling resistive frequency selective surface, Opt. Express, Vol. 20, 4675 2012.

[68] Q. Feng, M. Pu, C. Hu and X. Luo, Engineering the dispersion of metamaterial surface for broadband infrared absorption, Opt. Lett., Vol. 37, 2133, 2012.

[69] J. Grant, Y. Ma, S. Saha, A. Khalid and D R. S. Cumming, Polarization insensitive, broadband terahertz metamaterial absorber, Opt. Lett., Vol. 36, 3476, 2011.

[70] C. Cheng, M. Abbas, C. Chiu, K. Lai, M. Shih and Y. Chang, Wide-angle polarization independent infrared broadband absorbers based on metallic multi-sized disk arrays, Opt. Express, Vol. 20, 10376, 2012.

[71] M. Li, S. Xiao, Member IEEE, Y.Bai and B. Wang, Member, IEEE, An Ultrathin and Broadband Radar Absorber Using Resistive FSS, IEEE Antennas Wirel. Propag. Lett., Vol. 11, 748-751, 2012.

[72] K. Alici, A. Turhan, C. Soukoulis and Ekmel Ozbay, Optically thin composite resonant absorber at the near-infrared band: a polarization independent and spectrally broadband configuration, Opt. Express, Vol. 19, 14260-14267, 2011.

[73] K. Aydin, V. Ferry, R. Briggs and H. Atwater, Broadband polarization-independent resonant light absorption using ultrathin plasmonic super absorbers, Nat. Commun., Vol. 10, 1038, 2011.

[74] N. R. Han, Z. C. Chen, C. S. Lim, B. Ng, and M. H. Hong, Broadband multi-layer terahertz metamaterials fabrication and characterization on flexible substrates, Opt. Express, Vol. 19, 6990-6998, 2011.

[75] B. Wang, L. Wang, G. Wang, W. Huang, X. Li and X. Zhai, Theoretical Investigation of Broadband and Wide-Angle Terahertz Metamaterial Absorber, IEEE Photon. Technol. Lett., Vol. 26, 111-114, 2014.

[76] D. Kim, D. Kim, S. Hwang and J. Jang, Surface relief structures for a flexible broadband terahertz absorber, Opt. Express, Vol. 20, 16815-16822, 2012.

[77] C. Shi, X. Zang, Y. Wang, L. Chen, B. Cai and Y. Zhu, A polarization-independent broadband terahertz absorber, Appl. Phys. Lett., Vol. 105, 031104, 2014.

[78] Z. Lu, M. Zhao, Z. Yang, L. Wu and P. Zhang, Helical Metamaterial Absorbers:

Broadband and polarization-Independent in Optical Region, J. Lightw. Technol., Vol. 31, 2762-2768, 2013.

[79] J. Zhu, Z. Ma, W. Sun, F. Ding, Q. He, L. Zhou and Y. Ma, Ultra-broadband terahertz metamaterial absorber, Appl. Phys. Lett., Vol. 105, 021102 , 2014.

[80] H. Xiong, J. Hong, C. Luo and L. Zhong, An ultrathin and broadband metamaterial absorber using multi-layer structures, Appl. Phys. Let., Vol. 114, 064109, 2013

[81] M. Soheilifar, R. Sadeghzadeh, Design fabrication and characterization of stacked layers planar broadband metamaterial absorber at microwave frequency, J. Electron. Commun., Vol. 69, 126-132, 2015.

[82] B. Wang, L. Wang, G. Wang, W. Huang, X. Li and X. Zhai, A simple design of a broadband, polarization-insensitive and low-conductivity alloy metamaterial absorber, Appl. Phys. Express, Vol. 7, 082601, 2014.

[83] Y. Yang, W. Wang, P. Moitra, I. Kravchenko, D. Briggs and J. Valentine, Dielectric Meta-Reflect array for Broadband Linear Polarization Conversion and Optical Vortex Generation, Nano Lett., Vol. 14, 1394-1399, 2014.

[84] T. Cao, C. Wei, R. Simpson, L. Zhang and M. Cryan, Broadband Polarization-Independent Perfect Absorber Using a Phase-Change Metamaterial at Visible Frequencies, Sci. Rep., Vol. 10, 1038, 2014.

[85] B. Wang, S. Liu, B. Bian, Z. Mao, X. Liu, B. Ma and L. Chen, A novel ultrathin and broadband microwave metamaterial absorber, J. Appl. Phys. Vol. 116, 094504, 2014.

[86] B. Wang, L. Wang, G. Wang, W. Huang and X. Zhai, Broadband polarization-insensitive and wide-angle terahertz metamaterial absorber, Phys. Scr. Vol. 89, 115501, 2014.

[87] J. Zhou, A. Kaplan, L. Chen and L. Guo, Experiment and Theory of the Broadband

Absorption by a Tapered Hyperbolic Metamaterial Array, ACS Photonics, Vol. 1, 618−624, 2014.

[88] J. Ma, W. Tong, K., X. Cao and B. Gong, A Broadband Metamaterial Absorber Using Fractal Tree Structure, Prog. Electromagn. Res. Lett., Vol. 49, 73-78, 2014.

[89] M. Lobet, M. Lard, M. Sarrazin, O. Deparis and L. Henrard, Plasmon hybridization in pyramidal metamaterials: a route towards ultra-broadband absorption, Opt. Express, Vol. 22, 12678-12690, 2014.

Chapter 2 Ferroelectrics based perfect absorbers

2.1 Introduction

Ferroelectric materials, such as $BaTiO_3$ (BTO), $Pb(Zr,Ti)O_3$ (PZT), $SrBi_2Ta_2O_9$ (SBT), and $LiNbO_3$ (LNO), have attracted much interest owing of their applications in many domains including high density capacitors, high-density dynamic random access memory (DRAM), non-volatile ferroelectric random access memory (FRAM), and high frequency devices such as varactors, frequency multipliers, delay lines, filters, oscillators, resonators and tunable microwave devices [1-7]. Among these ferroelectric materials, BTO-based films with Sr doping, namely $Ba_{1-x}Sr_xTiO_3$ (BST) are the essential components for wide spectrum applications, especially for electric field response components and devices, such as phase shifter [8-9], varactors [10], antenna [11], accelerator [12], cloaking [13] and so on because of its high dielectric constant, reasonable dielectric loss, high tunability, and large breakdown strength [14-29].

Thanks to a high permittivity, BST particles, normally cubes with subwavelength scale are able to support strong resonances based on Mie scattering theory. In Ref [32], after firstly reporting on basic Mie scattering theory, a PMA with absorption up to unity, by using BST cubes, was reported by Xiaoming et al.. Meanwhile, resonant frequency tunability with respect to the size was investigated as well in this literature. Following this work, further studies were reported on the parameters dependence of the absorption characteristics of BST and especially the coupling behavior between BST cubes. Lately by exploiting the coupling phenomena, F. Zhang et al. demonstrated a mechanically stretchable tunable PMA around 410 MHz by means of adjusting the interspacing between two dielectric resonators and hence shifting the resonant frequency [33].

In this chapter, we investigate how to use ferroelectric matematerials with a high

relative permittivity, which exhibits isotropic electromagnetic characteristics, to realize broadband perfect absorbers. Towards these goals, based on the principle of surface impedance matching of ferroelectric cubes, we firstly arrayed the ferroelectric $BaSrTiO_3$ (BST) cubes onto a metal ground plane to get a near unit absorption at Mie resonance frequency. This 2D periodic array of dielectric cubes exhibits a magnetic and electric activity that cancels the reflectivity by impedance matching whereas a backside metal plane stops the transmitted wave. In a second stage, we exploit a distribution of the longitudinal dimension namely the height of BST cubes while retaining the transverse periodic arrangement to realize a broadband perfect absorber. Finally, we propose to introduce some position disordering of BST cubes, by thus varying the coupling between the elementary resonators. A significant broadening of the absorbance window band can be pointed out significantly with an experimental verification carried out for all the three stages considered in this chapter.

2.2 BST periodic array single band perfect absorber

2.2.1 Design of the periodic absorbing layers

The design of the meta-material absorber consists of a ferroelectric high permittivity cube array interfaced, in its experimental version, by a thin (0.2 mm) dielectric layer with low permittivity (ε_r = 3.3), while a metallic substrate is employed to prevent transmission. These cubes are structured in the transverse directions in square array at a sub-wavelength scale. A schematic of the structure and of the basic cell are shown in Fig.2.2.1. The ferroelectric material used for the cubes is BST with a barium concentration of 50 % and a MgO doping of 15 wt. % [34]. The side length of the cubes is 1.8 mm (see Reference [35]). The BST material has a complex permittivity of 132(1 - 0.015i). By considering a size on a millimeter scale one can expect that the relevant Mie resonance frequencies should be located in the X (8-12 GHz) and Ku

(12-18 GHz) bands.

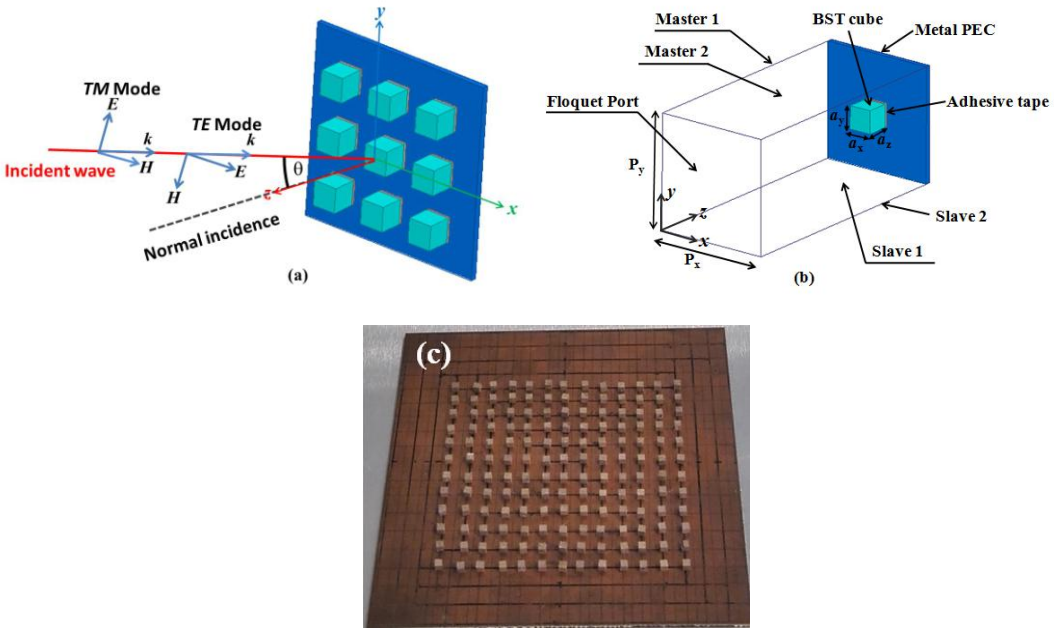

Fig.2.2.1 Schematic layout of (a) the metamaterial absorber with illustration of the *TE* and *TM* polarization modes of the incident wave and the definition of incidence angle (b) The basic unit cell with its characteristic parameters and the simulation conditions (c) Photograph of the periodic BST 2D array.

The commercial software HFSS by Ansys was used to perform the full-wave simulation reported in this work. We set incident plane - wave normal to the absorber surface, namely transmission along *z* axis. As indicated in Fig.2.2.1 (b) Floquet port and Master-Slave periodic boundary conditions were used in the simulation. Considering that the metallic substrate totally blocks all the transmitted wave, the absorbance of the resonator array can be expressed as $A = 1-|S_{11}|^2$. Fig.2.2.2 shows the simulation results of reflection (in red color) and absorption (in black color) spectra with normal incident wave impinging onto an 2D BST cube array arranged on a thin metal plate with a 0.2 mm-thick dielectric spacer layer. Two absorption peaks are pointed out in the frequency range of interest, located at 12.4 GHz and 16.8 GHz, respectively. The first resonance at around 12 GHz with an absorbance close to unit is much stronger than that at higher frequency (around 17 GHz).

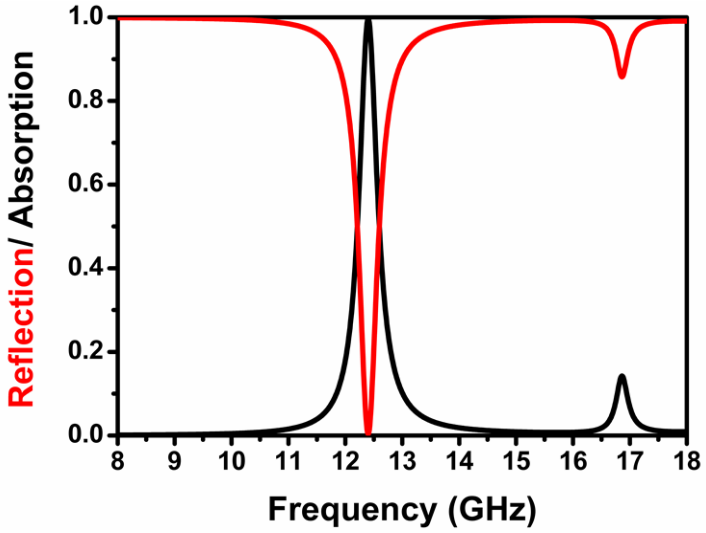

Fig.2.2.2 Reflection and absorption spectra for an absorber with BST cube array with period $P_x = P_y =$ 9mm and side length $a_x = a_y = a_z = 1.8$ mm on a 0.2 mm-thick dielectric layer and a metal substrate.

The *E* and *H* vector for these two resonant peaks (cut plane) at the center of the cubes are illustrated in Fig.2.2.3 (*E* vector on the upper and *H* vector on the bottom panel). For the first resonance, a current loop which results from the displacement current wrapping around the *H* incidence *x* axis can be noticed. Meanwhile a magnetic dipole that corresponds to the ground Mie-type magnetic resonance is induced. On the *x*-*z* plane, an elongation of the magnetic dipole can be noticed. This is the signature of magnetic dipole coupling effect more sensitive for this direction [35]. The second resonance is consistent with an electrical response as assessed by the creation of an electrical dipole on the *y*-*z* plane and the ring-shaped pattern in *H* field contours. For both resonances, strong electric field confinement can be seen in the spacer layer as a result of the continuity of the displacement vector *D*. The large difference in the relative permittivity between the ferroelectric layer ($\varepsilon_r \sim 100$) and the spacer layer ($\varepsilon_r \sim 3$) explains this accumulation. Owing to more pronounced absorption effect at around 12 GHz, in the following, we will focus our attention on the magnetic resonance.

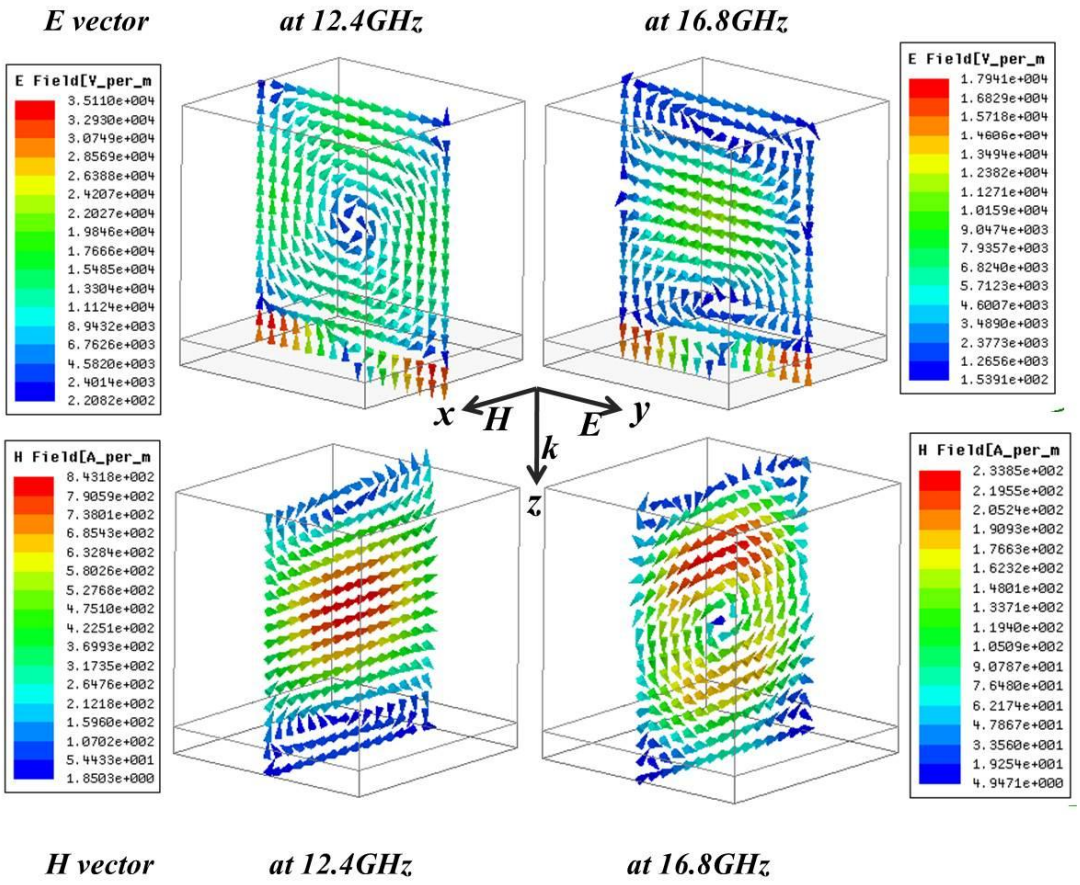

Fig.2.2.3 E and *H* vector recorded for the two resonance peaks at the center of the cubes, respectively.

For more comprehensive understanding of these array effects, the dispersion characteristic as a function of the in plane *k* vector ($k_{//}$) was investigated by employing eigenmode solver of HFSS. The dispersion diagram for the eigenmodes in the first Brillouin zone with p = 9 mm is shown in Fig.2.2.4. The highly localized modes, which correspond to the quasi-flat dispersion branches, were found in agreement with scattering parameters calculation, i.e., for the magnetic resonance at around 12 GHz and for the electric one around 16 GHz. For each localized states corresponds one direction (x, y or z) of the magnetic field. The waves propagating in the vicinity of the metal layer corrugated via the BST cube array (black square symbols) show a typical surface wave characteristic. The corresponding dispersion branch is tangent in the lower frequency part of the spectrum to the light cone (plotted in dotted yellow line). From Fig.2.2.4, it can be noted that surface mode wave couples to one of the highly

localized modes as evidenced via the anti-crossing apparent for reduced k value close to 0.8π for p = 9 mm.

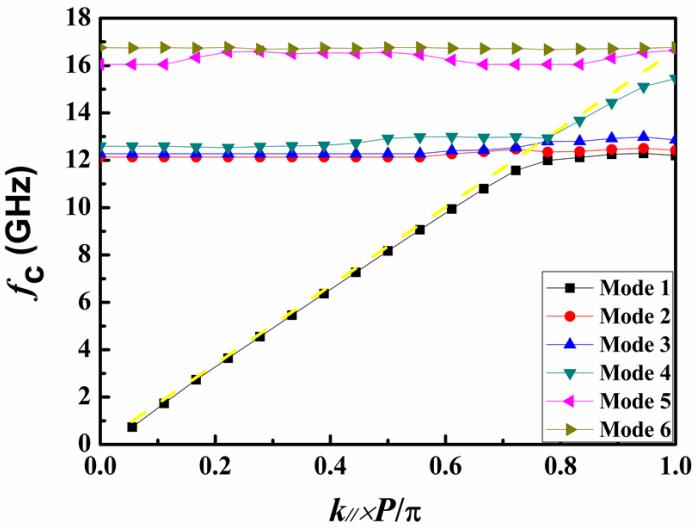

Fig.2.2.4 Dispersion characteristic for BST array absorber with p = 9 mm. Highly localized eigen-states of the BST magnetic resonator are square in light blue, rose, and orange symbols around the magnetic travelling surface wave (in dark blue square symbol). The black dot line represents the propagating wave.

2.2.2 Influence of material properties

For the material side, the most dominant properties are the complex relative permittivity namely the loss tangent (tanδ) and the real part of permittivity (ε_r) of the BST cube, which are the primary source of loss in the microwave frequency band considered in this section.

As well known a resonant cavity being on resonance has to satisfy the condition of a phase is multiple of π or the effective cavity length (lifetime) is a whole number times of half of the wavelength. Because the electrical length is directly related to the dielectric constant, a variation of the relative permittivity will induce a phase offset and as a consequence a shift of resonant frequency. Such expected permittivity dependence of the resonance frequency is verified numerically as shown in Fig.2.2.5 (a), with resonant frequencies decreasing as the dielectric constant increases.

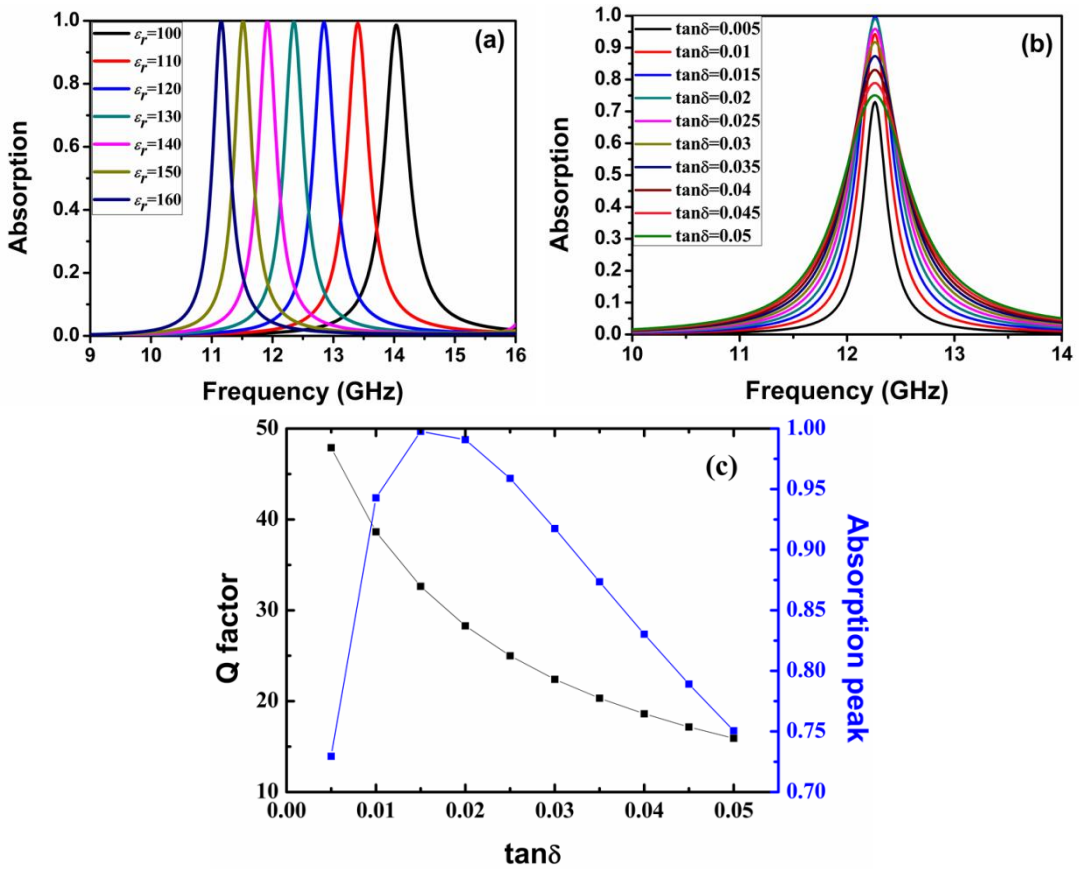

Fig.2.2.5 Absorption spectra for BST cube array with side length = 1.8 mm and period = 9 mm, interfaced with a 0.2 mm-thick dielectric with a metal plate(infinite conductivity) for BST permittivity varying from 100 to 160 (a), for BST loss tangent varying from 0.005 to 0.05 (b), (c) FWHM and Q factor dependence as a function of tanδ.

We reproduce here the principal result, shown as in Fig.2.2.5 (b) the absorption spectra versus loss tangent varying from 0.005 to 0.05, which is quite counter-intuitive because it highlights a trade-off on the tangent loss value with an optimized tanδ equals to 0.015. Fig.2.2.5 (c) shows the Q factor dependence as a function of tanδ. It can be seen that the quality factor reduces when tanδ increase owing to a broadening of the full width at half maximum. With respect to the absorption peak, the absorbance experiences first an increase and reaches the maximum up to unit for loss tangent around 1.5 % that would correspond to the so called critical coupling, when the coupling quality factor equals the loss quality factor (Q_{loss}) = 1/tanδ. Afterwards it drops to ~ 0.75 when tanδ = 0.5% with a maximum FWHM. Thus the optimal value in

the loss tangent of the dielectric system pointed out in Fig.2.2.5 (b) is a direct consequence of a trade-off between the quality of the resonance, which enhances the overall absorbance (A) around the resonance frequency, and the amount of intrinsic loss.

Similar behavior is also found for plasmonic resonator systems in Ref.37, in which the final absorption is engineered by varying the wave attenuation via the decay time constant and the maximum absorption is achieved once the dielectric loss is equal to the wave radiation time.

2.2.3 Influence of geometry

From the geometrical point of view, several parameters are expected to play important roles in the determination of the characteristic of absorption window including resonant frequency, the absorbance, FWHM and the coupling behavior between/among neighboring BST cubes. In this section, we mainly investigate the influence from the geometric parameters of BST and the period of array. But firstly a dielectric space layer which actually is not essential in the ideal case but was required in the practical test is studied.

1. Influence of the thickness *d* of the dielectric spacer

In this section, we consider the thickness (*d*) of the low permittivity spacer between the BST cube array and the backside metallic plane. Ideally the spacer layer is not a necessity in the perfect absorber structure, especially for the typical plasmonic type absorber. But let us remind that, from a practical point of view, a thin adhesive layer is needed to fix the BST cubes onto the metal substrate layer in the experiment. Since the metal layer considered as a perfect reflector, in the case of a close contact between the BST resonator and metal plate, the electric resonant current will be reflected at the interface which by means enlarger the resonator and results in a frequency hop to shorter side. In the simulation, we assume that a polyimide-type thin

spacer layer with a typical complex permittivity of 3.3 (1-0.02i) is sandwiched between the BST cube and the substrate metal layer.

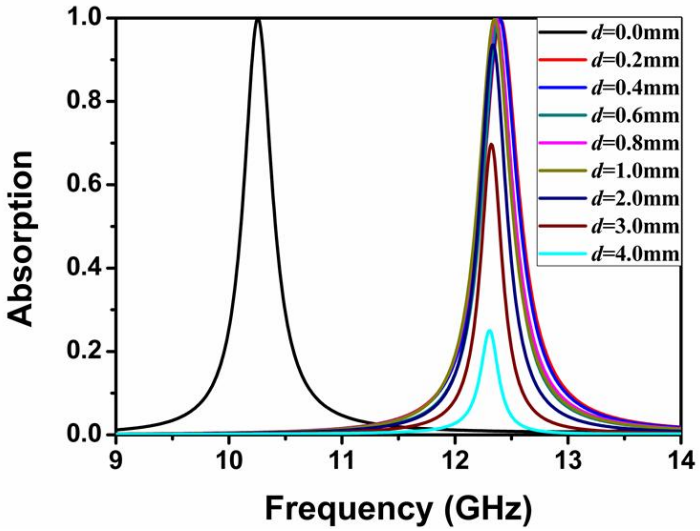

Fig.2.2.6 Influence on the absorption by a dielectric spacer with thickness *d* varying from 0 mm to 4 mm, with BST permittivity equal to 132(1-0.02i), *P* equals to 9 mm.

Fig.2.2.6 shows the absorption with respect of the thickness *d* ranging from 0 to 4 mm. It can be noticed that a significant resonance shift of about 2 GHz occurs when a thin dielectric space is introduced, with respect to the response of the absorber with no spacer. For the zero *d* configuration, one can see from *E* vector distribution in Fig.2.2.7 (upper contour diagram) that the presence of the metal plate directly in contact with BST cubes modifies the current loop in a half circle pattern in the propagation direction. From mirrored images considerations, it results a virtual larger size cube, which explains the frequency shift to lower frequency. In contrast, for finite value of *d*, only slightly resonance frequency shift can be evidenced but keep the same maximal absorptions.

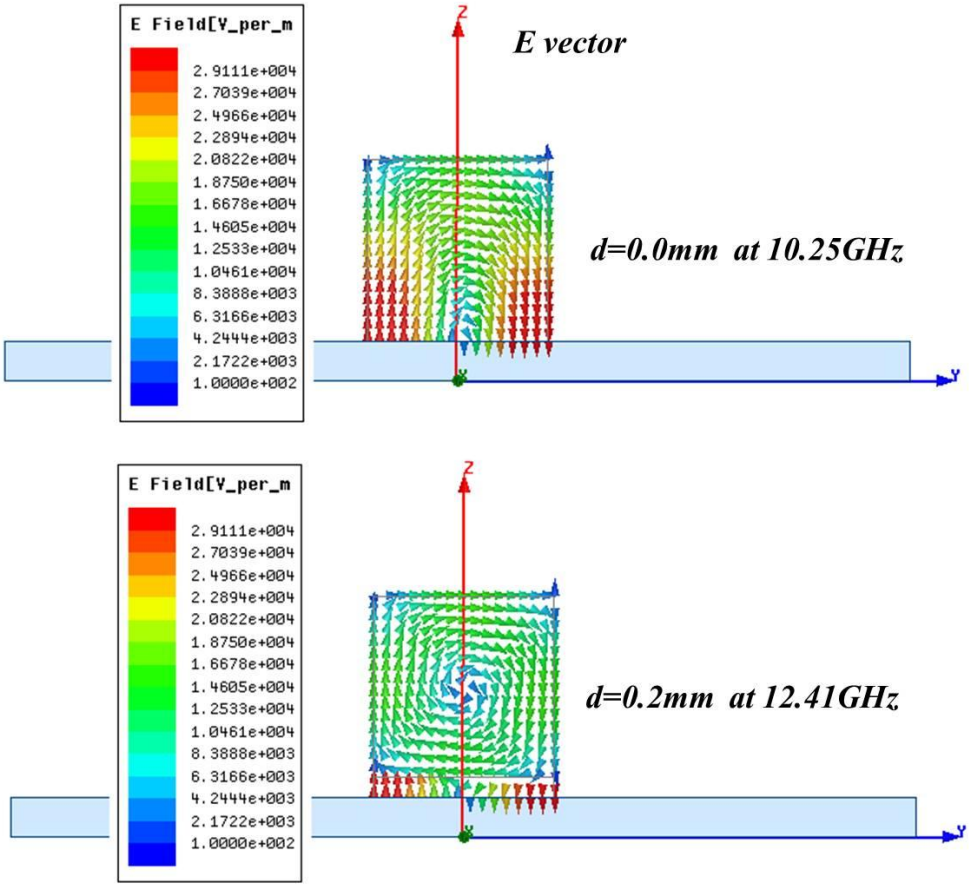

Fig.2.2.7 *E* vector distribution in BST cubes with d = 0.0 mm and d = 0.2 mm in *y*-*z* plane, respectively.

Regarding the maximum of the absorption, it decreases rapidly when the spacer layer is thicker than 1.0 mm. Fig.2.2.8 shows the field maps for the various spacer thicknesses, one can see that the magnetic field is well confined inside of the cube bedded with a 1 mm spacer layer, corresponding to the maximum of absorption. With a thicker spacer layer, the confinement of magnetic field decreases dramatically as depicted in Fig.2.2.8. That is to say, in real designing, the dielectric space layer can't be too thick to keep the unit absorption.

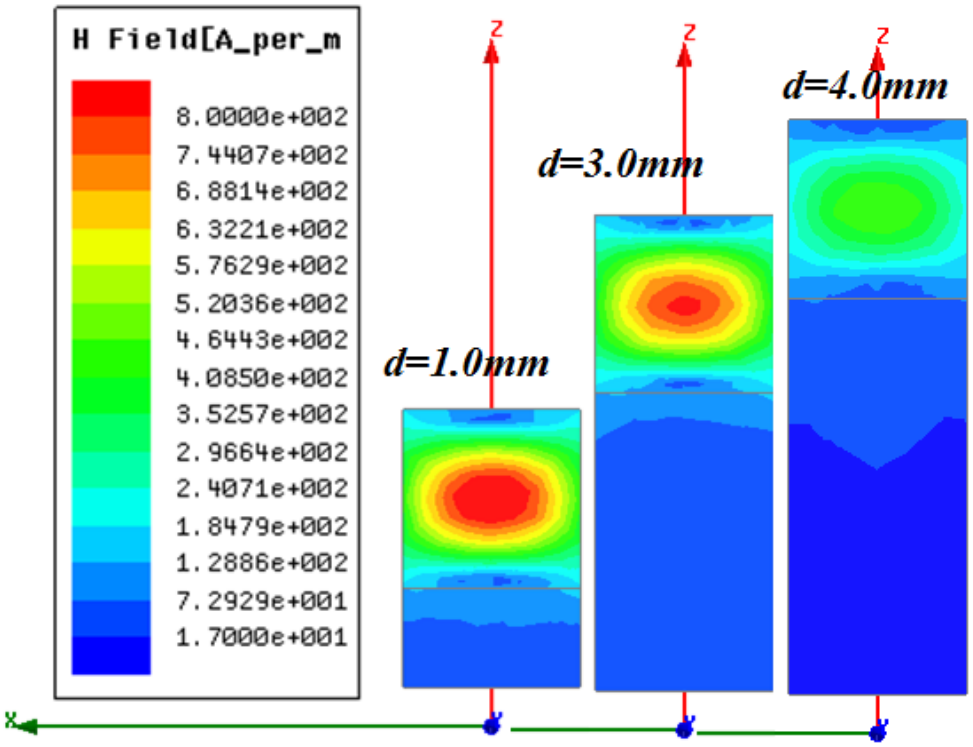

Fig.2.2.8 H field map in *x*-*z* plane with *d* = 1.0 mm, 3.0 mm and 4.0 mm at resonance frequency, respectively.

In conclusion, the virtual size, or effective size of the resonator is actually enlarged by the reflection effect at the BST and metal interface, which thus results in a lower resonant frequency, while a spacer layer is introduced in the structure, the current will forms a closed loop inside BST and resonate at higher frequency. Meanwhile a thicker spacer layer will weaken the confinement in the resonator and hence the absorbance. Similar behaviors were also found for SRR-type metamaterial absorbers [37].

Another way to analyze the mechanisms involved in the absorption process at the resonance (~ 12 GHz) is to consider the first Mie magnetic resonance in a BST cube. The second mechanism is the discontinuity induced by the interface of the BST and spacer layer. Here, two conditions have to be considered, one is total reflection by the metallic plate and the other is partial reflection/transmission. Thus together with the perfect reflected metal layer, the spacer acts as an asymmetric Fabry-Perot cavity. Multiple reflections can be constructive or destructive at the interface of cube/air

according to the spacer thickness [38]. As a last comment, let us mention that although the use of sticking tape for fixing the BST induces a certain frequency hop, it does not degrade the absorption if the tape is not too thick comparing with the dimension of BST cubes.

2. Influence of the BST cube size *a*

In order to hit the target working frequency, as well known, permittivity and size of BST cubes directly determine the resonance frequency, BST size in *x*, *y*, and *z* namely a_x, a_y, a_z are simulated as the condition in Fig.2.2.1 (b) with TE_{01} wave exciting *E* along *y* direction. The results are displayed in Fig.2.2.9. With a_x, a_y, a_z increases, the resonance frequency decreases gradually.

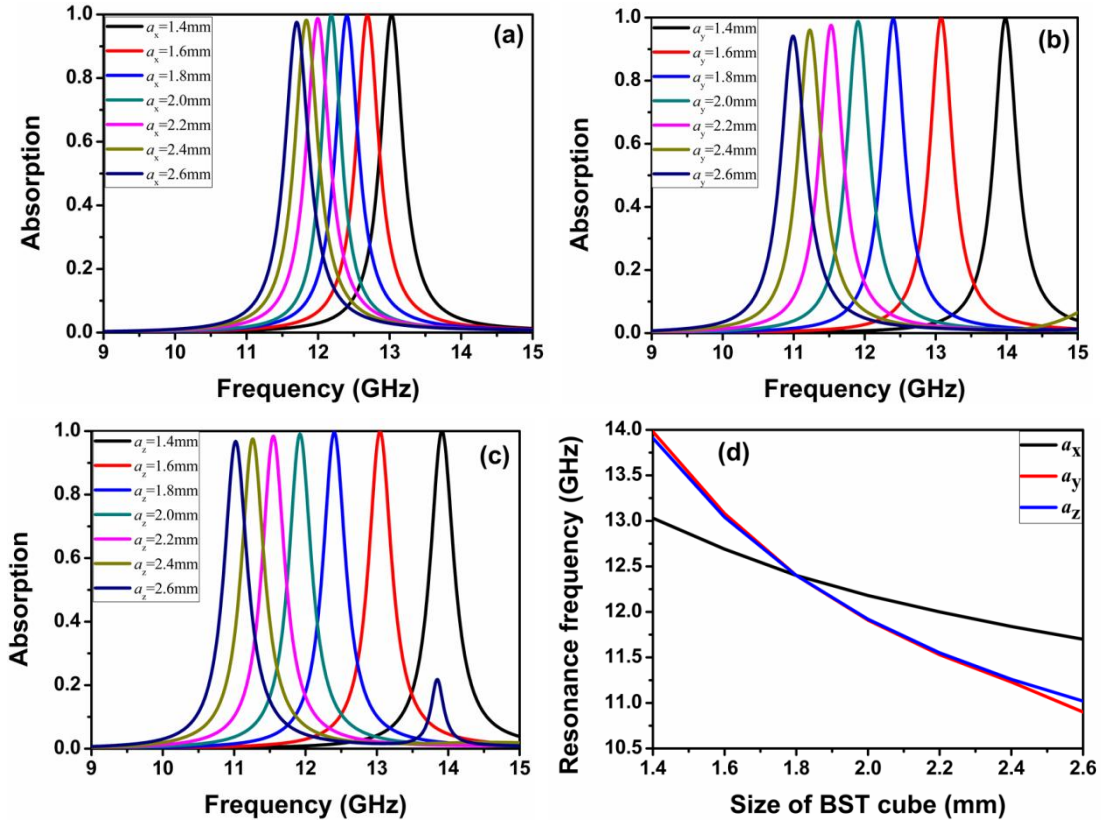

Fig.2.2.9 Influence on the absorption by BST size a_x (a), a_y (b), a_z (c) varying from 1.4 mm to 2.6 mm, with BST permittivity equal to 132(1- 0.02i), *P* equals to 9 mm, (d) resonance frequency dependence of BST size.

3. Influence of the periodicity *P*

In this section, we consider the influence of the period via coupling effect. In order to illustrate such array effect, a period dependence of the absorbance is plotted in Fig.2.2.10.

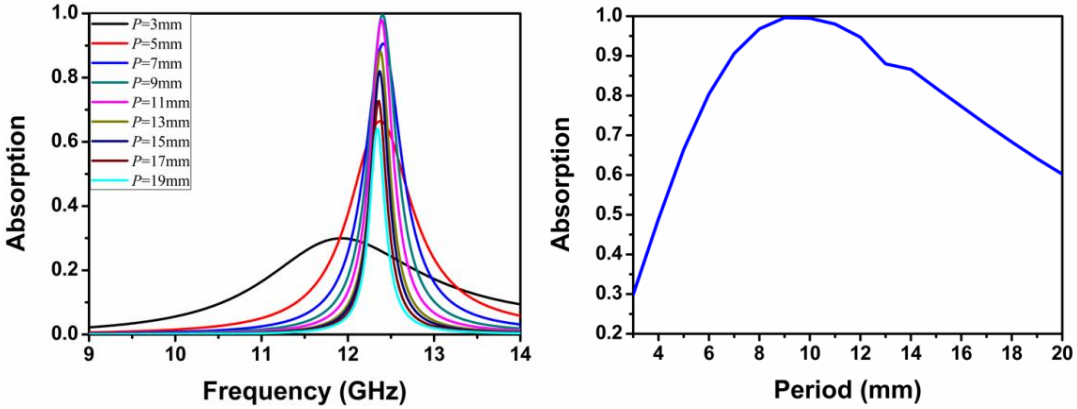

Fig.2.2.10 Influence of the period of the BST cubes ($a_x = a_y = a_z = 1.8$ mm) array ($p = p_x = p_y$) on the absorption spectra for p varying from 3 mm to 19 mm. Maximum of absorbance versus the array period is plotted in the left.

The results displayed in Fig.2.2.10 show unambiguously that the resonance frequency and the peak absorption along with spectral broadening characterized by the Full Width at Half Maximum (FWHM) are strongly dependent on periodicity, or on array effect. As shown in Fig.2.2.10 (a), for the period of $p = 3$ mm, which corresponds to an interspacing of 1.2 mm among cubes, a significant frequency shift from 11.9 GHz to 12.4 GHz is evidenced numerically. The lower frequency shift can be explained by the coupling effect between adjacent BST cubes. Generally optimized period for instance $p = 9$ mm as shown in Fig.2.2.10 (b) that is relatively large comparing to the size of resonators, is adopted and interaction between the resonators is weak enough to be neglected, thus localized mode in the resonant unit cells are mainly contributing to total absorption. If the distance between resonators gets closer the coupling strength can be enhanced and even become dominant. As a consequence, the resonant strength and frequency vary since the effective size of resonator is increased. As mentioned in

previous section, a tunable absorber can be realized by changing the dielectric constant of the interface between free space and absorber, while here the coupling phenomenon provides the other possibility for tuning by mechanically varying the pitch of the resonator array [33]. The coupling effect is also involved in Ref. 35 for bare cubes array. Fig.2.2.10 (b) however shows that concerning the peak absorbance variation with respect to the period, the maxima is relatively flat with a relatively wide band of around 1 mm, allowing a tolerance in fabrication.

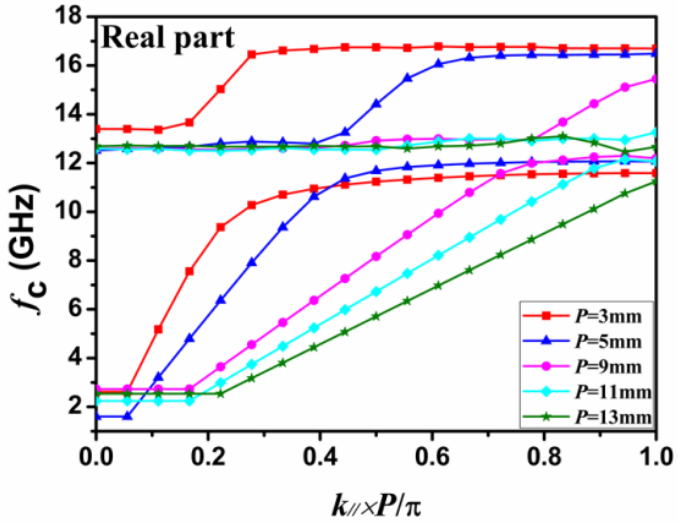

Fig.2.2.11 Dispersion characteristics versus the in plane vector of various periods.

From the real angular frequency versus wave vector characteristics shown in Fig.2.2.11, the anti-crossing between the propagating wave and the localized states corresponding respectively to the magnetic and electrical resonance of the cubes can be pointed out. The position of the anti-crossing depends on the frequency of the localized state and effective dielectric constant of BST array related to period. By enlarging the period, the density of BST array decreases and as a consequence the average or the effective dielectric constant drops, resulting in a lower slop for the propagating waves and hence an anti-crossing closed to the edge of the first Brillouin zone.

To have a more comprehensive understanding of the optimum period, we make a comparison between peak absorbance and Q factor at resonance. And the results are

displayed in Fig.2.2.12, (a) maximum absorption as function of period, (b) Q factor as function of frequency, for loss tangent varying ranging 0.005 to 0.05.

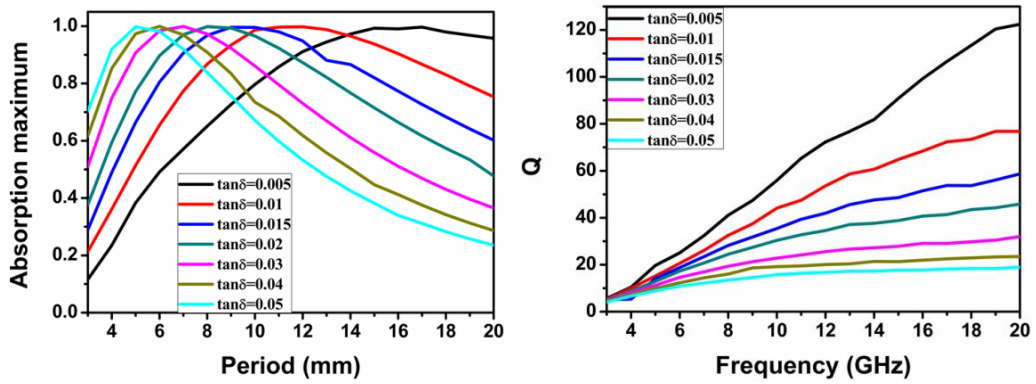

Fig.2.2.12 (a) Maximum absorption as a function of period, (b) Q factor as a function of frequency, for loss tangent ranging from 0.005 to 0.05.

As shown in Fig.2.2.12 (a), for BST with lower loss tangent, larger period is needed for optimized absorption and the related curve has a much broader peak, which greatly improves the tolerance in arranging the BST array. On the other hand the dissipation Q factor is inversely proportional to loss tangent. Once the coupling balances the resonant loss of the localized mode, the so-called critical coupling condition [36] is satisfied with consequently a maximum absorption. In this context a high Q factor may be helpful for achieving high absorption but at the detriment of a narrow absorption window by reminding that broadband absorption is welcome in most practical use. This illustrates the trade-off between high tolerance and wider absorption band.

2.2.4 Incidence angle and polarization analysis

In this present part, we report the isotropy and the polarization influence of the absorbers. The incident angle, *TE* and *TM* modes are defined on the Fig.2.2.1 (a), they correspond to a polarization direction of the electric field or the magnetic field perpendicular to the plane of incidence. Floquet ports and master-slave periodic boundaries were used shown as in Fig.2.2.1 (b). Different from the experimental

demonstration that a pure signal with certain polarization is impinged onto the testing absorber perpendicularly, in the practical use, the polarization and incident angle of the incoming wave are generally unknown. So a perfect absorber which is insensitive to polarization and incident angle is desired. The absorption spectra as a function of frequency are displayed in Fig.2.2.13 for incidence angle θ ranging from 0^o to 75^o for *TE* (a) and *TM* (b) modes, respectively.

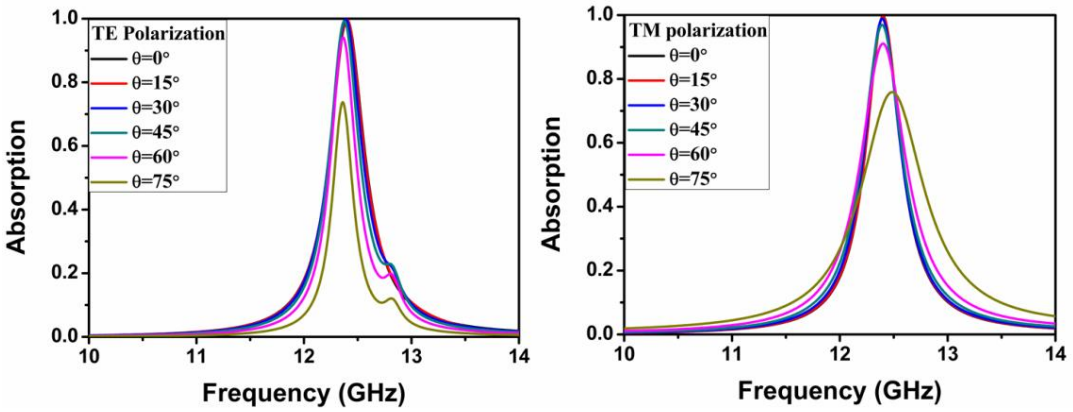

Fig.2.2.13 Absorption spectra as function of frequency for incidence angle θ ranging from 0^o to 75^o for *TE* (a) and *TM* (b) modes, respectively.

As shows in Fig.2.2.13, the 2D BST absorber could keep a high absorption above 90 % even if the incident wave is up to 60 degree with respect to the absorber surface. Moreover, thanks to a symmetric shape of the individual BST cube and the same period along two orthogonal directions, *TE* and *TM* polarizations shows the same response. It can also be pointed out that the resonant frequency has a weak sensitivity to the incident angle except for *TM* mode only 0.3 GHz shift for $\theta = 75^o$, which can be expected by reminding that absorption takes place around the magnetic Mie resonance frequency. On this basis, intrinsically isotropic properties are achieved owing to the displacement current loop responsible for magnetic induction. Under these conditions, one can expect slight variation in the relevant dimensions involved in the resonance process.

For *TM* mode, the increase of the resonance frequency can be understood from a k// increases with h, which gives a slight higher resonance frequency according to the

dispersion diagram. For this polarization condition, the incident magnetic field is always parallel to BST cube array. Also, qualitatively, when θ increases, the transverse component of the *k* vector increases with thus a lower ratio between the parallel wavelength and the cube size. For *TE* polarization, the magnetic Mie resonances can be induced by the two components of the magnetic field ($H_{\perp}$ and $H_{/\!/}$, respectively). Therefore, the incident wave interacts with the cube via the two H components with thus a lower reflectivity for the *TE* mode with respect to the *TM* one. The result that the reflection coefficient shows a minimum value could be explained by the relative importance of the absorption mechanisms via the transverse and perpendicular H components, respectively.

2.2.5 Experimental verification

A Measurement in X and Ku band wave guide

To satisfy the energy conservation principle which has to be verified for absorbance calculation, we use a hollow waveguide configuration and hence a close system to facilitate the energy balance. In practice we thus compare the reflection coefficient of a uniform metal plate with and without a BST cube put the end of the waveguide section Since the target resonant frequency is predicted by the simulation to be at ~12 GHz which is at the edges of X-band and Ku-band, in practice, the experimental assessment was performed both in X-band (22.86 × 10.16 mm^2) and Ku-band (15.799 × 7.899 mm^2) rectangular hollow waveguides.

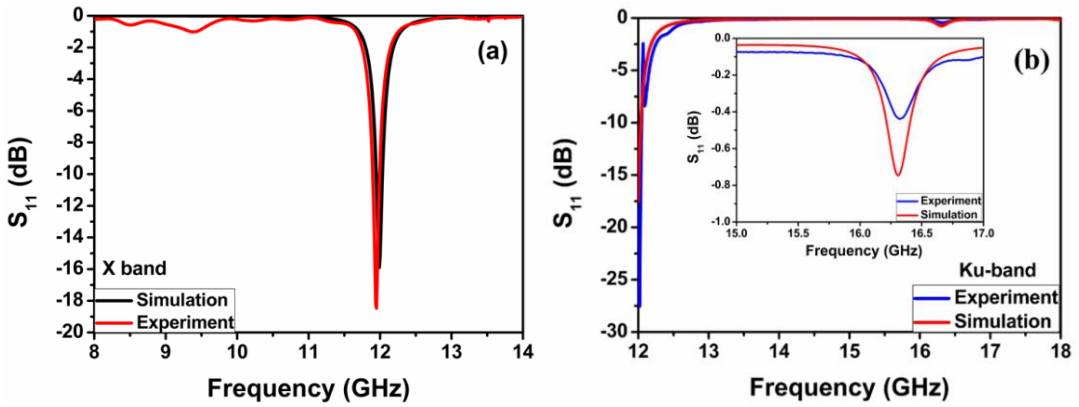

Fig.2.2.14 shows the S_{11} spectra obtained in the test, (a) measured in X band wave guide, (b) measured in Ku band wave guide, insert is the zoomed view of S_{11} parameters from 15 to 17 GHz.

In the first test, a BST cube with side length of 1.8 mm was placed at the center of a 2 mm-thick aluminum plate which afterwards is fixed on the output port of the waveguide. Because of the high reflection from aluminum and by neglecting the scattering loss and leakage, we can measure the reflected energy and calculate the absorption by Eq. $A = 1 - |S_{11}|^2$. Like the reflection spectra shown in Fig.2.2.14 (a), the experimental result agrees relative well with simulation. Additionally, the test in Ku band also verified the resonance at 12 GHz together with electrical resonance at higher frequency ~16.5 GHz shown in Fig.2.2.14 (b), agreeing relative well with simulation result in Fig.2.2.2.

For the next step, the coupling between the BST cubes was investigated using an X-band wave guide. One has to notice that, the incident wave distribution differs from the one in free space with a TE_{10} dominant mode. With such restriction in mind, we focused our attention on the coupling effects illustrated in the previous sections, here for dimer that offers a simpler test-bed for assessing coupling effects. Therefore, the experiment was conducted with two BST cubes in close proximity on a 2 mm-thick aluminum plate. The separation distance between the two cubes is given between their centers either in the magnetic field direction (*PH*) or in the electric field direction (*PE*) as depicted in Fig.2.2.15. At last, let us mention that post-experiment simulations were conducted for a hollow waveguide configuration and hence PEC boundary conditions

are employed to mimic the metal side walls.

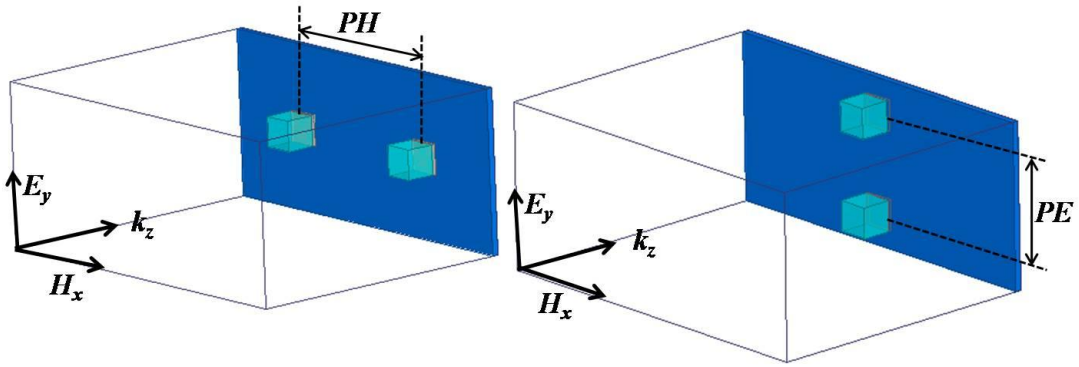

Fig.2.2.15 Schematic of the hollow metal waveguide configuration for assessing the coupling effect between two cubes (a = 1.8mm), *PH* and *PE* definition.

Fig.2.2.16 shows the comparison between experiment (a) and simulation (b) for two BST cubes with different pitches along *PH*. However the absorbance and the exact resonant frequency show some difference which stems from the experimental error in the measurement and the imperfect shape of the BST due to the fabrication tolerance.

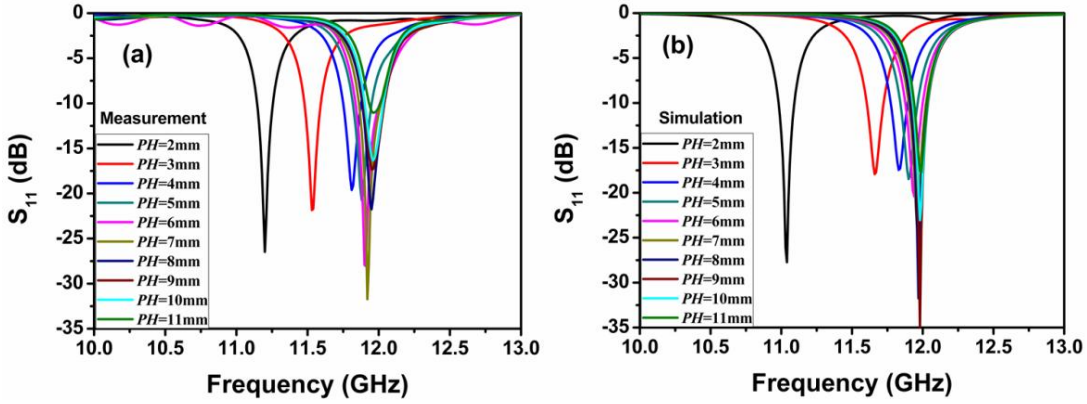

Fig.2.2.16 Simulated and experimental reflection spectra for BST cubes dimer when varying *PH* ranging from 2 mm to 11 mm.

Fig.2.2.17 depicts the field distribution in the BST cubes, (a) *E* vector in the center of one cube in *y*-*z* plane and *H* vector in the center of the cubes in *x*-*z* plane for *PH* = 2 mm, (b) *E* vector in the center of one cube in *y*-*z* plane and *H* vector in the center of the cubes in *x*-*z* plane for *PH* = 6 mm. One can see that when the cubes are in close vicinity, they strongly interact with each other, operating as one bigger BST cube

and thus the resonant frequency is relatively low as verified by the S_{11} spectra while with a larger pitch, the cubes independently confine the field.

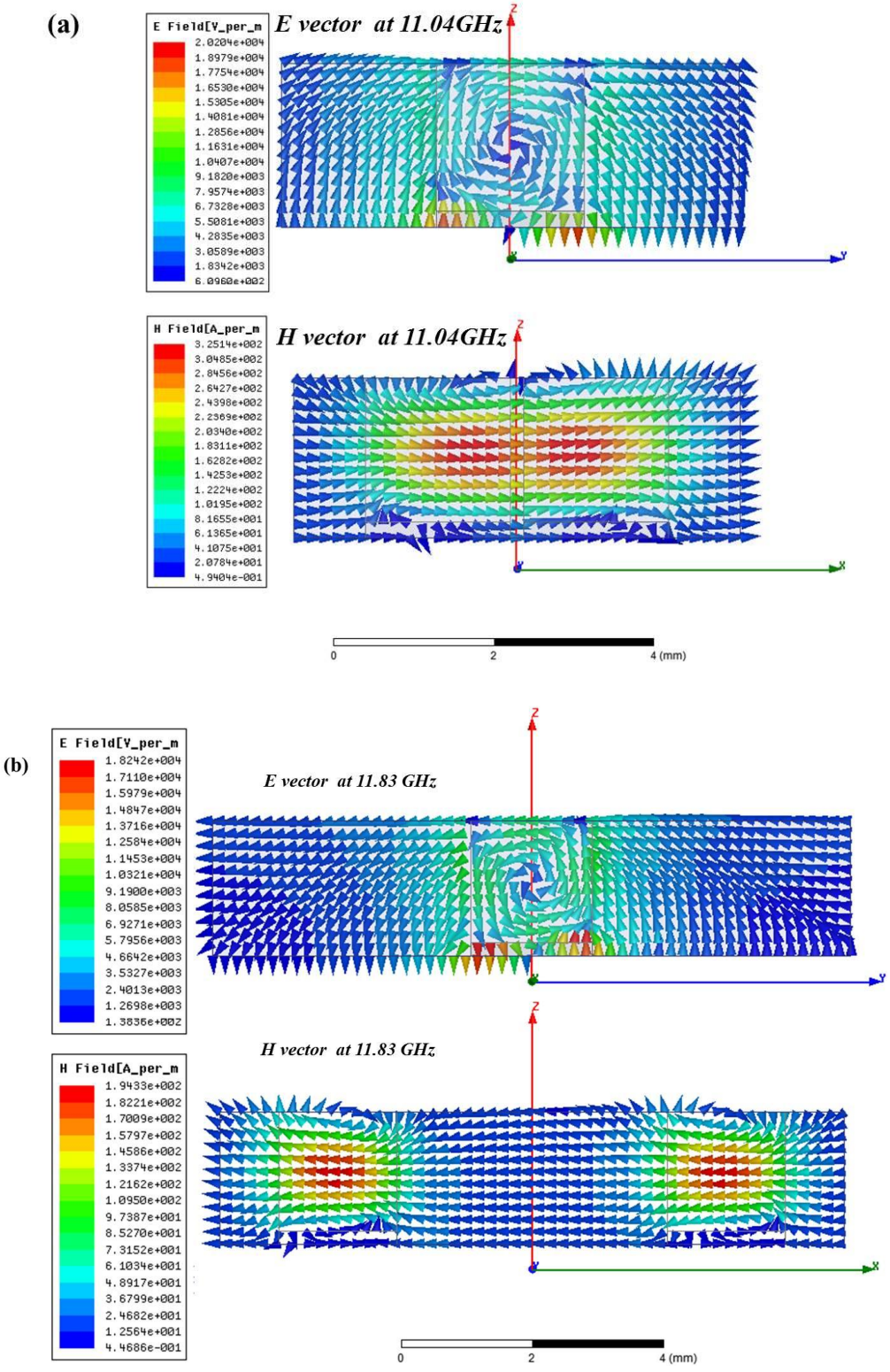

Fig.2.2.17 E and *H* vector at resonance frequency in the center of the cubes in *y*-*z* and *x*–*z* plane, (a) for *PH* = 2 mm and (b) for *PH* = 6 mm, respectively.

Compared to the pitch variation along *PH*, it does not show obvious frequency shift when the pitch changes along *PE*. From Fig.2.2.18 one can see that the absorption is much weaker if the cubes are too close to each other but it makes no significant change when the pitch is larger than 2 mm. And accordingly the field map of *E*-vector shows weaker values for a narrow pitch (Fig.2.2.19). Again we have to mention that here the polarization of the incident wave has to be considered once the symmetry is broken. Thus for *PE* in our demonstration, the period of the BST cubes does not change with respect of the polarization of the incident wave, hence the resonance does not shift and absorption just shows slight variation.

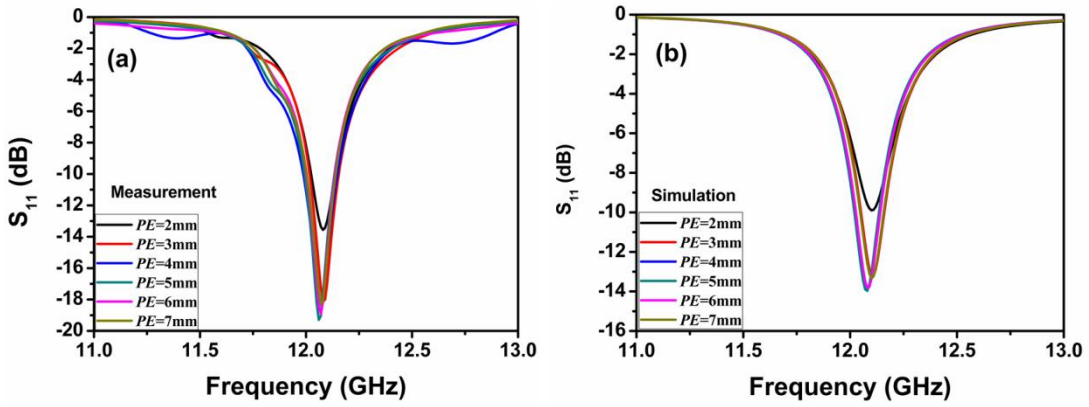

Fig.2.2.18 (a) Experimental and (b) simulated reflection spectra for BST cubes dimer when varying *PE* ranging from 2 mm to 7 mm.

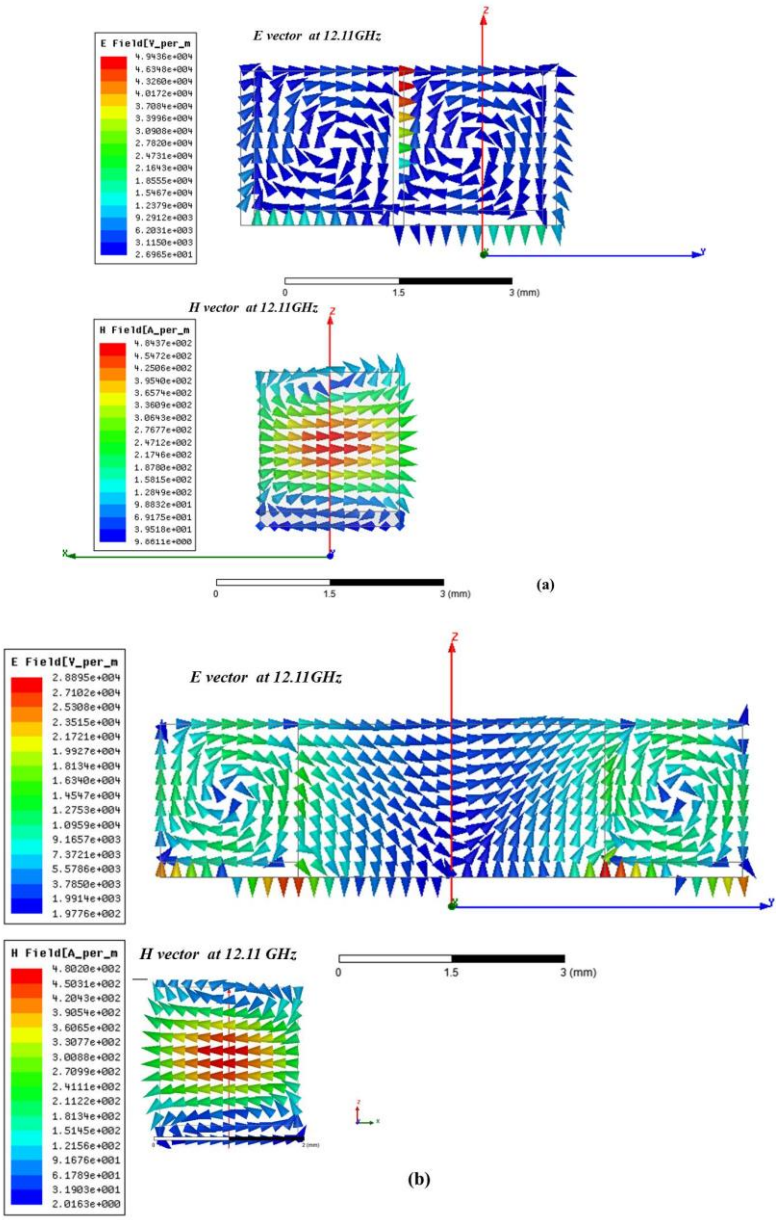

Fig.2.2.19 E and *H* vector at resonance frequency in the center of the cubes in *y*-*z* and *x*–*z* plane, (a) for *PE* = 2 mm and (b) for *PE* = 6 mm, respectively.

B Measurement in free space in Ku band

In this part we checked the absorption in free space in Ku-band. Considering the influence from the size dispersion of BST cubes, we found the optimized period is around 4 mm, which is different from simulation. In the following, we will analysis the size dispersion in details.

The free space measurement carried out by means of free space Vector Network Analyzing (VNA). The analyzer is connected to rectangular hollow waveguide through coaxial cables and coaxial-to-rectangular waveguide transitions. A schematic of the experimental configuration is shown in Fig.2.2.20 (a). It is worth-mentioning that the ecosorb layer AN77 layer defines the scattering area of the wave impinging either onto a bare copper plate (unit reflection whatever the operating frequency) and the selective reflecting metasurface that exhibits a dip in the reflectance spectrum. This setup has been calibrated using the TRL (Thru-Reflect-Line) method in the output plane of the waveguide transitions. The hollow waveguide is perpendicularly positioned h = 25 cm above the BST array to make sure that the wave, supplied by the analyzer could radiate over the whole BST array, with a maximum of power. Some of the BST cubes with the size around 1.8 mm under measurement are shown insert photograph in Fig.2.2.20 (b). We measured the varied periods from 3.0 mm to 6.0 mm under normal incidence. The frequency was swept from 11 GHz to 18 GHz working in Ku band. S_{11} versus frequency spectra was shown in Fig.2.2.20 (b) for the normal incidence with period varied from 3.0 mm to 6.0 mm. A reflection deep is located at ~ 12.4 GHz and the minimum reaches ~ - 9 dB in S_{11} spectra which corresponds to the maximum absorption at P = 4 mm.

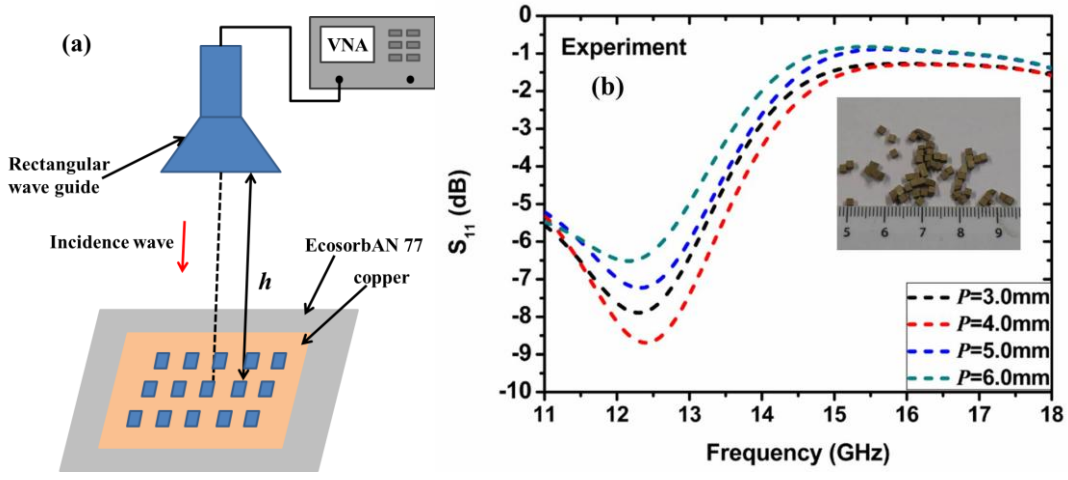

Fig.2.2.20 (a) schematic view of the experimental set-up in free space, (b) the experiment S_{11} spectra of BST cubes (with the side width around 1.8 mm) arrayed on the copper plate which measured under

normal incidence in the free space condition.

In summary, it can be achieved a single unit absorption peak by using ferroelectric metamaterials namely BST cubes with high permittivity above 100. This design idea can be verified both inside the wave guide and in the free space. For the former verification, we placed a BST cube with side width of 1.8 mm at the center of a 2 mm-thick aluminum plate by using adhesive, and then fixed the plate on the output port of the rectangular waveguide (X band wave guide and Ku band wave guide). It is obviously proved the design idea.

The second stage, we investigated the coupling effect between two BST cubes by using the same measurement method to put the two BST cubes in X band wave guide in *H* and *E* direction. Since it is the magnetic Mie-resonance at the first resonance frequency, when *PH* varied from 2 mm to 11 mm, there exist a frequency shift while when *PE* varied the absorption have no obvious variation.

At last stage, we proposed to measure the absorption properties in the free space to find the optimized period. In the measurement results we found the optimized is 4 mm, which is smaller than the simulation one (9 mm). This can be explained that the BST cubes are not with the exact same size since the fabrication error.

2.3 Giant causeway-like absorbers based on size dispersion of ferroelectric Mie type resonators

2.3.1 Design and analysis of the broadband absorbing layer

Based on periodic arrangement, perfect absorbers were analyzed in the previous sections. In particular, it was shown that the resonant frequency is not significantly affected by the period array but is mostly dominated by the size of BST cube. Here based on this conclusion, we introduce size dispersion in the longitudinal direction by

keeping a 2D periodic configuration to realize a broadband perfect absorber. The absorption spectrum mostly depends on the distribution of the resonant frequency. In other words, it is determined by the sum of the Mie resonators that is obtained by introducing several relevant dimensions, namely size dispersion. That introduces several resonance frequencies. By finely controlling the interval between each frequency, the various resonances could partially overlap. By superposition principle an ultra-broadband absorption window results from the overlap. One can image that with a large number of size avoiding any abrupt change in dimensions, broadband operation could be achieved. In a previous study, we showed that absorbance values close to unity can be explained by the balance condition between the quality coefficients related to the coupling of the incident energy with the absorbers and their dissipation properties. This is proved using ferroelectric and plasmonic gratings. Under these conditions, it was decided in a first stage, to preserve the periodicity by solely introducing a size distribution in the third dimension. However in a second stage we will see that a position disorder of the BST cubes can also be useful for dramatically broaden the absorption band.

In a general case, a distribution in size can be observed in the transverse and longitudinal dimensions is as shown schematically in Fig.2.3.1 (a). Here, we firstly depict an example of a periodic 2D BST array with 3 selected heights but the same dimensions of the base. The rectangular with same height are arranged in a square 2D array. A super-unit cell formed by 9 absorbing parallelepipeds can be easily figured out. In this simulation, the base of the cuboid is set to be 1.8 × 1.8 mm, while three different heights labeled by 1, 2 and 3, respectively in the inset schematic image, are selected between 1.65, 1.8 and 2.0 mm. An infinite periodic structure is mimicked by employing the master-slave boundary condition using HFSS. Such a configuration looks like the Giant's Causeway in Ireland, as shown in Fig.2.3.1 (b). If a wave with a broadband spectrum impinges on to this Giant’s Causeway like surface, specific frequencies will be selectively trapped by 1, 2 or 3, and thus be absorbed as demonstrated numerically

on the spectra shown in Fig.2.3.1 (c).

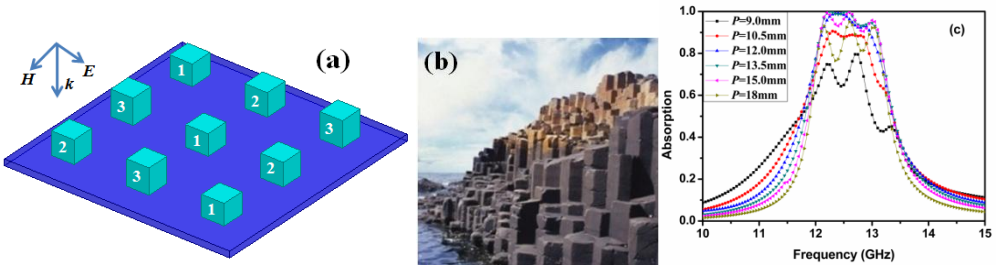

Fig.2.3.1 Schematic of a network of cubes of different heights BST (a), (b) the rocky structures of the Giant's Causeway, (c) Window of absorption calculated for a network of 9 absorbing centers

Let us now consider the effective impedance as a macroscopic parameter which can be regarded as an average impedance of the BST array and the space among them. If the density of the BST is too high (the period is too small), the impedance matching condition could not be satisfied. As a consequence, there will be some reflection on the incident facet and the critical coupling could not be satisfied as well. Such spurious reflection will dramatically weaken the absorbance value as for instance indicated by the black curve with period = 9 mm. By increasing the period, the effective impedance gets closer to that of free space, which increases the coupling to localized modes and thus a higher Q and hence higher absorbance. As illustrated by the various spectra displayed in Fig.2.3.1 (c), the maximal absorbance close to unity is achieved for P = 12 mm. By further diluting the BST array, one can notice that the individual peaks become narrower but the absorption remains maximal, which means the resonances are under the critical coupling condition. If we continue this dilution, sharper resonances with weaker absorbance can be expected. Since the absorption occurs locally in the BST resonators, which relax somehow the period requirement for maximal absorption, the period shows a large tolerance of ~ 3 mm, which is almost 2.5 times the BST base length, from 12 mm to 15 mm for maximal bandwidth according the spectra with the FWHM around 12 %.

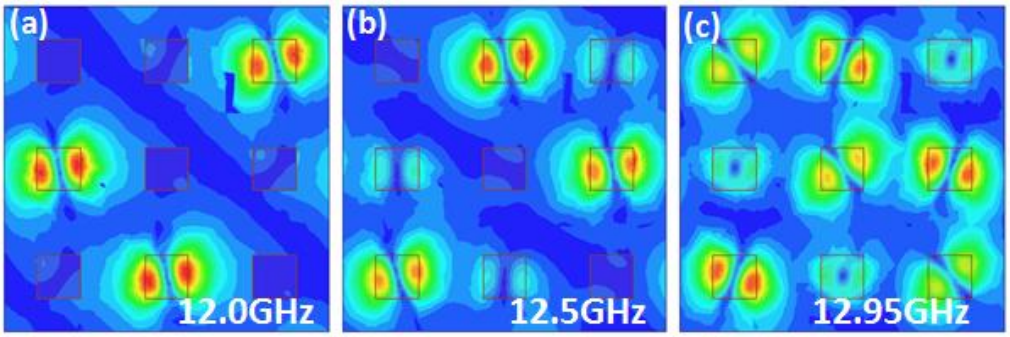

Fig.2.3.2 The *E*-field magnitude is plotted in the BST mid-plane, for the configuration corresponding to the optimized period P = 12 mm at (a) 12.0 GHz, (b) 12.5 GHz, (c) 12.95 GHz.

In order to observe the mode trapping behaviors, the electric field maps for P = 12 mm in a horizontal mid plane was investigated as depicted in Fig.2.3.2. The three frequencies, which were chosen, correspond to the absorption peaks, which form the broadband spectra illustrated in Fig.2.3.1. They are related to the eigen resonance modes of the BST cuboids with three different selected heights. In Fig.2.3.1 (a) a lower frequency at 12.0 GHz was merely trapped in BST 3, because the resonance frequency is below the cutoff frequency of other smallest height BST labeled 1 and 2. As a consequence no EM-field is localized in BST 1 and BST 2 for instance located in the first row. When the frequency goes higher and reaches the resonance frequency of BST 2 that has a little bit shorter height, the impinging wave is trapped mainly by BST 2. As Fig.2.3.2 (c) shows, at 12.95 GHz that is above or matches all the cutoff frequencies of BST cubes, we can clearly observe the trapping modes in all the BST cubes with different intensities that are related to the mismatches to the resonance frequencies. Meanwhile, since the high frequency wave could not be fully trapped by BST 1 who has the highest absorbance, thus the final absorption is lower at high frequency as it can be noted from the spectra in Fig.2.3.1.

In a second stage, we designed the absorbing layer with four different height of BST cuboids (a_{z1} = 1.6 mm, a_{z2} = 1.75 mm, a_{z3} = 1.9 mm, a_{z4} = 2.3 mm) to have a more broadband absorption, the basic super-cell is shown in Fig.2.3.3. Two configurations

correspond to the schematic in (a) and (b).

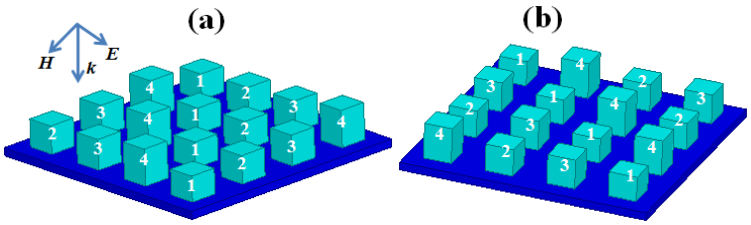

Fig.2.3.3 Schematics of an array of 16 BST cuboids with four different heights (a) 1, 2, 3 and 4 arrangement, (b) 1, 4, 2 and 3 arrangement for the first row.

Fig.2.3.4 shows the absorption spectrum of the two configurations with the optimized period P = 16 mm. We found the FWHM around 16 %.

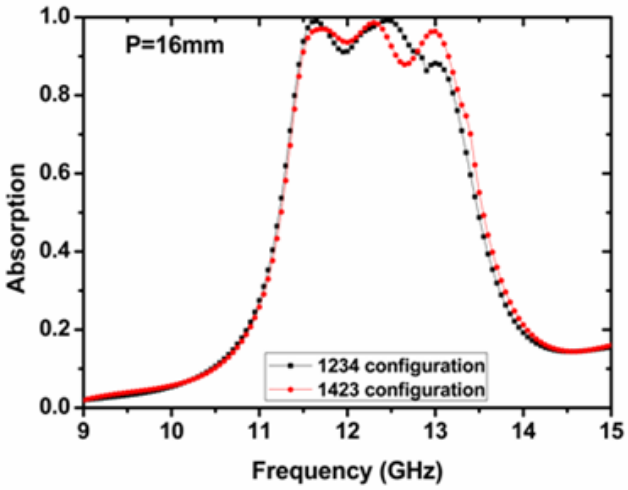

Fig.2.3.4 Absorption window calculated for two different arrangement (1234 and 1423 configurations) of an absorber consisted of 16 resonators in the super-cell.

In the last step, the BST cubes with 16 different heights were randomly positioned on the substrate with a specific period, as shown in Fig.2.3.5 (left-side). The absorbance spectra, also displayed in this figure for three configurations (right-side), exhibit in all cases a broad absorption window from frequency around 10.5 GHz up to 13.4 GHz in the best case.

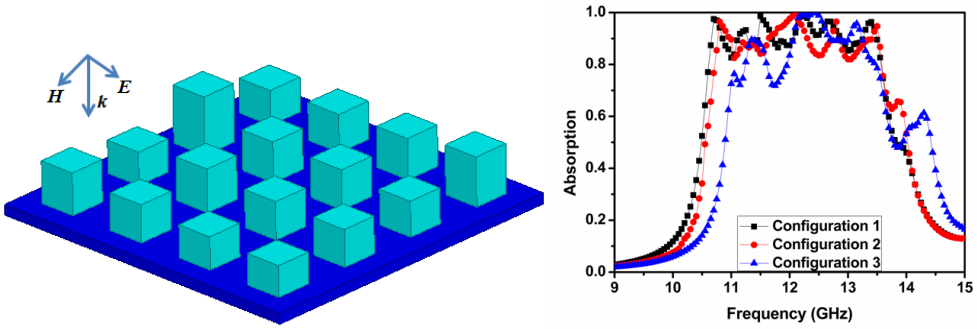

Fig.2.3.5 Schematic of an array of 16 BST cuboids with 16 different heights from 1.4 mm to 2.6 mm randomly varied (left figure). Absorption spectrum as a function of frequency for three different configurations (right figure).

2.3.2 Experimental verification

For experimental verification of the broadening effect, we compared the absorption spectrum for a mono-dispersed absorber system with the one measured for a set of micro-resonators dispersed in size. In the test of the mono-disperse resonator, a single BST cube with height between 1.8 mm and 3 mm was positioned at the center of a metal plate that was used as a back short of a rectangular waveguide. On the basis of the expected resonance frequencies, the measurements were performed in X-band. A photo of the flange of the rectangular waveguides along with the BST resonator onto the aluminum metal plate is shown in Fig.2.3.6.

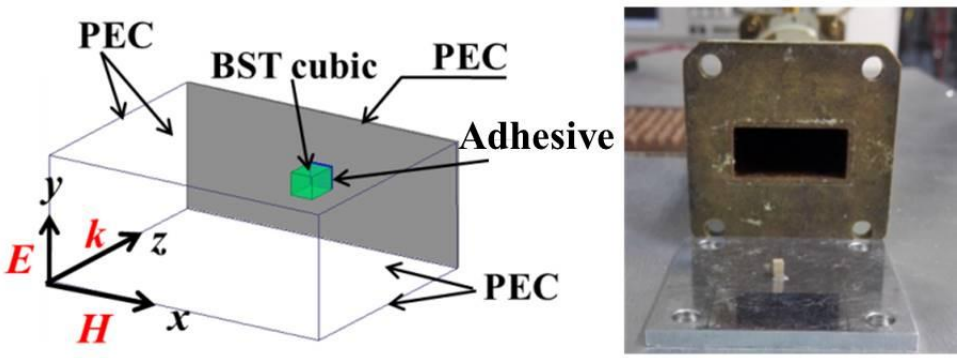

Fig.2.3.6 Schematic of the simulation domain mimicking an X-band wave guide loaded by the absorber basic cell and boundary conditions (left-side). Photograph of the flange of an X band wave guide

associated to a single micro-resonator positioned on a metal plate by using adhesive (right-side).

Taking the measurement accuracy as well as the shape errors into account, the experimental results show a good agreement with simulation results as seen in Fig.2.3.7. One can notice that all these BST cuboids efficiently absorb the incident wave, with absorbance peaks close to unity. In addition, one can note that the 1.2 mm height variation (1.8 mm-3.0 mm) results in a large frequency ranging up to nearly 3 GHz. Such a preliminary result intuitively indicates that a broad absorption window could be achieved by exploiting size dispersion effect in general or more specifically height dispersion effect as studied in the present work. It is however worth-mentioning that in the simulation we used PEC boundary conditions to simulate the metal rectangular waveguides, thus introducing a virtual periodicity through image effects. In a practical situation, a distribution in the height of a set of elemental resonators has to be introduced.

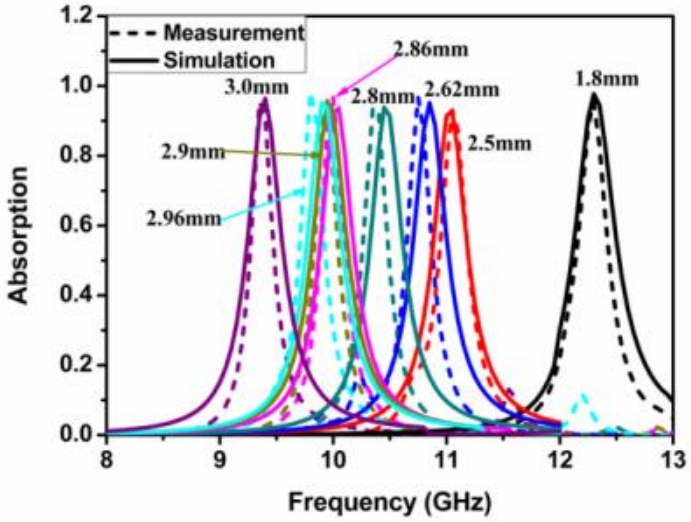

Fig.2.3.7 Comparison between experimental and simulation results for single BST rectangular with various heights ranging from 1.8 mm to 3.0 mm.

Owing to the limited quantity of the BST samples the broadening enhancement of the absorbance window by height dispersion was verified again in a waveguide operation mode. Herein a set of eight BST cubes with discrete heights around the

average value was selected and was regularly arranged on the metal plate to meet the periodic requirement, as illustrated in Fig.2.3.8.

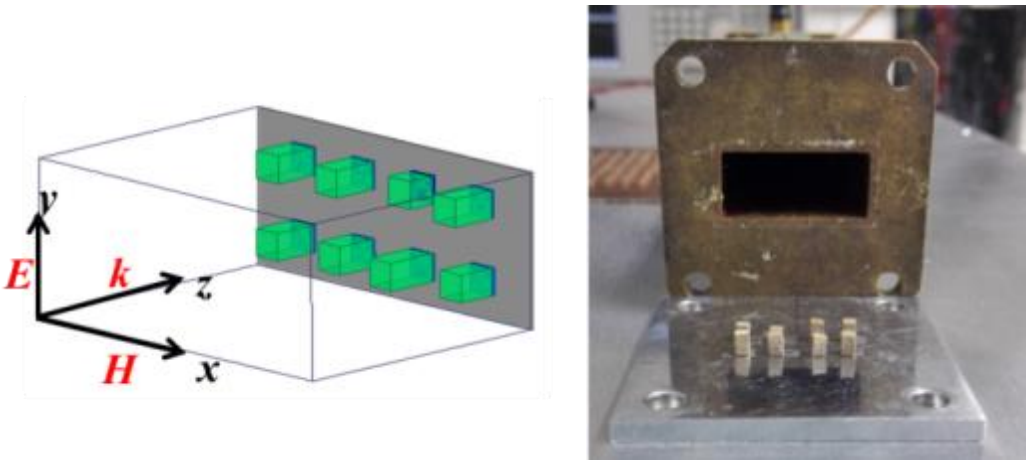

Fig.2.3.8 Schematic of the basic cell in X-band wave guide and the simulation conditions (left). Photograph of the 8 BST rectangular arrays. Photo of X band waveguide completed with eight micro-resonators deposited on a metal plane (right).

One expects multiple absorption peaks (reflection notches) that correspond to the resonance BST absorbers with different heights. Compared to the narrow spectrum of a single resonator, a significantly broadened absorption window is formed by the superposition of multiple resonances, induced by size dispersion. Meanwhile, as shows in Fig.2.3.9 the measured spectrum agrees qualitatively with the simulation result, except a discrepancy of the resonance at higher and lower frequencies. We believe that this discrepancy is caused by the dimension difference between the fabricated resonators and the parameters used in simulation. According to the analysis described above, the resonance strength can be depicted by the Q factor. Under the condition that the free space-resonator coupling mode balances the dissipation in the resonating cavity, namely critical coupling, a strong absorbance but with narrow band width is achieved. Therefore due to a slight unbalance probably over coupling, the Q factors in simulation are relatively lower than measured ones so that these peaks with maximal absorbance merge to an undistinguished peak.

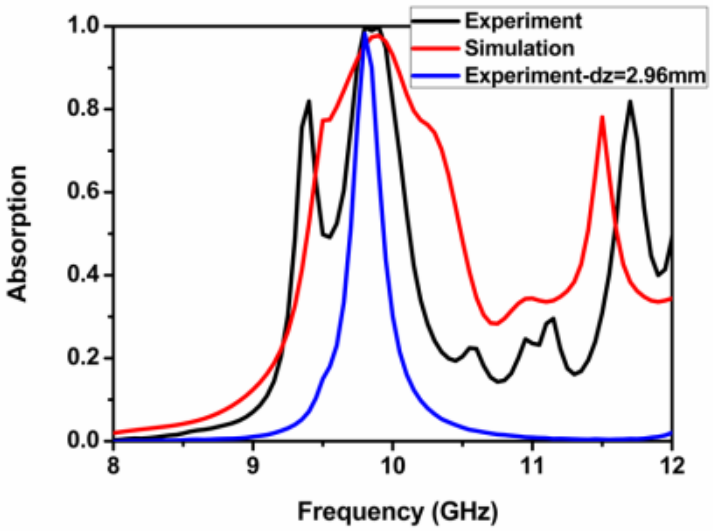

Fig.2.3.9 Illustration of the results of measurements and simulation for absorber consisting of ferroelectric elements whose longitudinal dimensions have been distributed as 1.8 mm, 2.5 mm, 2.62 mm, 2.8 mm, 2.82 mm, 2.9 mm, 2.96 mm, 3.0 mm.

To conclusion that, size dispersion of ferroelectric BST cubes in longitudinal direction can broaden the absorbance windows compare to the single BST cube.

2.4 Bandwidth enhancement by BST randomly positioned absorber

2.4.1 Design and simulation analysis

Recently, high absorption levels have been measured at optics by using plasmonic cubes randomly deposited on a metallic plate coated with a thin dielectric film [40, 41]. By using Barium Strontium Titanate (BST) cubes resonating at centimeter wavelength, we compare in this section the response of periodic and random arrays and we show that a random array of identical size cubes can lead to a broadening of the absorption bandwidth with respect to the response of a periodic one.

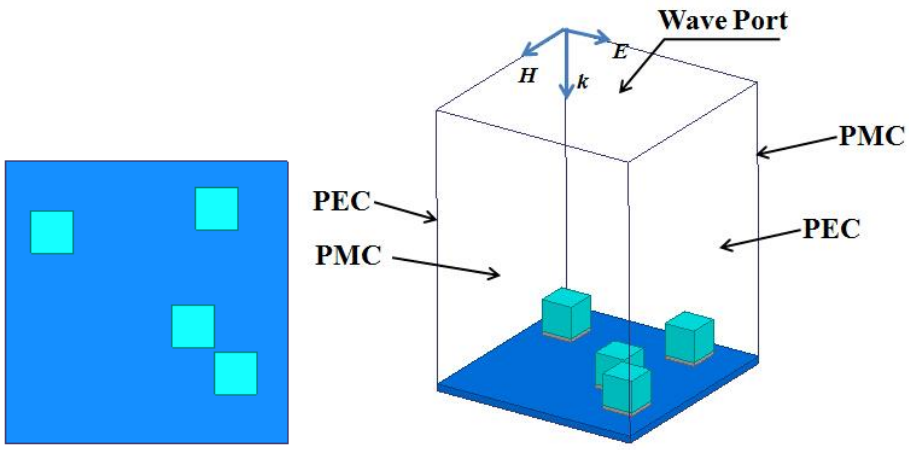

Fig. 2.4.1 Schematic of the basic super-cell in the top view (left) and the simulation conditions (right).

In order to introduce some disorder in a periodic array, we consider a super-cell including 4 BST cubes randomly positioned onto a 12 × 12 mm^2 area metallic ground plate see in Fig. 2.4.1 (left). In the simulation, PEC and PMC boundary condition are used, as show in Fig. 2.4.1 (right). A dielectric adhesive tape is sandwiched between the BST cube and plate to satisfy the experiment condition.

The frequency response of this random super-cell compared to the one of a periodic structure consisting of 4 cubes regularly positioned over the same area ($P_x = P_y$ = 6 mm) is reported in Fig. 2.4.2. In this condition, the average BST filling factor is kept constant. By comparing the two absorption spectra, one can notice that the maximum absorbance value is about 0.8 for a periodic array and close to 1 for a random array. For the random super-cell, absorbance not only solely exceeds this maximum value of 80 % but the absorption bandwidth is also broadened. This property can be explained by the coupling phenomena occurring when the BST cubes are close to each other. Indeed, the consequence of this random arrangement with various coupling strengths between the cubes is a frequency and angular distribution of the magnetic dipoles (see Fig. 2.4.1).

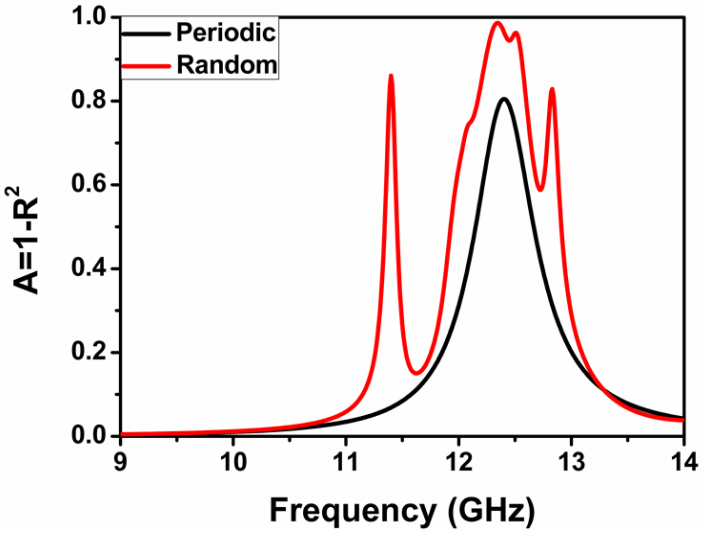

Fig. 2.4.2 The absorption spectrum as a function of the frequency for random and periodic (P = 6 mm) structure as shown in Fig.2.4.1, the BST cubes with the side length of 1.8 mm.

On the H-field maps of the random configuration reported at different resonance frequencies in Fig. 2.4.3, one can note that, the EM-field is confined inside two close cubes at lowest resonance frequency of 12.11 GHz. While, at higher frequency the EM-field is mainly confined inside separate cubes.

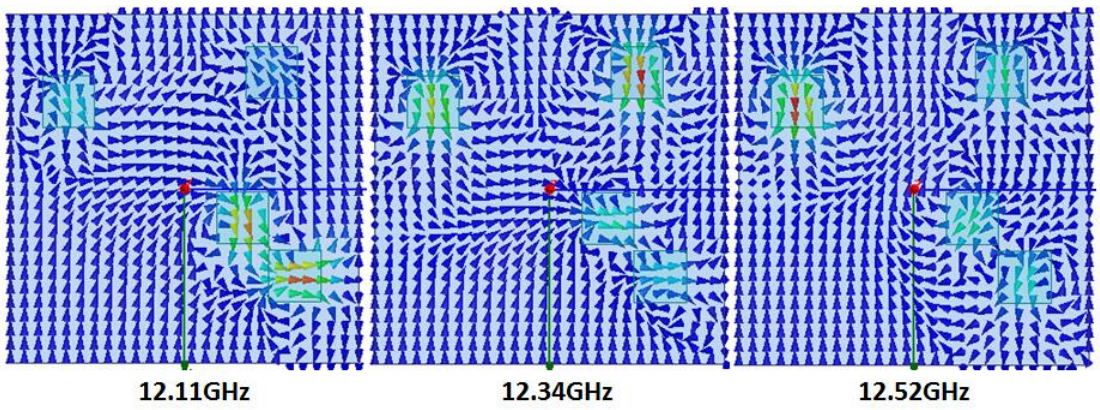

Fig. 2.4.3 H-vector for random structure at frequency 12.11 GHz, 12.34 GHz and 12.52 GHz, respectively.

2.4.2 Characterization in free space

Free space verification of a broadband absorption for random array has been performed using a Vector Network Analyzer connected to a rectangular horn antenna

through a coaxial cable. The horn antenna was positioned at 16 cm above the structured random absorber. We used 174 BST cubes deposited on a copper plate with areas of 4.5 × 4.5 cm^2. During the S11 measurements the absorber consisting of the copper plate coated with the random BST resonators was set onto an Ecosorb AN77 absorbing foam in order to limit the influence of parasitic reflections. Fig. 2.4.4, shows on the left-hand side a photograph of the random BST cubes deposited on the copper plate, while a schematic illustration of the measurement set up is reported on the right.

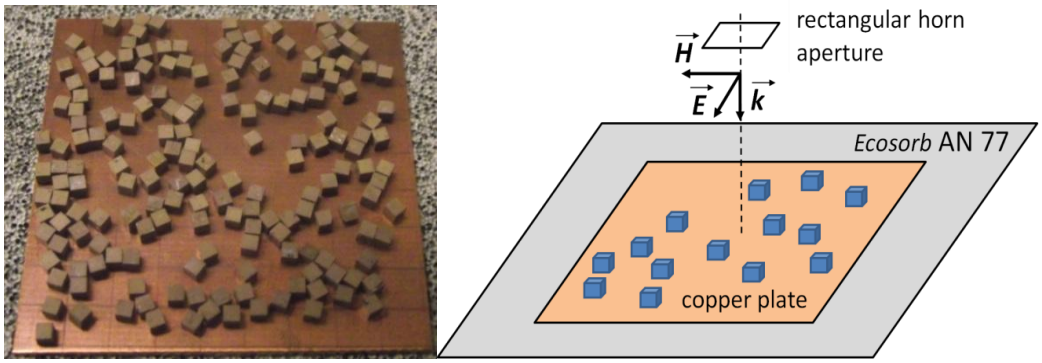

Fig. 2.4.4 (left) Photograph of the random BST cubes (side length around 1.8 mm) sample deposited on the copper plate, (right) schematic illustration of measurement set up.

In Fig. 2.4.5Fig. 2.4.1, we plot the frequency response related to the random structure as shown in Fig. 2.4.1 (left). The frequency response shows a broadening effect for the random structure. This phenomenon is the signature of the coupling between cubes in close vicinity.

In summary, the introduction of position disorder of BST cubes can be broadening the absorbance window which was verified by measurement in free space. This broaden effect can be explained by the coupling between two adjust cubes.

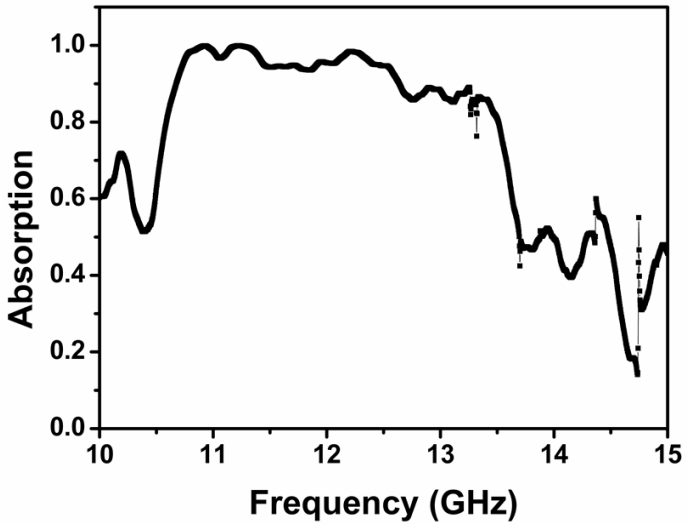

Fig. 2.4.5 Experimental absorption spectrum for the random structure in figure 2.4.4 (left).

2.5 Conclusion

In summary, we have proposed and demonstrated numerically and experimentally that a PMA based on Mie-resonance in ferroelectric metamaterials can be achieved both for single absorption peak (typically 5% for the Fractional Bandwidth FB) and relatively broadband absorption window (FB~25%).

To this aim, we firstly designed a periodic BST array structure to achieve unit absorption at targeted frequencies by optimizing the parameters such as the complex permittivity of BST ferroelectric dielectric layer, the size of BST resonators and the period of the array, numerically. This theoretical analysis showed, via the simulation of the reflection coefficient and of the dispersion diagram, that the magnetic Mie-type resonance mode was responsible of the dramatic enhancement of the absorptivity. It was also shown that some trade-off exists in the coupling mode between the incident wave and the resonators and the dielectric dissipation mechanisms when the EM-energy is trapped in the ferroelectric absorption centers. Following this theoretical work, an experimental verification was carried out in a hollow metal wave guide configuration assessing the enhancement of the overall absorption at the resonance frequency.

In a second stage, the possibility to broaden the absorption window was studied following two routes. The main approach was based on a longitudinal size dispersion of Ferroelectric rectangular periodically arranged on a metal plate. On this topic, it was primarily demonstrated, by numerical simulations, that such a cuboid-height dispersion by preserving the periodicity of the position introduces a dispersion in the relevant resonance lengths with subsequently a broadening of the overall absorption window. Here again an experimental assessment of the broadening was presented by using single-and multi-size resonators in a wave guide.

At last, the introduction of a position disorder of the BST cubes was introduced showing a broad absorption window, by the measurement of the reflectance carried out in free space for a large number of absorbing resonators. Such an enhancement in the band-width was explained by the coupling of the magnetic dipole when the resonators are in close proximity.

References

[1] P. Bao, T. Jackson, X. Wang and M. Lancaster, Barium strontium titanate thin film varactors for room-temperature microwave device applications, J. Phys. D, Vol.41, 063001, 2008.

[2] M.W. Cole, P. C. Joshia, M. H. Ervina, M. C. Wooda and R. L. Pfeffer, The influence of Mg doping on the materials properties of $Ba_{1-x}Sr_xTiO_3$ thin films for tunable device applications, Thin Solid Films, Vol. 374, 34-41, 2000.

[3] M. W. Cole, P. C. Joshi and M. H. Ervin, La doped $Ba_1AxSrxTiO_3$ thin films for tunable device applications, J. Appl. Phys., Vol. 89, No. 11, 6336- 6340, 2001.

[4] A. Tagantsev, V. Sherman, K. Astafiev, J. Venkatesh and N. Setter, Ferroelectric materials for microwave tunable applications, J. Electroceram, Vol. 11, 5-66, 2003.

[5] S. Gevorgian and E. Kollberg, Do we really need ferroelectrics in paraelectric

phase only in electrically controlled microwave devices?, IEEE Trans. Microw. Theory Techn., Vol. 49, 2117-2124, 2001.

[6] N. Setter, D. Damjanovic, L. Eng, G. Fox, S. Gevorgian, S. Hong, A. Kingon, H. Kohlstedt, N. Park, G. Stephenson, I. Stolitchnov, A. Taganstev, D. Taylor, T. Yamada, and S. Streiffer, Ferroelectric thin films: review of materials, properties, and applications, J. Appl. Phys.Vol.100, 051606, 2006.

[7] S. Gevorgian, Ferroelectrics in microwave devices circuits and systems, ISBN 978-1-84882-507-9, 2009.

[8] D. Kuylenstierna, A. Vorobiev, P. Linnér and S. Gevorgian, Composite right/left handed transmission line phase shifter using ferroelectric varactors, IEEE Microw. Compon. Lett., Vol. 16, 167-169, 2006

[9] G. Vélu, K. Blary, L. Burgnies, J. C. Carru, E. Delos, A. Marteau and D. Lippens, A 310^{o}/3.6-dB K-band phaseshifter using paraelectric BST thin films IEEE Microw. Compon. Lett., Vol. 16l, 87-89, 2006.

[10] L. Burgnies, G. Vélu, G. Houzet, K. Blary, J. Carru and Didier Lippens, A TRL-like calibration for tunable interdigitated BST varactors, IEEE Trans. Instrum. Meas., Vol. 57, 1127-1132, 2008.

[11] K. Pan, H. Jiang, D. Brown, C. Zhang, M. Patterson and G. Subramanyam, Frequency tuning of CPW bowtie antenna by ferroelectric BST thin film varactors, IEEE NAECON, 978-1-4577, 1 - 4, 2011.

[12] A. Kanareykin, E. Nenasheva, A. Kozyrev, S. Kazakov, Observation of an anomalous tuning range of a dopen BST ferroelectric material developed for accelerator applications, Proceedings of IPAC'10, 3987-3989, Kyoto, Japan.

[13] D. P. Gaillot, C. Croënne and D. Lippens, An all-dielectric route for terahertz cloaking, Opt. Express, Vol. 16, 3986-3992, 2008.

[14] S. S. Kim, E. K. Choi, H. J. Kim, M. H. Park, H. S. Lee, W. J. Kim, J. C. Bae, T. K. Song, H. S. Lee and J. Y. Lee, Ferroelectric properties of (Bi, Sm)$_4$Ti$_3$O$_{12}$ (BST) thin films fabricated by a metalorganic solution deposition method, J. of Electroceram., Vol. 13, 83-88, 2004.

[15] Y. Jiang, Y. Wang, K. Choi, D. Rajamani and Andrew Hunt, Ferroelectrics - Material Aspects, ISBN: 978-953-307-332-3, Chapter 1: BST and other ferroelectric thin films by CCVD and their properties and applications. ferroelectrics-material aspects, 2011.

[16] T. Lepetit, É. Akmansoy and J. P. Ganne, Experimental measurement of negative index in an all-dielectric metamaterial, Appl. Phys. Lett., Vol. 95, 121101, 2009.

[17] G. Houzet, L. Burgnies, G. Velu, J. Carru and D. Lippens, Dispersion and loss of ferroelectric $Ba_{0.5}Sr_{0.5}TiO_3$thin films up to 110 GHz, Appl. Phys. Lett. Vol. 93, 053507, 2008.

[18] A. Marteau, G. Velu, G. Houzet, L. Burgnies, E. Lheurette, J. C. Carru and D. Lippens, Ferroelectric tunable balanced right- and left-handed transmission lines, Appl. Phys. Lett. Vol. 94, 023507, 2009.

[19] Q. Zhao, B. Du, L. Kang, H. Zhao, Q. Xie, B. Li, X. Zhang, J. Zhou, L. Li and Y. Meng, Tunable negative permeability in an isotropic dielectric composite, Appl. Phys. Lett. Vol. 92, 051106, 2008.

[20] H. Zhao, L. Kang, J. Zhou, Q. Zhao, L. Li et al., Experimental demonstration of tunable negative phase velocity and negative refraction in a ferromagnetic/ferroelectric composite metamaterial, Appl. Phys. Lett. Vol. 93, 201106, 2008.

[21] T. Lepetit, E. Akmansoy and J. Ganne, All-dielectric metamaterial: a ferroelectric-based scheme in the microwave range, Proc. SPIE Vol. 7392 73920H-1, 2009.

[22] G. Houzet, K. Blary, S. Lepilliet, D. Lippens, L. Burgnies, G. Véu, J. C. Carru, E. Nguéma and P. Mounaix, Dielectric dispersion of $BaSrTiO_3$ thin film from centimeter to submillimeter wavelengths, J. Appl. Phys. Vol.109, 014116, 2011.

[23] T. Lepetit, E. Akmansoy, M. Pate and J. P. Ganne, Broadband negative magnetism from all-dielectric metamaterial, Electron.Lett. Vol. 44, No. 19, 2008.

[24] L. Liu, J. Sun, X. Fu, J. Zhou and Q. Zhao, Artificial magnetic properties of dielectric metamaterials in terms of effective circuit model, PIER, Vol. 116, 159-170, 2011.

[25] L. Kang, Q. Zhao, H. Zhao and J. Zhou, Magnetically tunable negative permeability metamaterial composed by split ring resonators and ferrite rods, Opt. Express, Vol. 16, 8825-8834, 2008.

[26] F. Zhang, Q. Zhao, L. Kang, J. Zhou and D. Lippens, Experimental verification of isotropic and polarization properties of high permittivity-based metamaterial, Phys. Rev. B, Vol. 80, 195119, 2009.

[27] F. Zhang, L. Kang, Q. Zhao, J. Zhou and D. Lippens, Magnetic and electric coupling effects of dielectric metamaterial, New J. Phys. Vol. 14, 2012.

[28] V. Sadaune, L. Kang and D. Lippens, Enhanced transmission via a sub-wavelength hole aperture coupled to a high-permittivity resonator, J. Phys. D: Appl. Phys. Vol. 45, 475102, 2012.

[29] S. Kim, E. Choi, H. Kim, M. Park, H. Lee, W. Kim, J. Bae, T. Song, H. Lee and J. Lee, Ferroelectric properties of (Bi, $Sm)_4Ti_3O_{12}$ (BST) thin films fabricated by a metalorganic solution deposition method, J. Electroceram., Vol. 13, 83-88, 2004.

[30] Q. Zhao1, J. Zhou, F. Zhang and D. Lippens, Mie resonance-based dielectric metamaterials, Mater. Today, Vol.12, 60-69, 2009.

[31] C. Vandenbem and J. Vigneron, Mie resonances of dielectric spheres in

face-centered cubic photonic crystals, J. Opt. Soc. Am., Vol. 22, 1042-1047, 2005.

[32] X. Liu, Q. Zhao, C. Lan and J. Zhou, Isotropic Mie resonance-based metamaterial perfect absorber, Appl. Phys. Lett., Vol. 103, 031910, 2013.

[33] F. Zhang, S. Feng, K. Qiu, Z. Liu, Y. Fan, W. Zhang, Q. Zhao and J. Zhou, Mechanically stretchable and tunable metamaterial absorber, Appl. Phys. Lett., Vol. 106, 091907, 2015.

[34] Q. Zhao, B. Du, L. Kang, H. Zhao, Q. Xie, B. Li, J. Zhou, L. Li, and Y. Meng, Tunable negative permeability in an isotropic dielectric composite, Appl. Phys. Lett., Vol. 92, 051106, 2008.

[35] F. Zhang, L. Kang, Q. Zhao, J. Zhou, and D. Lippens, Magnetic and electric coupling effects of dielectric metamaterial, New J. Phys.14, 033031, 2012.

[36] A. Sellier, T. V. Teperik and A. de Lustrac, Resonant circuit model for efficient metamaterial absorber, Opt. Express Vol. 21, A997-A1006, 2013.

[37] C. M. Watts, X. Liu and W. J. Padilla, Metamaterial electromagnetic wave absorbers, Adv. Mater. Vol. 24, OP98-OP120, 2012.

[38] N. I. Landy, C. M. Bingham, T. Tyler, N. Jokerst, D. R. Smith and W. J. Padilla, Design, theory and measurement of a polarization insensitive absorber for terahertz imaging, Phys. Rev. B, Vol. 79, 125104, 2009.

[39]. A. Moreau, C. Ciraci, J. J. Mock, R. T. Hill, Q. Wang, B. J. Wiley, A. Chilkoti, and D. R. Smith, Controlled-reflectance surfaces with film-coupled colloidal nanoantennas, Nature, Vol. 492, 86-89, 2012.

[40]. X. Chen, H. Gong, S. Dai, D. Zhao, Y. yang, Q. Li and M. Qiu, Near-infrared broadband absorber with film-coupled multilayer nanorods, Opt. Lett., Vol. 38, 2247-2249, 2013.

[41]. Y. Nishijima, L. Rosa and S. Juodkazis, Surface plasmon resonances in periodic and random patterns of gold nano-disks for broadband light harvesting, Opt. Express, Vol. 20, 11466-11477, 2012

Chapter 3 Broadband perfect absorbers in disordered meta-materials

3.1 Introduction

As well-known electromagnetic metamaterials with very small dimensions comparing to the operation wavelength, can manifest positive, zero or negative refractive index depending on the values of ε_{eff} and μ_{eff} [1-3]. For instance in Ref. 2, the effective permittivity and permeability was determined from reflection and transmission coefficients of periodic wires or split ring resonators (SRR) arrays. In practice, to achieve such unusual parameters of constitutive equations from conventional materials, one has to take benefit of field localization effects. As an example in an array of open split ring resonators allowing the coupling of the resonance modes with an impinging wave. This kind of materials can be formed either in periodic or random arrays. For a periodic arrangement of the resonators, the scattering properties are strongly dependent on the periodicity as in photonic crystal technologies [4]. But for metamaterials the properties rely mainly on refraction principles. As a consequence, their frequency response can tolerate a periodicity disorder as long as the coupling effects between nearby resonators remain negligible, which can be clearly understood by Fig. 2.2.10 in chapter 2.

As one form of metamaterial, disordered materials can be designed by self-organized bottom-up processes, which simplify the fabrication programs [5]. Following these principles, the topic of disorder in metamaterials has motivated extensive studies over the past ten years. In reference [6], R. Singh et al. experimentally demonstrated the weak influence of positional disorder on the transmission properties of Split Ring Resonators (SRR) arrays designed for terahertz operating frequencies. In this study, the coupling forces between nearby resonators remain weak. Distinguishing between incoherent (closed rings) and coherent metamaterial particles (asymmetric

split ring structures), the deformation of disordered metamaterial frequency response when the coupling forces can no more be neglected is clearly evidenced in Ref. 7. More recently, the same group experimentally imaged these coupling forces in disordered coherent metamaterials by measuring speckles-like localization effects using near field probing [8]. Some authors tried to understand the positional disorder influence beyond the frequency response criteria by analyzing separately the electric and magnetic properties of the metamaterial [9]. C. Helgert et al. showed experimentally that the disorder impact is stronger on the effective permittivity with respect to the effective permeability by measuring the response of cut-wire pair arrays designed for near infrared wavelengths both at normal [10] and oblique incidence [11]. Other works have been devoted to size disorder influence of the elementary particle while keeping the periodicity constant [12] and combining size and position disorders influence is addressed in [13] which is focused on magnetic properties.

Beyond the technological aspects, the next step is to understand whether disorder can be used in order to extend the properties of metamaterial structures. In Ref. 14, controllable anomalous localization effects are evidenced by using a Lévy-type distribution within a 1D structure. Recently, A. Moreau et al. have shown increasing effects of the average absorption for disordered meta-surfaces made of silver nanocubes deposited on a gold back-grounded polymer film at visible and near infrared wavelengths [15].

Subsequently, Y. Nishijima et al. proposed a broadband light harvesting device based on surface plasmon resonances from order to disorder distribution of gold nano-disks [16]. X. Chen et al. demonstrated a broadband absorber by depositing randomly gold nanorods onto a gold metal plate separated by a thin dielectric layer [17]. Following these works, our group designed a broadband absorber with an array of randomly positioned rings onto FR-4 substrate [18-19]. More recently, S. Cao et al. reported a broadband solar energy absorbers based on a random nanospheres distributed in different layers [20]. Beyond the position random structure, Ali Kemal Okyay's group

introduced size disorder of nano silicon particles for broadband detection [21].

In this chapter, special attention was paid attention to the following question: how random ring resonator distributions can be used as an efficient way for improving metamaterial-based absorber performances in terms of absorption level and relative bandwidth through the disorder and filling factor. Basically, the main originality of the present work stems from a progressive introduction of a position disorder in electromagnetic resonator arrays without intentionally introducing dispersion in the size, geometry (via aspect ratio notably), or material parameter in contrast to the results reported in the literature. It is shown that the sole variation of the resonator inter-distance in a super-cell results in a wide broadening of the absorption windows due to sub-cell coupling. To this aim, an optimal period for periodic and hence position ordered arrays was pointed out owing to the existence of a critical trapping of the impinging wave. On this basis, a three-fold broadening of the absorption window by preserving a quasi-unit absorbance was evidenced for highly disordered media.

The frame of this chapter is as follows: firstly, steel rings periodically arrayed on a FR-4 dielectric substrate coated with a copper metal ground plane are designed to have a single band perfect absorption. Then, on the basis of an optimum period some position disorder of resonators is introduced for broadening the absorption band width. To have a clear understanding of the broadening mechanism, several random configurations associated with various filling factor are investigated as a function of incidence angle. Finally, experimental verification in free space is reported.

3.2 Periodic steel rings array

3.2 .1 Magnetic response in steel rings resonators

The metamaterial structure includes steel rings (outer diameter: 9 mm, inner diameter 3 mm, thickness: 0.83 mm) deposited onto an Epoxy (FR-4) substrate (thickness: 0.85 mm, permittivity ε_r = 3.6, loss tangent tan (δ) = 0.02) back-coated with

a uniform copper thin film (typical thickness: 35 μm) as shown Fig. 3.2.1.

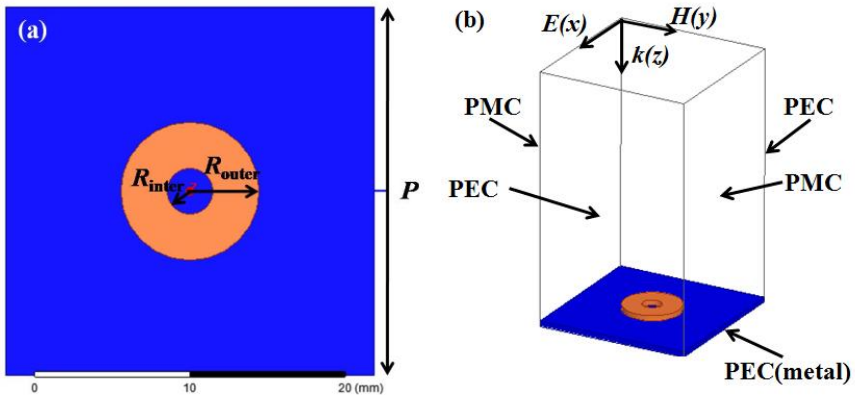

Fig. 3.2.1 Schematic of the basic resonator (a) top view with its characteristic parameters (b) Illustration of simulation conditions.

Fig. 3.2.2 shows the frequency dependence of the magnitude of the extinction coefficient noted E and defined as $E = 1 - S_{11}^2$. From this figure, it can be noted that the fundamental magnetic resonance frequency is located at 9.11 GHz with a unit absorbance value. Let us remind that unit absorbance can be achieved for period equals to 24 mm in order to satisfy the impedance matching condition. This is the configuration used for the spectrum plotted in Fig. 3.2.2 (a).

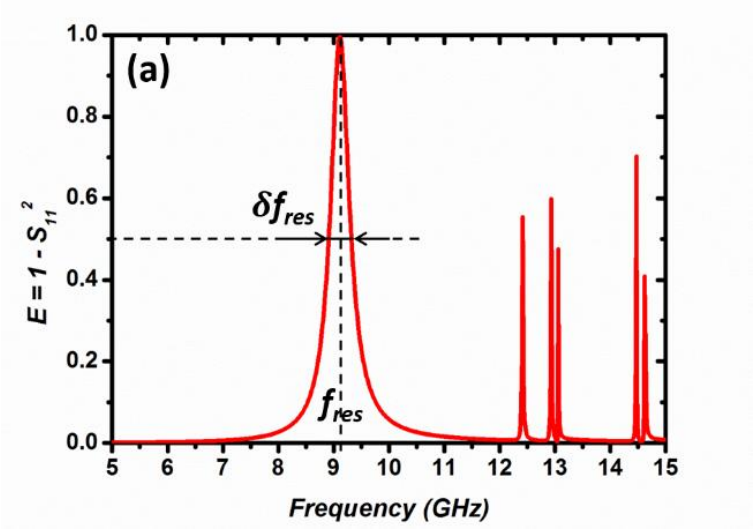

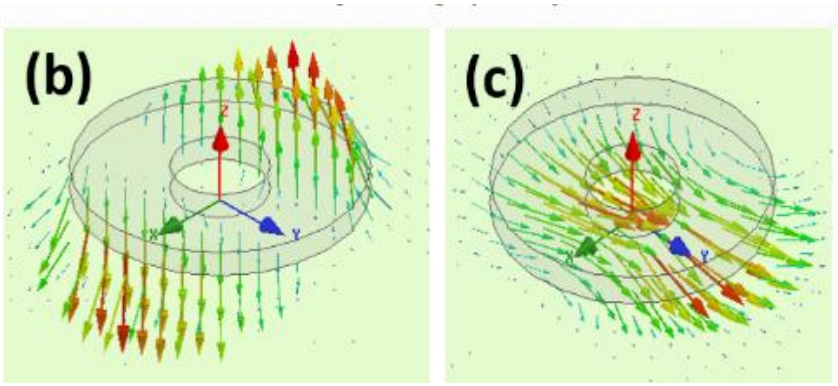

Fig. 3.2.2 (a) Extinction spectrum simulated for a periodic array of rings deposited on a metal-coated Epoxy substrate. The fundamental magnetic resonance mode occurs at 9.11 GHz as illustrated by the field maps showing (b) the electric field vector and (c) the magnetic field vector. These maps are plotted in the mid plane between the steel ring and the ground plane.

The optimized period was investigated both in simulation and experiment. For the latter, the measurements have been carried out by means of free space Vector Network Analyzing (VNA). The analyzer is connected to rectangular horn antennas through coaxial cables and coaxial-to-rectangular waveguide transitions. A schematic of the experimental configuration is shown in Fig. 3.2.3 (a). This setup has been calibrated using the TRL (Thru-Reflect-Line) method in the output plane of the waveguide transitions. Only the reflection coefficient under normal incidence has been measured here. Therefore, only one horn has been used to radiate the incident wave and measure the reflected one. The distance between the horn aperture and the under test sample was set to 16 cm as a trade-off between the dimensions of the metamaterial substrate and the horn radiation pattern. This structure, spatially limited to the surface of the grounded epoxy substrate (21 × 29.7 cm^2), was surrounded with commercial absorbing foam (EcosorbAN 77) in order to alleviate the influence of parasitic reflections. A normalization process has been performed by taken into account the reflected signal measured from a bare back-grounded substrate. From the reflection measurements, the absorbed power A can easily be deduced by applying the following equation: $A = 1 - |S_{11}|^2$, where S_{11} is the magnitude of the reflection coefficient for an impinging electric

field polarization along the small side of the horn antenna. In this definition, by considering a quasi-plane wave illumination under normal incidence, the multi angle back-scattering contribution is neglected. The metallic rings have been aligned along grids whose period varies from 16 to 72 mm. From the numerical side, for period larger than 35 mm, the simulations show a multimode pattern leading to a multi-peak response, explaining why the numerical data were only plotted around the optimal period. A comparison between simulated and experimental peak absorbance is shown in Fig. 3.2.3 (b). Both measurement and simulation results point out that the optimized period is around 24 mm for the periodically arrayed ring absorber.

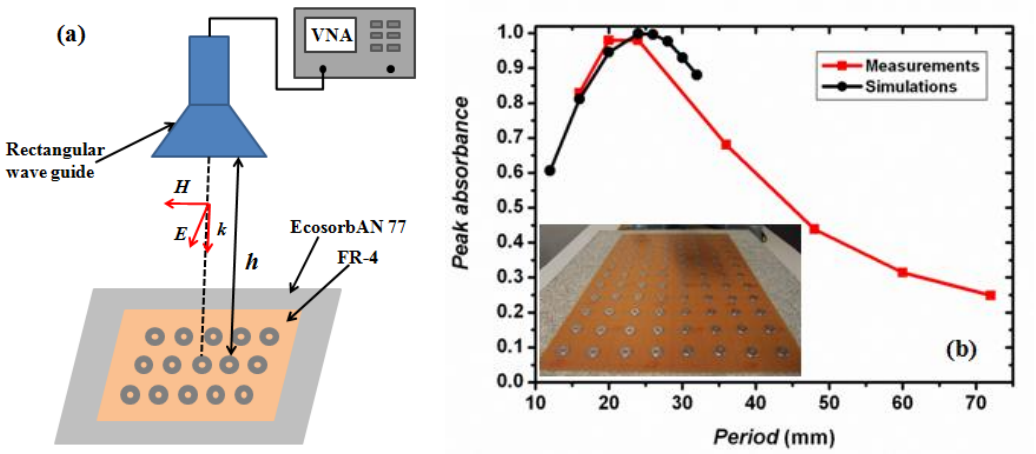

Fig. 3.2.3 (a) Schematic of the measurement equipment operating in X-band, (b) Peak absorbance detected around 9 GHz as a function of the array period. Insert is a photograph of a measured array.

In a more general way, as detailed in chapter 2, the optimal absorbance can also be explained by the concept of critical coupling of an open resonator given by the following set of equations [22]:

$$Q^{-1} = \frac{\delta f_{res}}{f_{res}} \tag{3-1}$$

$$Q^{-1} = Q_{leak}^{-1} + Q_{diss}^{-1} \tag{3-2}$$

$$Q_{leak}^{-1} = Q_{diss}^{-1} \quad (3\text{-}3)$$

The quality coefficient Q given in equation 3-1 as the inverse ratio between the resonance frequency f_{res} and the Full Width at Half Maximum (FWHM) δf_{res}, is a direct expression of the absorption bandwidth. It involves two distinct contributions. The first one stems from the loss term given by Q_{diss}. As the metallic losses can be neglected at the operating frequency, the loss process is located into the dielectric substrate and thus Q_{diss} is inversely proportional to the Epoxy dielectric loss tangent. The second one, given by Q_{leak}, is a quality coefficient describing the coupling between the impinging wave and the resonating structure. This term refers to the spatial configuration of the field and depends on the periodicity of the structure. Satisfying equation (3-3) yields an optimal period for a given loss tangent value in order to get a maximal absorbance. Considering the Epoxy loss tangent tan (δ) = 0.02, and assuming the balance condition between Q_{leak} and Q_{diss} to be satisfied, the value of Q equals 25, which is consistent with the ratio $f_{res}/\delta f_{res}$ deduced from the graph of Fig. 3.2.2 (a).

Let us remind that we choose to use the term extinction instead of absorption in order to alleviate any ambiguities about diffuse reflection. Obviously the reflection on a periodic metamaterial interface is specular as long as the periodicity remains small with respect to the working wavelength. In this case, extinction and absorption are equivalent. Nevertheless, in order to remain general and for an ease of comparison between the behaviors of periodic and random structures, especially under oblique incidence, we chose to keep extinction as a key parameter. Considering the fact that the magnitude transmission coefficient S_{21} naturally cancels due to the presence of the ground plane, the power extinction coefficient E can be written as follows:

$$E = 1 - S_{11}^2 \quad (3\text{-}4),$$

where S_{11} stands for the magnitude reflection coefficient.

To sum up at this stage, an evidence of a ground magnetic resonance is afforded by the *out of plane* E-field pattern displayed in Fig. 3.2.2 (b) that illustrates the displacement current within the dielectric layer with opposite signs at the edges. Such an anti-parallel configuration of displacement currents yields the localization of the *H*-field within the resonator corresponding to an *in-plane* magnetic dipole such as depicted in Fig.2.2.1 As seen in the following devoted to position disorder arrays, a lift of degeneracy of the magnetic resonant frequency will be achieved by the strong interaction between the magnetic dipoles of neighbored resonators in close proximity. This will explain a distribution of the resonant frequencies that depends on the strength of the coupling (broader absorption window) that has to be compared to the single resonance mode of regular periodic array. Higher resonance modes of the elementary particle can also contribute to the absorption mechanism, depending on the geometrical ratio of the resonator. However, in this study we focus on the fundamental mode whose signature is easily identified on the *E*-field maps. Beyond this fundamental resonance signature, several additional peaks starting around 12.5 GHz can also be observed in the extinction spectrum. Let us recall that the simulated structure which is a unit-cell bounded by perfect electric and magnetic mirrors condition leads to the model of an infinite square array with a 24 mm period. It is well known that such a structure also leads to array resonances whose frequencies are close to the Rayleigh values [23]. The first resonance frequency of the array is given by the following expression:

$$f_R = \frac{c}{p} \tag{3-5}$$

Where c is the speed of light and P is the period of the array.

Indeed considering a period of 24 mm, f_R equals 12.5 GHz. For this frequency as the period matches the working wavelength, diffuse reflection phenomenon is expected as discussed above. However, considering the situation of a disordered or a periodic array such as the ones we assessed experimentally, our main interest is focused on the

former magnetic resonance.

3.2 .2 Influence of incidence angle

Simulations under oblique incidence have been performed since insensitivity of the absorber performance is one of the key issues in potential application. In this case, the super-cell is bounded by *master-slave* type conditions, as shown in Fig. 3.2.4. By using these master slave boundary conditions, the ring resonator was virtually arrayed both in *x* and *y* direction in *x-y* plane. The titled incidence dependence absorption spectra as a function of frequency were given in Fig. 3.2.5 both for *TE* and *TM* polarization.

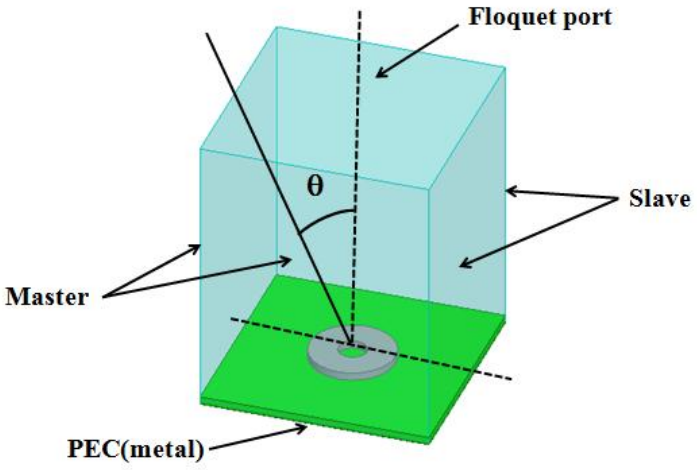

Fig. 3.2.4 Schematic of the incidence angle definition and the simulation conditions.

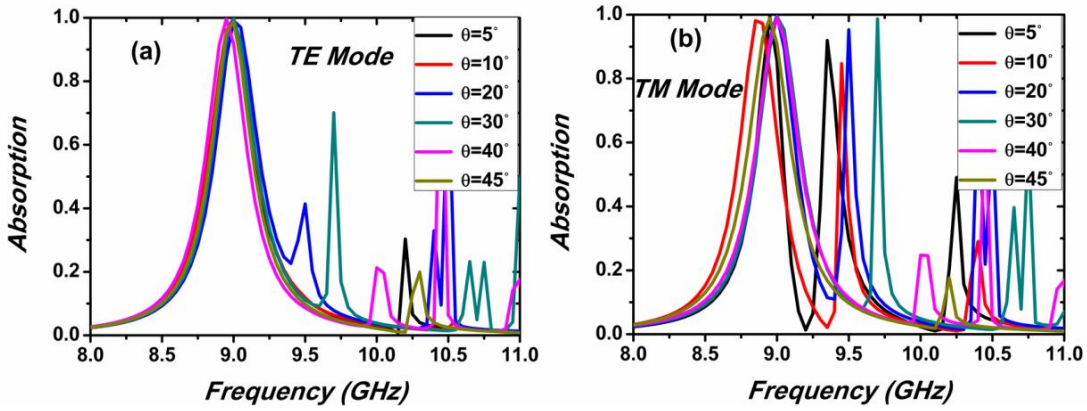

Fig. 3.2.5 Absorption spectra with respect to frequency (a) for *TE* mode, (b) for *TM* mode.

From Fig. 3.2.5, we can find that, the absorption keep unit at resonance frequency even when the incidence angle increase up to 45 ° both for *TE* and *TM* mode. Also there are several additional peaks at higher frequency region called cavity resonance which is investigated in chapter 3.2.1 in details. For *TM* mode, when the incidence angle varied, the resonance frequencies have a little bit shifts ~ 0.25 GHz. It can be explained that, at this frequency is a magnetic resonance the incident magnetic field is always parallel to the resonators while the transverse component of the *k* vector changes which lead to a ratio between the parallel wavelength and the ring size.

The measurements under oblique incidence have been carried out by means of a free space Vector Network Analyzing (VNA). However here, the analyzer is connected to two rectangular horn antennas through coaxial cables and coaxial-to-rectangular waveguide transitions. The horns are guided on semi-circle arm whose radius equals to 85 cm. The schematic of the experimental set-up is shown in Fig. 3.2.6 (a). This setup has been calibrated using the TRL (Thru-Reflect-Line) method in the output plane of the waveguide transitions. In addition, we used the measurement method as the one explained in chapter 2, by switching to the time-domain windowing process during the measurement to prevent any parasitic signal resulting from the direct path between antennas. The angular measurements have been performed under *TE* and *TM* polarization of the ring array with optimized period 24 mm.

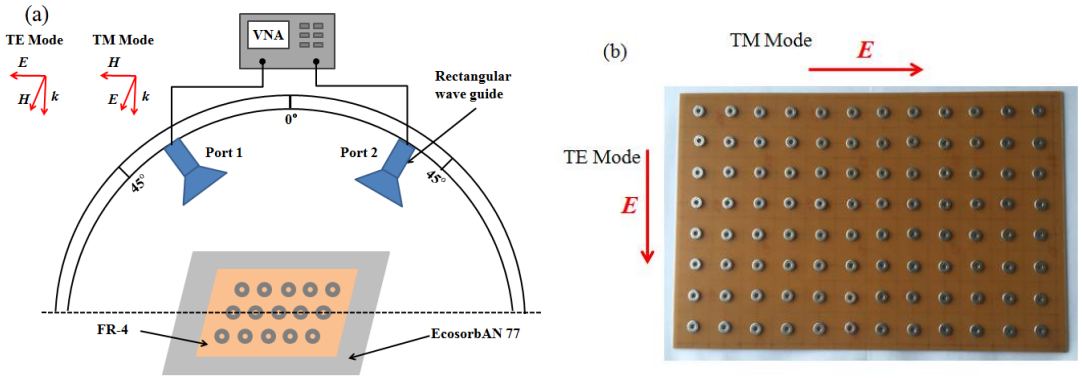

Fig. 3.2.6 (a) Schematic view of the experimental set-up, (b) Photograph of the measured period rings

array.

During the measurement process, first we measured the reflection of the bare substrate as the reference, and then the metallic rings were aligned on a grid whose periodicity equal to 24 mm both along *x* and *y* direction, and this periodicity can lead to a maximized extinction coefficient as previously discussed. It should be noted that the number of resonators was 96 with 8×12 lines. The electric field is aligned along the 8 and 12 rings direction for *TE* and *TM* modes respectively (Fig. 3.2.6 (b)). In this case, the final wave extinction of the metamaterial structure is:

$$E = E_S - E_{Ref} \qquad 3\text{-}6$$

where E_S is the wave extinction of the substrate with ring resonator on top, and E_{Ref} is the wave extinction of the bare back-grounded. Finally, the measurement results of the wave extinction for the *TE* and *TM* mode without and with time-domain process were shown in Fig. 3.2.7 (a) to (d).

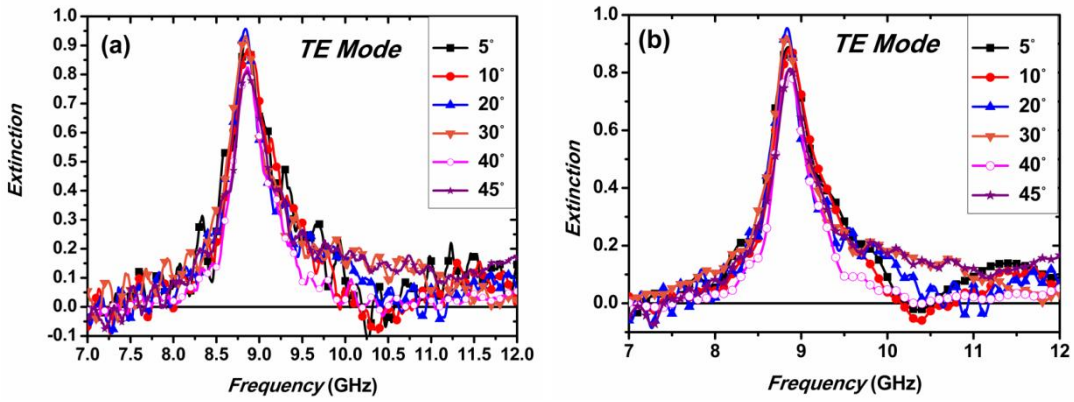

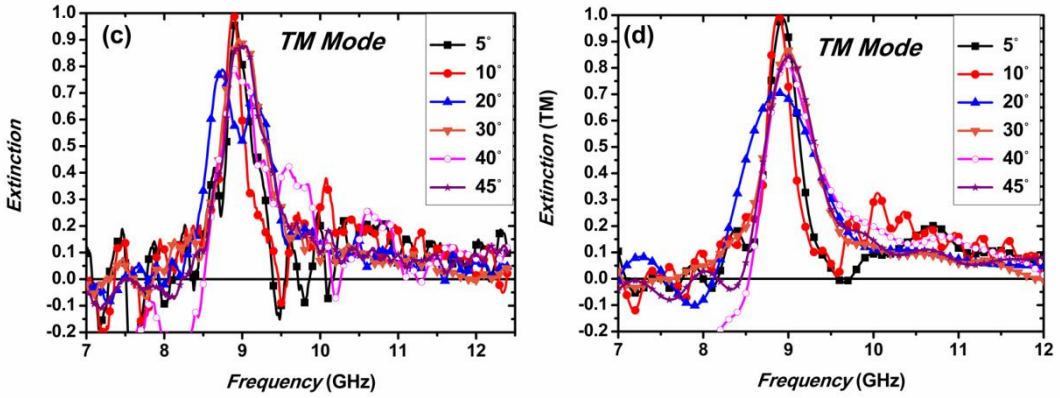

Fig. 3.2.7 Wave extinction (a) for *TE* mode without time-domain process, (b) for *TE* mode with time-domain process, (c) for *TM* mode without time-domain process, (d) for *TM* mode with time-domain process.

The peak extinction, predicted around 9 GHz by simulation is confirmed by the experiment both for *TE* and *TM* polarization. However, a slight reduction of the extinction value down to 96 % should be noted. This can be attributed on one hand to the small number of patterns illuminated by the impinging wave [8] and on the other hand to the fact that the measurements have been performed with a minimum angle of 5 °, which does not reproduce the normal incidence condition of the simulations. In practice, this minimum angle is the consequence of the size of the horn antennas. When the angle is increased from 5 °up to 45 °the peak extinction does not show any relevant frequency shift for *TE* polarization. In addition its value remains larger than 80 %, which shows that the impinging electromagnetic energy remains predominantly coupled to the magnetic resonance mode and dissipated within the dielectric interlayer.

When comparing the results with and without time-domain windowing process, it is clear to that this post-measurement treatment via Fourier transform is more or less efficient by notably depending on the windowing parameters that have been chosen during the measurement process. As a general rule the influence of this post-treatment is weak as seen in the Fig. 3.2.7 (b) and (d), especially for the *TE* mode. However smoother frequency variations can be achieved as exemplified by the comparison of the *TM* modes results.

Also it is worth mentioning that the calibration is only valid within the 8 to 12 GHz frequency band. Therefore, any measurement out of this range can only provide qualitative information. As an example of this limitation, it can be noted that negative extinction was achieved when the frequency is lower than 8 GHz. It is believed that such an error is related to the waveguide cut-off effect. On the other hand, owing to a reference calibration for a unit reflectivity carried out in free space one can expect a higher impact of the calibration error in a high reflectivity regime

3.3 Random meta-material based absorbers

The previous comments point out the difference between the metamaterial regime which takes benefit of strong field localization at the vicinity of an isolated resonator and the array resonances based on the seminal works of Rayleigh and Wood [2, 3]. The isolated resonator approach seems to be valid in many cases since the fields are strongly localized and the period of the array is several times the elementary size of the resonator in order to satisfy the impedance matching criterion [4]. However, introducing positional disorder from a periodic structure, by changing inter-particle distances, can introduce coupling forces between each resonator leading to the occurrence of extended resonance modes. The analysis and the role of these modes in the extinction response of a random metamaterial will be discussed in the next section.

3.3.1 Influence of the coupling forces between resonators in random meta-materials

Based on the period process, we choose a unit-cell such as the one defined previously, i.e. surface 24×24 mm^2, perfect mirrors as boundary conditions, but where the resonator is no more centered within the basic cell. Its coordinate values are randomly generated along the x and y axis, and 10 different positions have been considered. For sake of clarity, only 5 spectra are superimposed in Fig. 3.3.1.

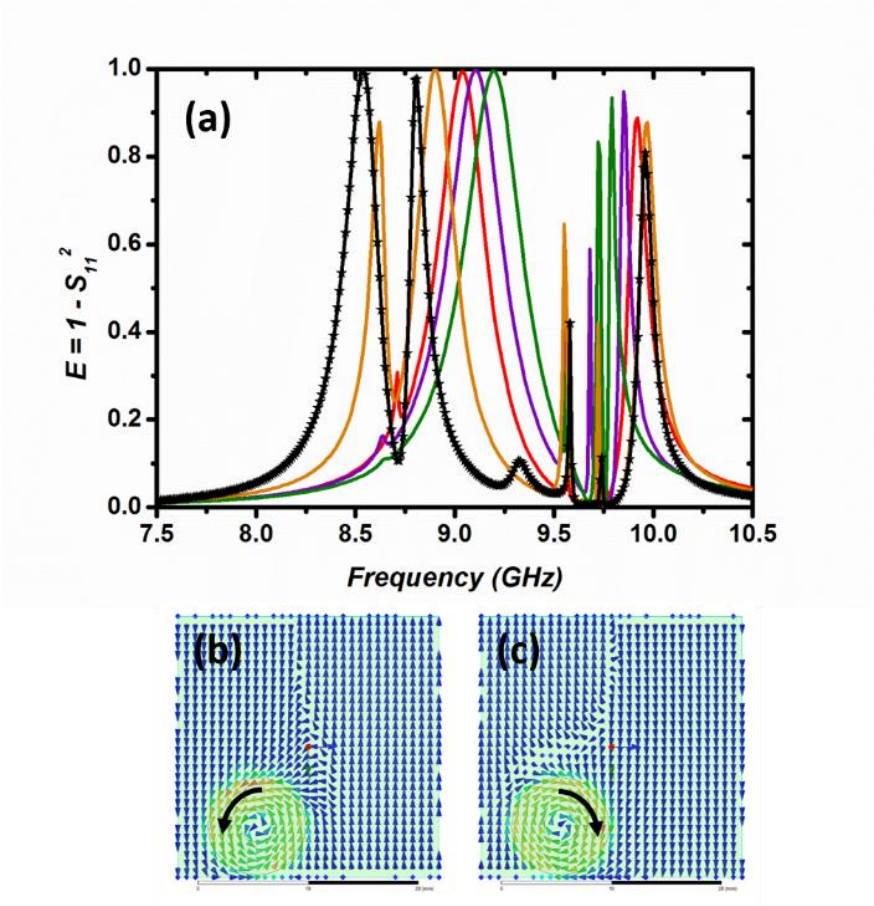

Fig. 3.3.1 (a) Extinction spectra for 5 different positions of the ring resonator within a 24 x 24 mm^2 unit cell bounded by perfect mirror conditions. The Poynting vector is plotted in the dielectric mid-plane, for the configuration corresponding to the black-dotted curve, at each maximum: (b) 8.54 GHz, (c) 8.81 GHz.

First, as previously commented, two different phenomena can be observed, namely the magnetic resonances localized around 9 GHz and the array resonances whose high orders are visible from above 9.5 GHz. In fact, the first order resonance is located at 6.25 GHz which is out of the scale considered in figure Fig. 3.3.1(a). This red-shift is the consequence of the doubled period introduced by the mirror boundary conditions. Indeed, as described in [24], when the elementary particle moves along one direction to the edge of the unit-cell, this introduces a dimer configuration. As a consequence, the period of the dimer array is twice as large as the one of the centered particle array. Focusing on the former magnetic resonance mode, it is worth mentioning

that the peak frequency shift can be either positive or negative according to the nature of the coupling force. Indeed, numerical simulations show that when the resonators get closer along the direction of the magnetic field the resonance frequency decreases due to the end-to-end coupling of the magnetic dipoles. On the contrary, when the resonators get closer along the direction of the electric field, the repulsive coupling force between the magnetic dipoles leads to an increase of the peak frequency. This phenomenon has already been analyzed in detail in case of dielectric Mie resonators [5] and metallic SRRs [6]. As a first step to the analysis of a random array, in Fig. 3.3.1 we consider that the metallic ring can be randomly positioned within the whole unit cell and the alignment along the directions of the incident electric and magnetic field vectors are not considered separately. The main conclusion of this first numerical experience is the fact that the resonance can be tuned over a frequency band of typically 8 % by keeping the peak of extinction close to unity. Depending on the coupling distance, a secondary peak may occur such as depicted in the dotted black curve where the two peaks located at 8.54 and 8.81 GHz are close to one. This effect, expected in case of strong coupling between two resonators, is illustrated by the Poynting vector plots of Fig. 3.3.1(b) and Fig. 3.3.1(c), and probed in the dielectric mid-plane. One can observe that the magnetic resonance mode splits into two different states, each one being characterized by a rotation direction of the Poynting vector: clockwise at 8.81 GHz and anti-clockwise at 8.54 GHz. This splitting effect along with the tuning effect observed in case of weaker coupling will both contribute to a broadening of the extension spectra in random metamaterial absorbers.

3.3.2 Influence of the filling factor in random metamaterials

In this part, we will investigate how the filling factor works during the designing of the random PMA. Here we define the filling factor $Q_f = S_{ring}/S_{sub}$, where S_{ring} is the area of the ring resonators and S_{sub} is the area of the substrate.

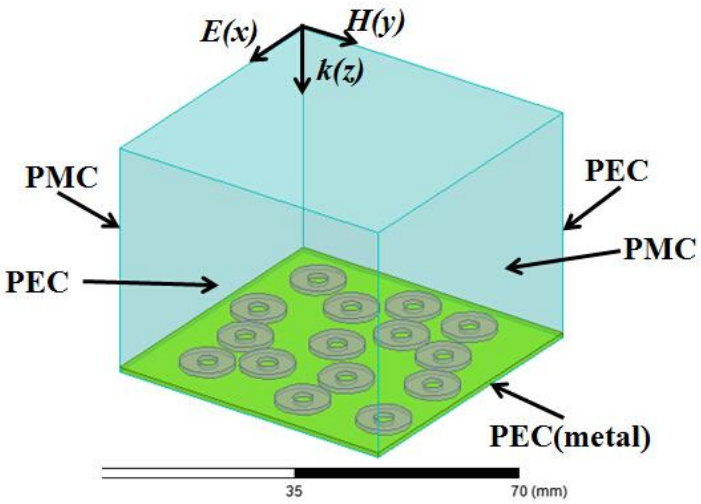

Fig. 3.3.2 Schematic of the resonators randomly position on the FR-4 substrate and the simulation conditions

In the simulation process, several rings randomly positioned onto the FR-4 substrate form a super-cell and perfect mirror boundary conditions were used, as it is shown in Fig. 3.3.2. The substrate with area of 48 x 48mm^2 is kept constant and the number of rings was increased to change the Q_f from 10% to 40%. For each filling factor we considered three configurations, namely three different random distributions. For an unambiguous analysis of the electromagnetic coupling influence, physical contacts between the rings are forbidden in this numerical experience. The numerical results are shown in Fig. 3.3.3.

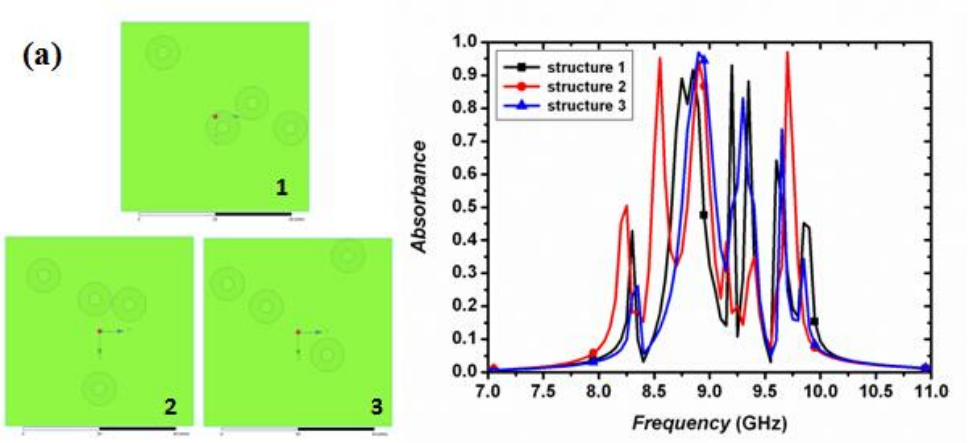

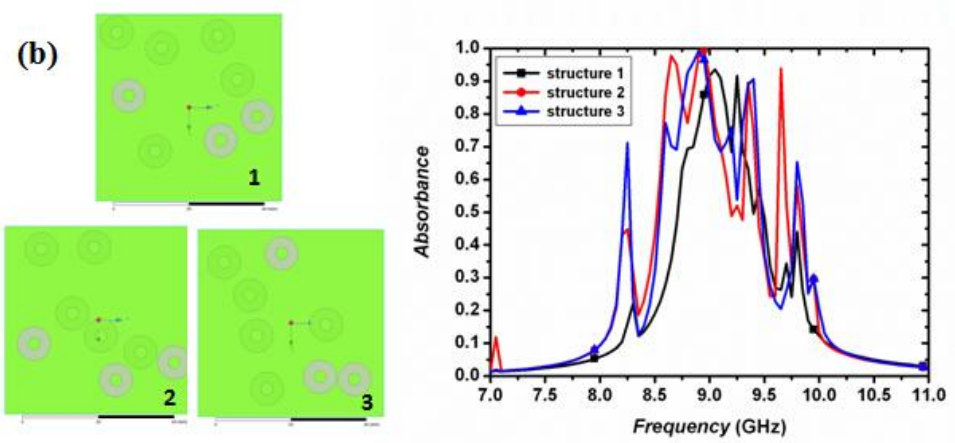

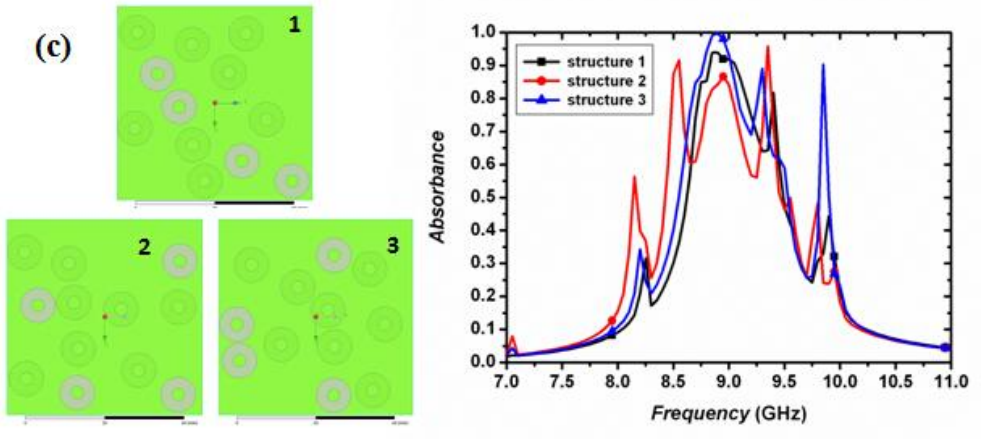

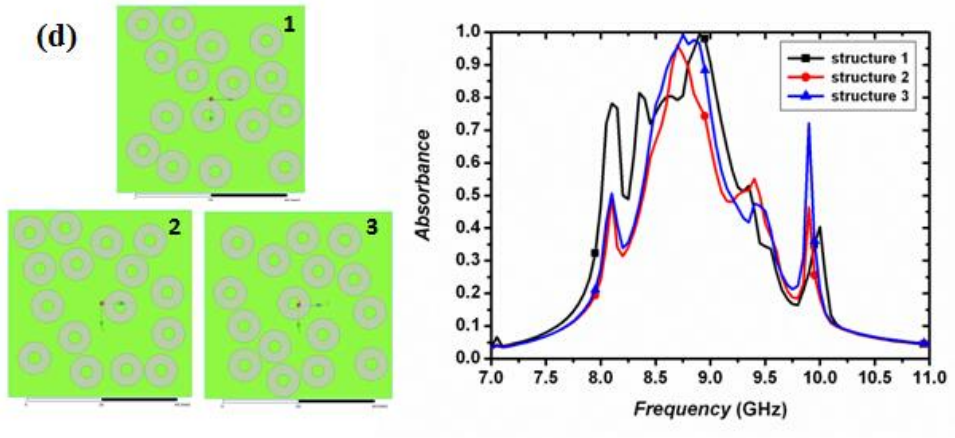

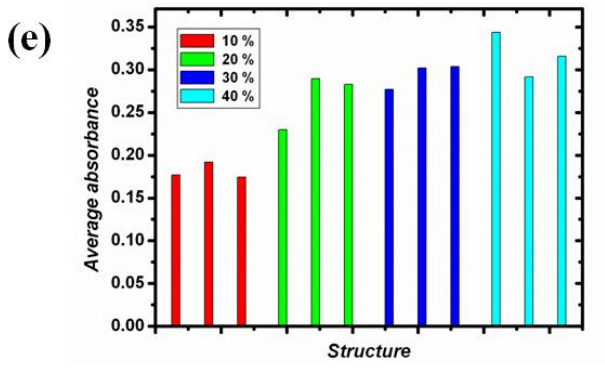

Fig. 3.3.3 Extinction spectra simulated for various filling factors within a 48 x 48 mm^2 unit cell bounded by perfect mirror conditions and the distribution of the various cases (a) 10 %, (b) 20 %, (c) 30 % and (d) 40 %. (e) Average extinction calculated between 7 and 11 GHz for the various case depicted in Fig. 3.3.3 (a) to (d).

For a filling factor equal to 10 %, additional peaks occur on both side of the 9 GHz absorbing frequency. This behavior can be related to the coupling between neighboring resonators, as described and analyzed previously. When the filling factor is increased from 10 % (Fig. 3.3.3 (a)) up to 40 %, (Fig. 3.3.3 (d)), the multi-peak extinction spectra moves towards a mini-band as a consequence of the merging of the numerous frequency localized responses. This mini-band remains centered around 9 GHz which is the former magnetic resonance frequency of a single resonator. Moreover, at this central frequency, extinction coefficient remains close to unity suggesting an increasing of the average extinction. This tendency is confirmed by the graph depicted in Fig. 3.3.1 (e), where the average extinction over the 7 to 11 GHz frequency band has been plotted for the drawing simulated in Fig. 3.3.3 (a) to (d). It can be seen that the average extinction is gradually increased by a factor of 2:1 when the filling factor increases from 10 % up to 40 %. Let us recall that for every random simulated structure so far, the contact between elementary ring patterns has been forbidden. Therefore, the broadening effect is only the consequence of the electromagnetic coupling effects between close resonators.

3.3.3 Influence of the contact between elementary rings

Physical contacts between ring patterns, allowing the setting up of multi-ring clusters, have been introduced in this part. The super-cell whose area is 48 x 48 mm^2 has been bounded with perfect mirror conditions, and two different configurations have been considered. Simulation results were reported in Fig. 3.3.4, illustrated by the field-maps of Fig. 3.3.4 (b) and (c) for the first configuration, and 4 (d) and 4 (e) for the

other one. These pictures show the top view of the structures simulated under normal incidence, with the incident electric field along the vertical direction.

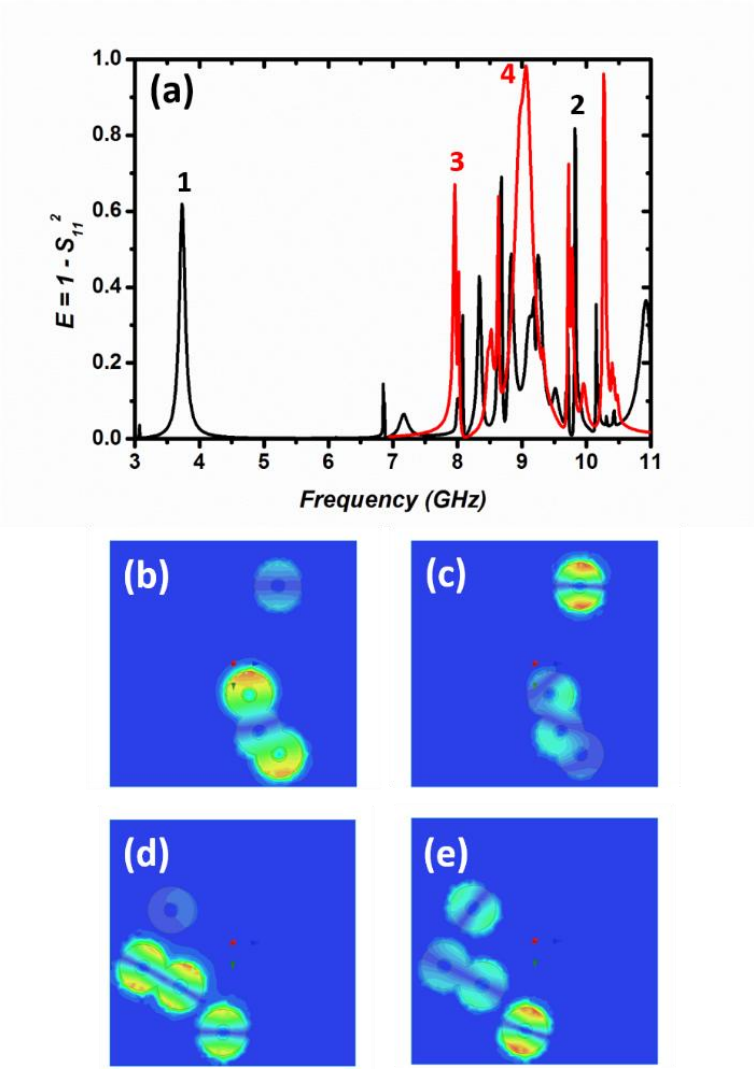

Fig. 3.3.4 (a) Extinction spectra for various position of four ring resonators within a 48 x 48 mm^2 unit cell bounded by perfect mirror conditions. The E-field magnitude is plotted in the dielectric mid-plane, for the configuration corresponding to the black curve at (b) 3.73 GHz (marker 1), (c) 9.82 GHz (marker 2) and configuration corresponding to the red curve at (d) 7.96 GHz (marker 3), (e) 9.06 GHz (marker 4)

The response of the first structure plotted in black (Fig. 3.3.4 (a)) shows a first extinction peak larger than 0.6 at 3.73 GHz (marker1). The related electric field-map (Fig. 3.3.4 (b)) illustrates the role of the three rings cluster which is able to support a

low-frequency mode. This mode is characterized by a single *E*-field node in the middle of the cluster with a concentration of the electric field at the edges of the external rings. As a consequence, the resonating length is increased yielding a red shift of the magnetic resonance. At this frequency, the isolated ring whose fundamental resonance frequency is located at 9.82 GHz is weakly excited. Such a behavior can be useful for the design of practical absorbing media in order to alleviate the barrier of wide surface structures when addressing low frequencies. It is important to note that the expected peak at 9 GHz, describing either periodic or highly diluted disordered array is almost canceled for this configuration. In addition, another peak, resulting of the joint contribution of the cluster and isolated ring (see Fig. 3.3.4 (c)) can be evidenced at 9.82 GHz (marker 2). The second configuration features a two rings cluster and two isolated rings. As a first remark, the field maps show that the contributions of the two isolated rings to the frequency response are very different. This can be explained by considering their specific electromagnetic environment. Indeed, the ring located in the bottom of the super-cell is strongly coupled to its neighboring image through the bottom perfect electric mirror whereas the other isolated ring, rather centered along the vertical direction is submitted to a much weaker coupling influence. The joint resonance of the two ring cluster along with the lower first isolated ring is at the origin of the 7.96 GHz peak depicted in Fig. 3.3.4 (a) (marker 3). Unlike the first configuration response, the extinction around 9 GHz remains important here (marker 4). The field map depicted in Fig. 3.3.4 (e) illustrates the weak influence of the two-ring cluster for this frequency peak.

3.3.4 Oblique incidence influence

The numerical results commented so-far are related to extinction spectra under normal incidence condition. In addition, simulations under oblique incidence have been performed. In this case, the super-cell is bounded by *master-slave* type conditions. This means that the electromagnetic field is reproduced from the master plane to the slave

plane with a user-defined phase constant. Therefore, the infinite media is defined in *x*-*y* plane by reproducing the super-cell geometry following a translation process. The 48 x 48 mm^2 super-cell features 15 randomly positioned resonators (see Fig. 3.3.5 (b) and (c)). Fig. 3.3.5 (a) depicts the extinction spectrum versus frequency for an incidence angle swept between 0 to 60 ° under *TM* polarization. In other words, the incident magnetic field remains parallel to the metamaterial plane for every angle value. First, it should be noted that the extinction remains close to unity around 9 GHz for each incidence angles. For these simulations performed under oblique incidence, we only considered the specular reflection coefficient retrieved from the fundamental Floquet mode. This makes sense since the average distance between nearby resonators is very small with respect to the working wavelength which tends to forbid the multi-directional reflection phenomenon. Nevertheless, for this super-cell configuration, one has to pay attention to the Rayleigh frequencies introduced by the in-plane periodicity. This periodicity can contribute to the sharp features located around 10 GHz as observed in Fig. 3.3.5 (a) for similar dimensions of the super-cell. In addition, when looking at the field maps of Fig. 3.3.5 (b) and (c), one can notice a distribution of the magnetic dipole orientation resulting from the various coupling situations between nearby resonators. Because of this azimuth angular distribution, one can be concerned about depolarization effects when the incident plane wave interacts with the disordered metamaterial structure. However, this effect is also very marginal as shown in Fig. 3.3.5 (d) which includes in the same graph the extinction coefficients for both *TE* and *TM* modes and the cross-polarization reflection terms as a function of the incidence angle. These four coefficients have been averaged over the 7-11 GHz frequency band.

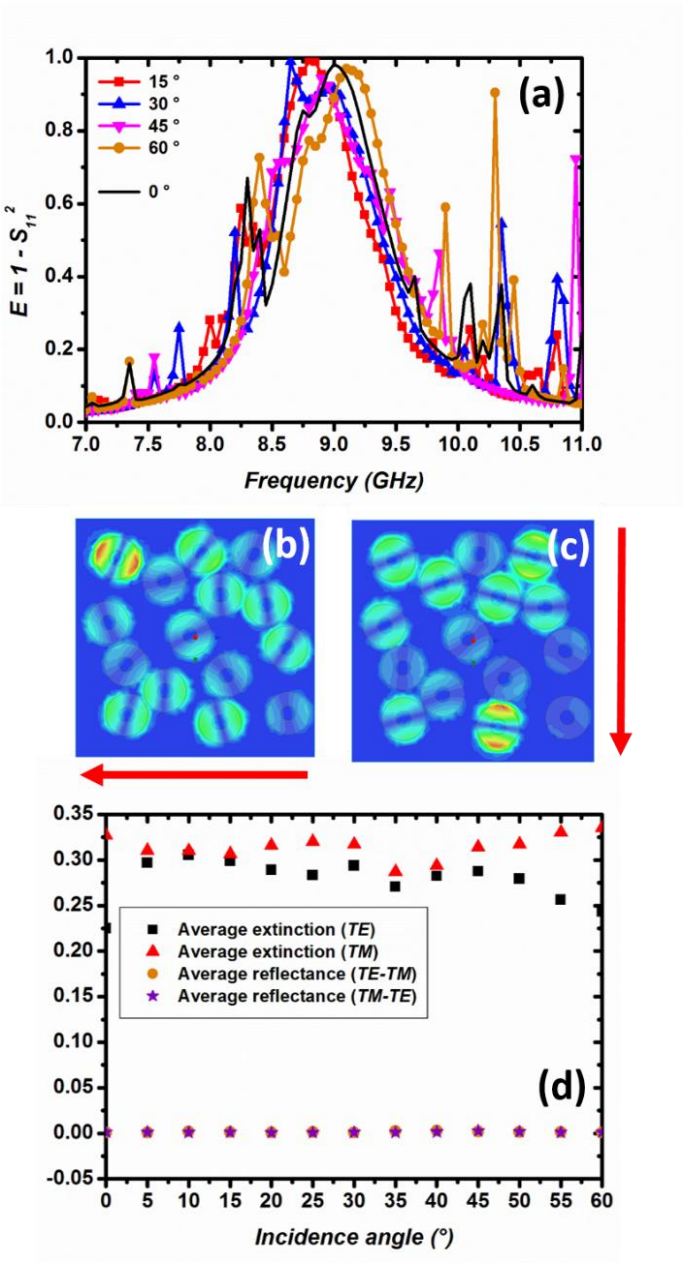

Fig. 3.3.5 (a) Extinction spectra versus frequency under oblique incidence (*TM* mode) for a 48 x 48 mm^2 unit-cell including 15 resonators and bounded by master-slave conditions, *E*-field magnitude in the dielectric mid-plane at 8.9 GHz and 15 ° incidence angle for *TE* (b) and *TM* (c) polarization, incident E-field direction shown by red-arrows, (d) average extinction spectra versus incidence angle plotted for both polarization directions along with the average cross-polarization reflectance.

We can note that the cross polarization terms remains close to zero between 0 °and 60 ° incidence angle. The fact that both the non-specular and cross-polarization terms

remain insignificant when the incidence angle is increased shows that the main contribution to the extinction property is the absorption by means of the magnetic resonance mode described in Fig. 3.3.5. Both the *TE* and *TM* average extinction coefficients are comprised between 0.25 and 0.35 and their curves tend to diverge for large incidence angles, typically above 45 °. This behavior is expected as mentioned in [7] since in *TM* polarization, the direction of the magnetic field remains unchanged and can efficiently drive the current loop up to large incidence angles.

These simulations results provide a first illustration of the extended modes influence occurring both in case of coupling between nearby resonators and clustering as a consequence of physical contacts. However, let us recall that this numerical study has been conducted by finite elements simulations in a super-cell configuration including 15 rings at the maximum.

3.3.5 Experimental verification

For the experimental analysis reported in the following, the same measurement equipment as shown in Fig. 3.2.1 Schematic of the basic resonator (a) top view with its characteristic parameters (b) Illustration of simulation conditions.

Firstly, we compare the several random configurations to the period array by the extraction of absorption curve. For the measurement of periodic array we set P = 24 mm corresponding to the optimal period while for the random situation, from random 1 to random 4 we disordered the rings more and more as shown in Fig. 3.3.1 (a) Extinction spectra for 5 different positions of the ring resonator within a 24 x 24 mm2 unit cell bounded by perfect mirror conditions. The Poynting vector is plotted in the dielectric mid-plane, for the configuration corresponding to the black-dotted curve, at each maximum: (b) 8.54 GHz, (c) 8.81 GHz. by keeping the number of the rings (96) constant. The measurement results for these four configurations of weak disorder were shown in Fig. 3.3.7.

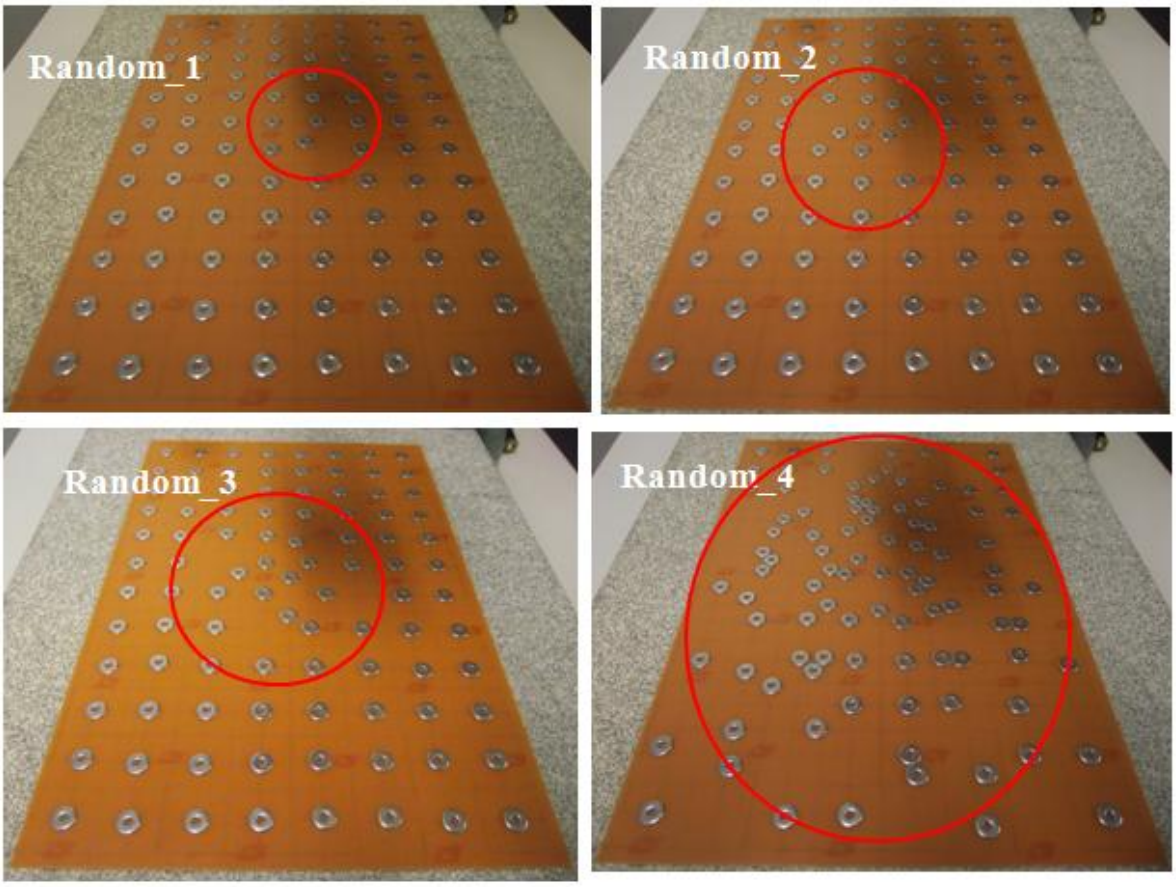

Fig. 3.3.6 Photograph of the measured structure for the 4 random configurations.

From the results reported in Fig. 3.3.7, a strong influence of this disorder can be pointed out with a progressive FWHM enhancement from 14% to 70%. When this delocalization process is randomly extended to the whole substrate area, this broadening effect becomes more and more significant. For instance, the "random 4" distribution gives an enhancement factor of about 80%, which means that the resulting FWHM is almost three times higher than the one measured from the 24 mm periodic array. For some random distributions, the maximum absorbance is sometimes lowered due to a lower local concentration of rings within the illuminating area.

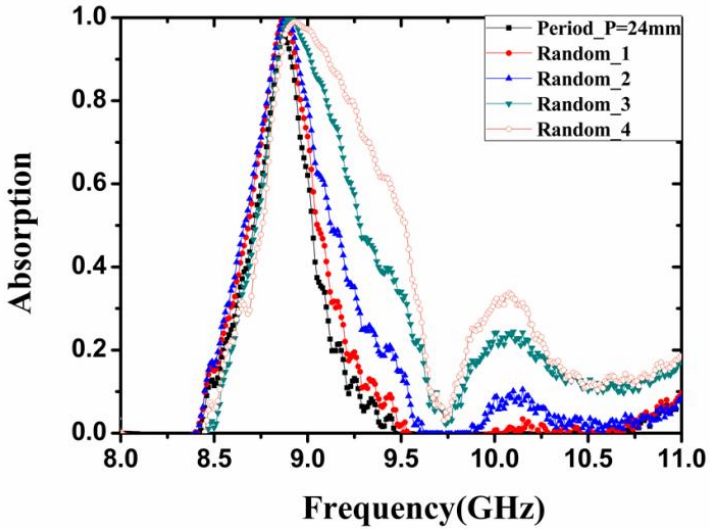

Fig. 3.3.7 Comparison between the optimal periodic case (24 mm) and various random structures by keeping the number of rings (96) constant.

Secondly, we characterized the absorbing layer by increasing the total number of rings from 51 up to 311. The photographs of six distributions with different number of rings are given in Fig. 3.3.8. It was decided to extend the TRL calibration process down to 7 GHz in order to record the whole absorption spectra of highly disordered structures. In this manner, the low frequency attenuation in the short coaxial waveguide component related to the waveguide cut-off was taken into account in the calibration. The results are shown in Fig. 3.3.9.

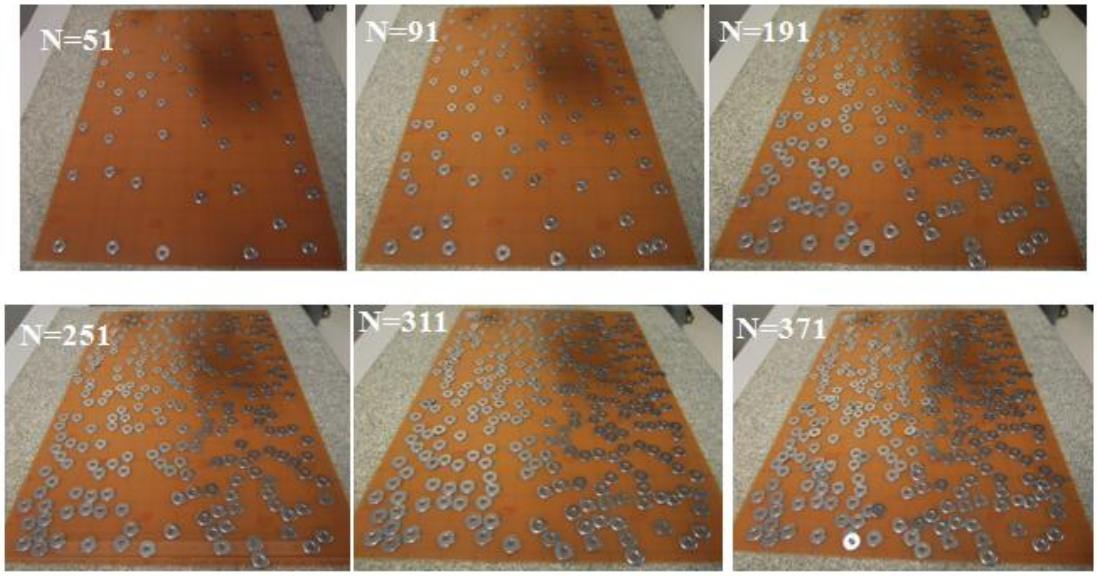

Fig. 3.3.8 Photograph of the measured structure for the six different number rings distribution.

To sum up, a positional disorder strongly contributes to the absorbance band broadening as evidenced in Fig. 3.3.7 and Fig. 3.3.9. This broadening effect increases with the average filling factor of resonating particles. This rule differs from the optimal period property of periodic array that is lost in case of random media. At last, whatever the random distribution considered, it appears that the broadening effect starts from the absorbance peak of a single isolated particle by assuming a negligible dispersion of the ring diameter. Let us remind that this ground resonance corresponds to the first mode of the magnetic dipole involving the conductive currents on the metal parts and displacement currents within the dielectric interlayer. However, from the observation of the characteristics in Fig. 3.3.9, especially the N = 311 and 371 cases, one can note that the absorption spectra are mainly distributed over the main resonance peak located at 9 GHz and over a frequency domain centered around 8.25 GHz. This is presumably interpreted as the contributions of electrically interconnected rings due to their overlap. Actually, clusters of electrically contacted resonators are clearly visible on the photo displayed in Fig. 3.3.8.

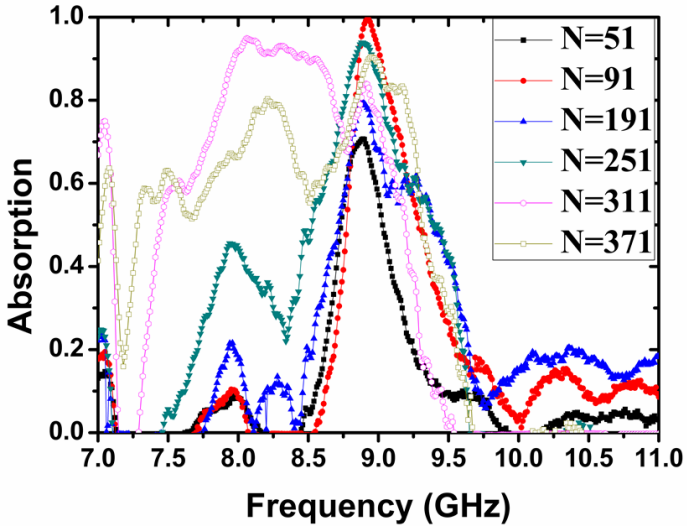

Fig. 3.3.9 Absorbance versus frequency measured for randomly distributed metamaterials structure with number of rings ranging from 51 to 371.

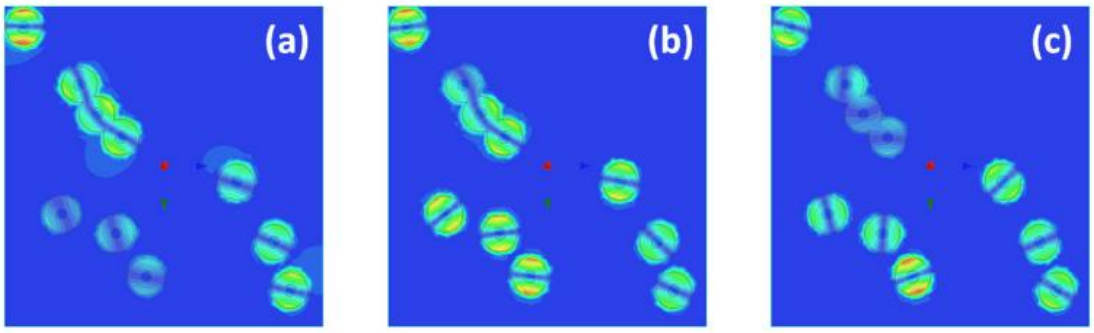

Fig. 3.3.10 Electric field map in the dielectric mid-plane for a random 10 rings super-cell at 7.85 GHz (a), 8.40 GHz (b), and 8.95 GHz (c).

To confirm the contributions of electrically interconnected rings due to their overlap, *E*-field maps were calculated numerically by full wave analysis. They are reported in Fig. 3.3.10. In this situation, we considered a super-cell including 10 rings. Among them, 3 rings are interconnected, thus forming a continuous metallic chain. The other rings are electrically isolated from their neighbors. Around the central frequency of 9 GHz (see Fig. 3.3.10 (c)), the absorption is governed by the resonance of isolated rings. When this operating frequency is shifted down to 7.85 GHz, the role of the 3-ring cluster is clearly illustrated by means of an increase of the mid-dielectric electric field

magnitude.

Finally, we investigated the oblique incidence of the random meta-material perfect absorber structures experimentally. The measurements of the absorption under oblique incidence have been carried out by means of free space Vector Network Analyzing (VNA) by measuring a two horn configuration as described previously. To this aim the analyzer is connected to two rectangular horn antennas through coaxial cables and coaxial-to-rectangular waveguide transitions. In addition as afore mentioned a semi-circle arm with radius equals to 85 cm is used to fix the two horns. A schematic view of the experimental set-up is shown in Fig. 3.3.11. This setup has been calibrated using the TRL (Thru-Reflect-Line) method in the output plane of the waveguide transitions. Besides, we also used here the post treatment time domain analysis as described in chapter 3.2.

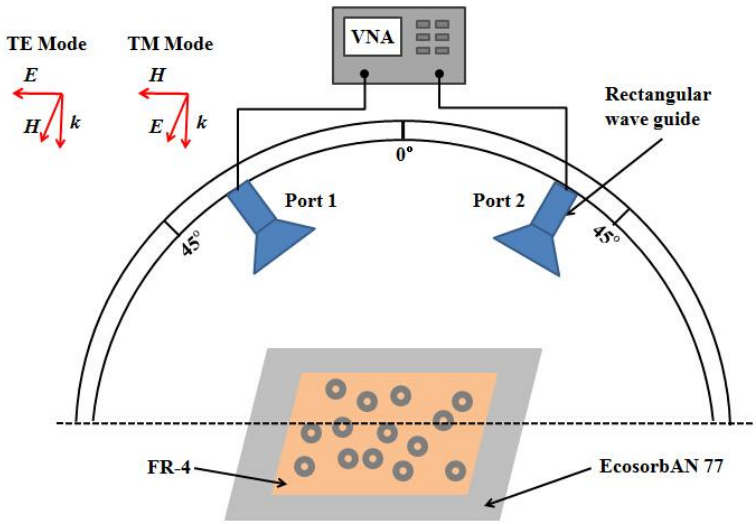

Fig. 3.3.11 Schematic view of the experimental set-up. Be careful: the *TE* mode triedron is also left-handed here.

The angular measurements have been performed under *TE* and *TM* polarization for the random structure with different ring numbers, in practice from 100 to 400 rings. The absorber area was kept constant so that increasing the number of ring was equivalent to an increase of the filling factor. For each distribution the incidence angle

was changed from 5° to 45° by varying the positions of the wave ports. From equation $E = 1 - S_{21}^2$, the absorption of the incident wave under tilted incidence was determined from the frequency dependence of the S_{21} parameter measured between the two horns.

Fig. 3.3.12 shows (a) a photograph of the tested structure. The extinction spectra has been measured for a random structure including 100 rings in a 21 x 29.7 cm^2 area grounded-substrate as a function of the incidence angle (b) *TE* polarization, (c) *TM* polarization. The same kind of experiment was carried out for 200, 300 and 400 ring. The results are displayed in Fig. 3.3.13 for 200 rings, in Fig. 3.3.14 for 300 rings and in Fig. 3.3.15 for 400 rings.

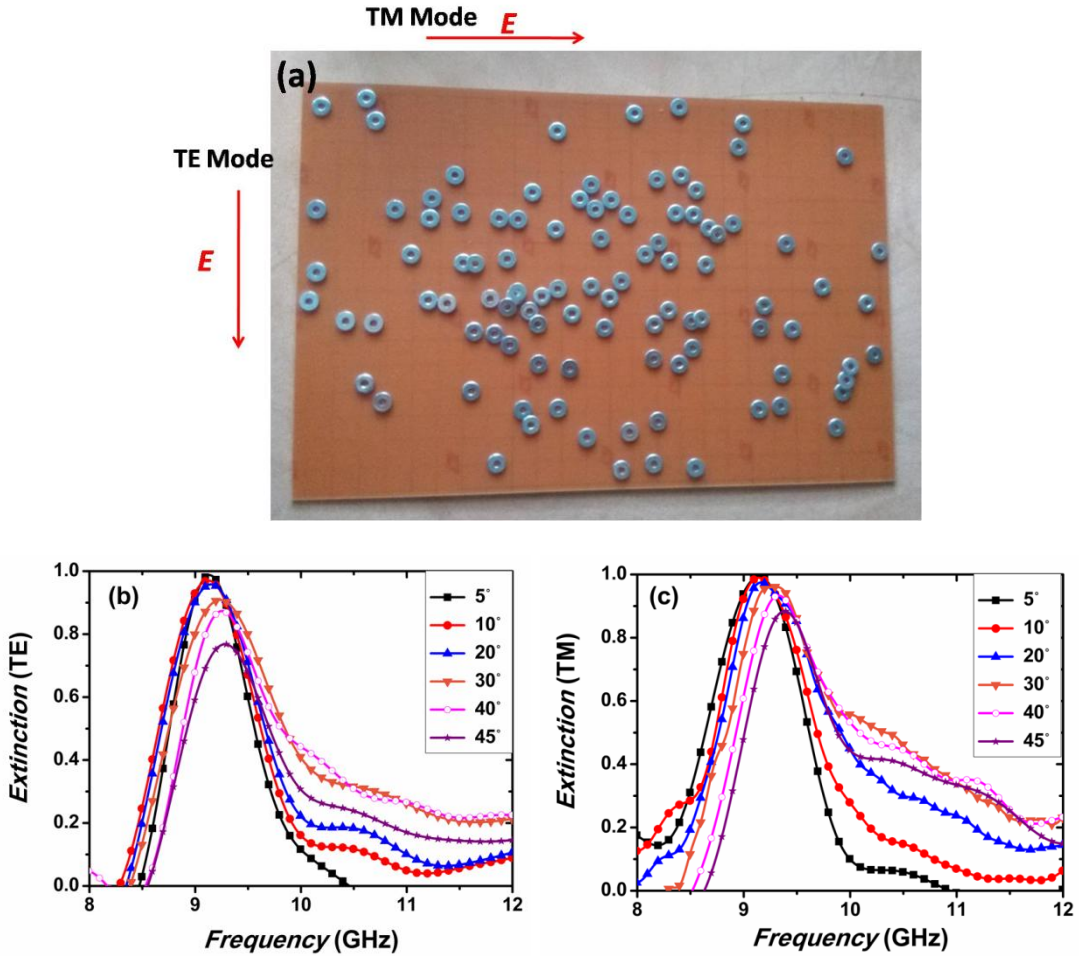

Fig. 3.3.12 (a) Photograph of the tested structure, Extinction spectra measured for a random structure including 100 rings in a 21 x 29.7 cm^2 grounded substrate as a function of the incidence angle (b) *TE* polarization, (c) *TM* polarization.

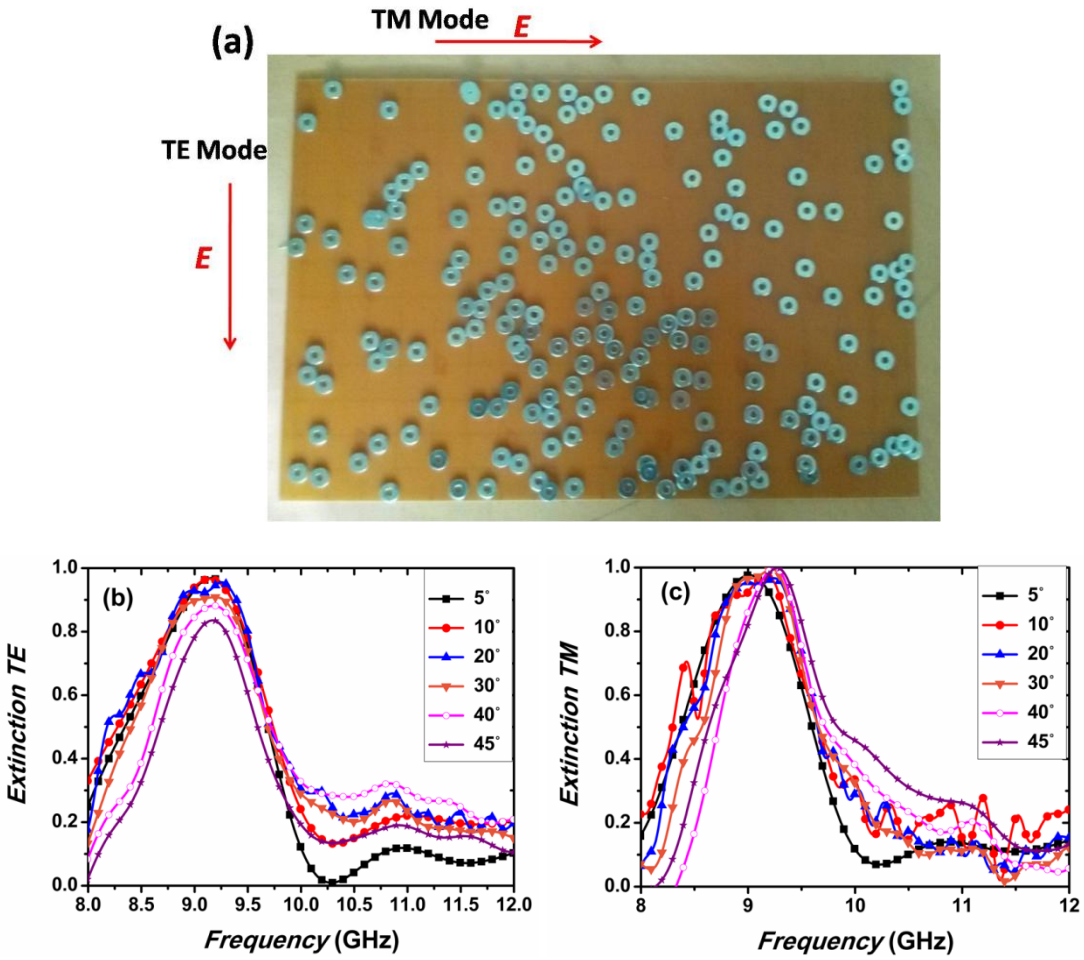

Fig. 3.3.13 (a) Photograph of the tested structure, Extinction spectra measured for a random structure including 200 rings in a 21 x 29.7 cm^2 grounded substrate as a function of the incidence angle (b) *TE* polarization, (c) *TM* polarization.

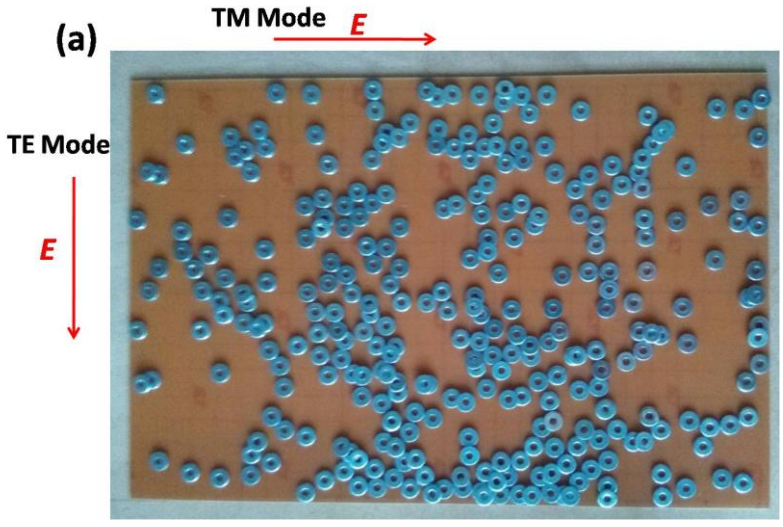

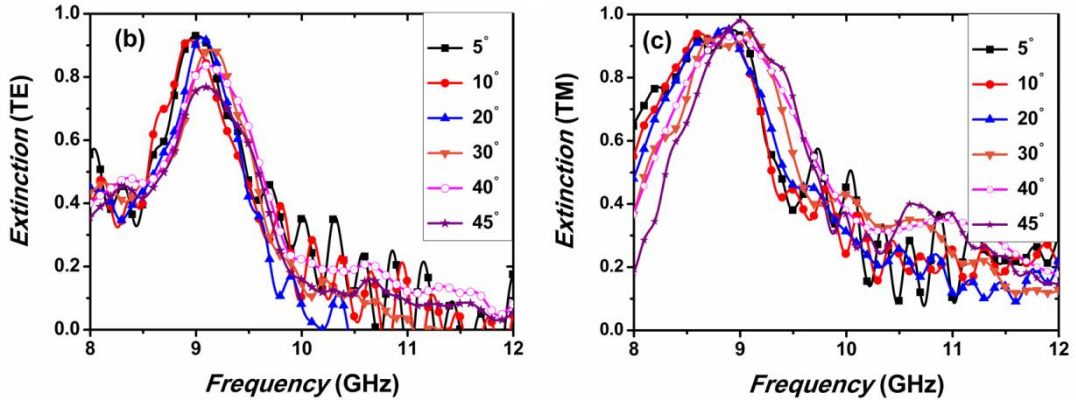

Fig. 3.3.14 (a) Photograph of the tested structure, Extinction spectra measured for a random structure including 300 rings in a 21 x 29.7 cm^2 grounded substrate as a function of the incidence angle (b) *TE* polarization, (c) *TM* polarization.

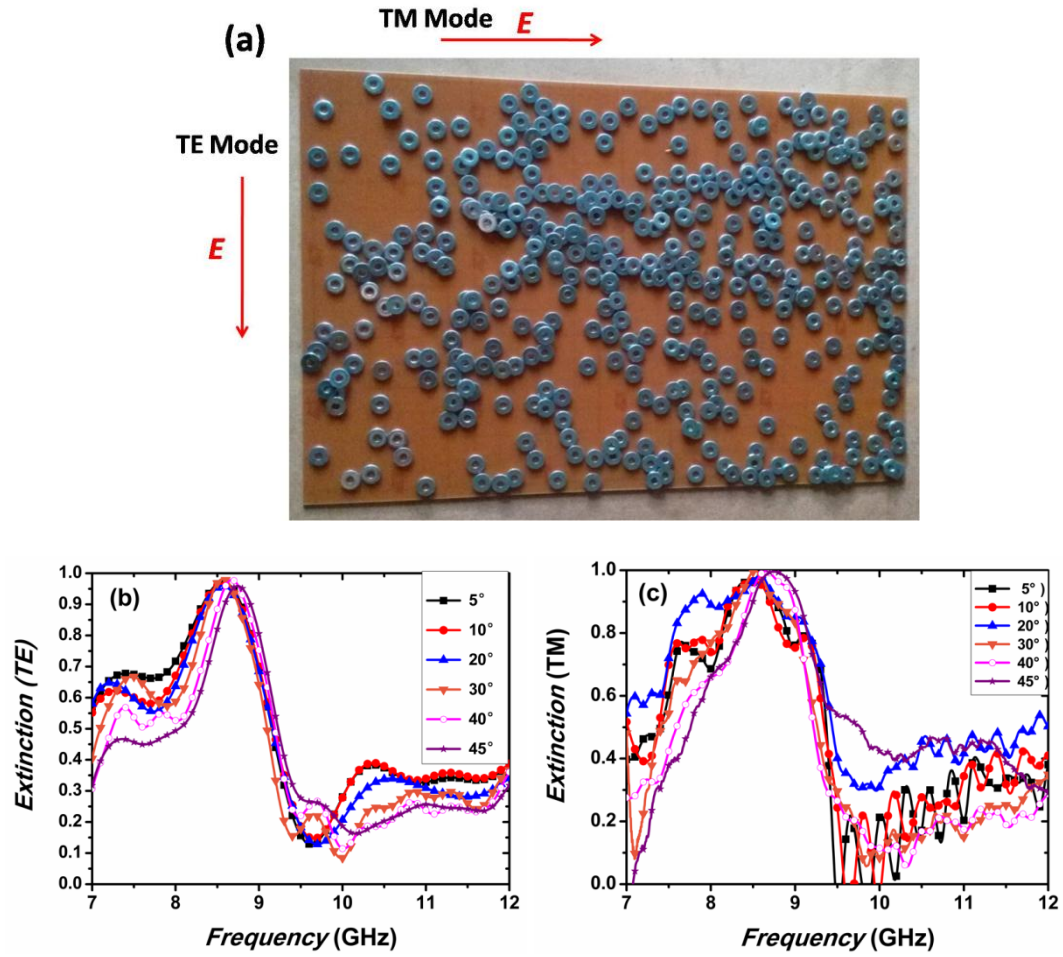

Fig. 3.3.15 (a) Photograph of the tested structure, Extinction spectra measured for a random structure

including 400 rings in a 21 x 29.7 cm^2 grounded substrate as a function of the incidence angle (b) *TE* polarization, (c) *TM* polarization.

The extinction spectra displayed from Fig. 3.3.12 to Fig. 3.3.15 show that the wave extinction are relatively insensitive to the incidence angle both for *TE* and *TM* polarization at least up to 45 °. The same conclusion holds with respect to the influence various filling factors.

The peak extinction frequency and a magnitude larger than 80 % are both preserved for the four situations, which is a signature of the magnetic resonance phenomenon. In addition the extinction band is substantially broadened as the number of rings increases.

The response of the structure can be understood as the situation described numerically from chapter 3.3.1. The broadening effect is the consequence of the coupling effects between nearby resonators. The highly disordered array gives rise to numerous extended modes contributing to the extinction spectra. The array is dense enough to avoid the multi-peak responses such as the one reported in Fig. 3.3.1 (a). However, this disordered array is sufficiently diluted to steer clear of a strong contribution of cluster modes such as the one described in chapter 3.3.1. As a consequence, the extinction spectra remain centered on the 9 GHz peak.

When the density of rings is doubled (see Fig. 3.3.15), extinction peak larger than 95 % can be preserved up to an incidence angle of 45 °. In addition, an extinction bump averaged at 55 % is occurring around 7.3 GHz. As previously described, this is the consequence of clusters development as clearly evidenced in Fig. 3.3.15 (a). Such clusters introduce longer electric length resonating modes such as the one depicted in Fig. 3.3.1 (b) with a resonance frequency centered at 7.3 GHz.

3.4 Conclusion

In this chapter, we focused on a new way for broadening the absorption window

of metamaterial-based absorbers by extending the magnetic resonance modes in *disordered* metamaterials. The key conclusions can be drawn as follows: firstly, magnetic response in periodic steel rings arrays were studied which is the fundamental behavior theory for the perfect absorption at a specific frequency. Secondly, coupling effects between nearby resonators and clustering effects in case of electric interconnections were pointed out in disordered rings structures. Following this rule, disordered broadband absorbers were proposed. Thirdly, some parameters such as filling factor, polarization and oblique incidence were investigated both numerically and experimentally. Finally, it can be concluded that disordered metamaterial absorbers can exhibit 4 times enhancement of their half-maximum bandwidth when compared to the periodic one.

References

[1] J. B. Pendry, A. J. Holden, D. J. Robbins and W. J. Stewart, Magnetism from conductors and enhanced nonlinear phenomena, IEEE Trans. Microw. Theory Tech., Vol. 47, 2075, 1999.

[2] D. R. Smith, S. Schultz, P. Markos and C. M. Soukoulis, Determination of effective permittivity and permeability of metamaterials from reflection and transmission coefficients, Phys. Rev. B, Vol. 65, 195104, 2002.

[3] R. A. Shelby, D. R. Smith and S. Schultz, Experimental veri Pcation of a negative index of refraction, Science, Vol. 292, 77-79, 2001.

[4] A. F. Koenderink and W. L. Vos, Optical properties of real photonic crystals: anomalous diffuse transmission, J. Opt. Soc. Am., Vol. B22, 1075-1084, 2005.

[5] X. Zhou, X. P. Zhao and Y. Liu, Disorder effects of left-handed metamaterials with unitary dendritic structure cell, Opt. Express, Vol.16, 7674-7679, 2008.

[6] R. Singh, X. Lu, J. Gu, Z. Tian and W. Zhang, Random terahertz metamaterials, J. Opt., Vol.12, 015101, 2010.

[7] N. Papasimakis, V. A. Fedotov, Y. H. Fu, D. P. Tsai and N. I. Zheludev, Coherent and incoherent metamaterials and order-disorder transitions, Phys. Rev. B, Vol. 80, 041102, 2009.

[8] S. Savo, N. Papasimakis and N. I. Zheludev, Localization of electromagnetic fields in disordered metamaterials, Phys. Rev. B, Vol. 85, 121104, 2012.

[9] M. Albooyeh, D. Morits and S. A. Tretyakov, Effective electric and magnetic properties of metasurfaces in transition from crystalline to amorphous state, Phys. Rev. B, Vol. 85, 205110, 2012.

[10] C. Helgert, C. Rockstuhl, C. Etrich, C. Menzel, E. B. Kley, A. Tunnermann, F. Lederer and T. Pertsch, Effective properties of amorphous metamaterials, Phys. Rev. B, Vol.79, 233107, 2009.

[11] M. Albooyeh, S. Kruk, C. Menzel, C. Helgert, M. Kroll, A. Krysinski, M.Decker, D. N. Neshev, T. Pertsch, C. Etrich, C. Rockstuhl, S. A. Tretyakov, C. R. Simovski and Y. S. Kivshar, Resonant metasurfaces at oblique incidence: interplay of order and disorder, Sci. Rep., Vol. 4, 4484, 2014.

[12] J. Gollub, T. Hand, S. Sajuyigbe, S. Mendonca, S. Cummer and D. R. Smith, Characterizing the effects of disorder in metamaterial structures, Appl. Phys. Lett., Vol. 91, 162907, 2007.

[13] H. Chen, L. Huang, X. Cheng, and H. Wang, Magnetic properties of metamaterials composed of closed rings, Prog. Electromagn. Res., Vol. 115, 317-326, 2011.

[14] A. A. Fernandez-Marın, J. A. Mendez-Bermudez, J. Carbonell, F. Cervera, J. Sanchez-Dehesa and V. A. Gopar, Beyond Anderson Localization in 1D: Anomalous Localization of Microwaves in Random Waveguides, Phys. Rev. Lett., Vol. 113, 233901, 2014.

[15] A. Moreau, C. Ciracı, J. J. Mock, R. T. Hill, Q. Wang, B. J. Wiley, A. Chilkoti and D. R. Smith, Controlled-reflectance surfaces with film-coupled colloidal

nanoantennas, Nature, Vol. 492, 86-89, 2012.

[16] Y. Nishijima, L. Rosa and S. Juodkazis, Surface plasmon resonances in periodic and random patterns of gold nano-disks for broadband light harvesting, Opt. Express, Vol. 20, 11466-11477, 2012.

[17] X. Chen, H. Gong,.S. Dai, D. Zhao,Y. Yang, Q. Li and M. Qiu, Near-infrared broadband absorber with film-coupled multilayer nanorods, Opt. Lett., Vol. 38, 2247-2249, 2013.

[18] J. Hao, É. Lheurette, L. Burgnies, É. Okada and D. Lippens, Bandwidth enhancement in disordered metamaterial absorbers, Appl. Phys. Lett., Vol. 105, 081102, 2014.

[19] J. Hao, R. Niemiec, L. Burgnies, É. Lheurette, and D. Lippens, Broadband absorption through extended resonance modes in random metamaterials, J. Appl. Phys., Vol. 119, 193104, 2016.

[20] S. Cao, T. Wang, J. Zhao, F. Tan, X. Zhang and W. Yu, Hierarchic random nanosphere model for broadband solar energy absorbers, Opt. Mater. Express, Vol. 5, 2777-2785, 2015.

[21] M. Nazirzadeh, F. Atar, B. Turgut and A. Okyay, Random sized plasmonic nanoantennas on Silicon for low-cost broad-band near-infrared photodetection, Sci. Rep., Vol. 10.1038, 2014.

[22] K. Y. Bliokh, Y. P. Bliokh, V. Freilikher, S. Savel'ev and F. Nori, Colloquium: Unusual resonators: Plasmonics, metamaterials, and random media, Rev. Mod. Phys., Vol. 80, 1201, 2008.

[23] A. Hessel and A. A. Oliner, A new theory of wood's anomalies on optical gratings, Appl. Opt., Vol. 4, 1275-1297, 1965.

[24] J. Hao, L. Zhou and M. Qiu, Nearly total absorption of light and heat generation by

plasmonic metamaterials, Phys. Rev. B, Vol. 83, 165107, 2011.

Chapter 4 Bandwidth enhancement of flexible multi-size resonator arrays at millimeter waves

4.1 Introduction

Perfect Metamaterial Absorbers (PMA) have attracted significant interest due to their numerous potential applications in various fields such as sensing [1-4], photo-detection [5], electromagnetic compatibility [6], stealth and energy harvesting [7-8]. It is well known that, all of these applications need the absorbing materials with very low thickness or even flexible and high performance in terms of absorption coefficient, bandwidth, while being insensitive to polarization and angle of incidence. Among these performances, let us remind we pay special attention on the bandwidth issue, which means that we try to design broadband PMAs. Generally, this broadband objective can be realized by increasing the number of resonators with size variation either in transverse or longitudinal directions. In this chapter, we propose a bandwidth enhancement of PMA through varying the transverse dimension of elementary resonators.

As well known, the first experimental demonstration of periodic PMA that used a planar electrical ring resonator coupled via a thin dielectric layer to a metal strip, as a basic cell, was published by Landy et al. in 2008 [9]. This structure consists of two metallic layers, one ground plane and an array of electric ring resonator (ERR) of various shape separated by a dielectric layer. The ERR array on the top of the dielectric layer couples strongly to the uniform electric field of the incidence wave, but weakly to magnetic field, providing frequency dependent electric response $\varepsilon(\omega)$. The magnetic field of incident waves will penetrate the space between the ERR and back metallic ground plane, leading to a frequency dependent magnetic response $\mu(\omega)$. One can tune the effective $\varepsilon(\omega)$ and $\mu(\omega)$ by adjusting the dimensions of the ERR, back ground plane

and the space gap between them, thus achieving the perfect impedance matching between the absorber and free space and minimize the reflection near to zero. Simultaneously, large loss and transmission near to zero can be achieved by varying the imaginary part of the material permittivity. The resulting absorption A, is calculated $A(\omega) = 1 - R(\omega) - T(\omega)$, where $R(\omega)$ is the reflection and $T(\omega)$ is the transmission of the incident wave, approximately equal to zero.

Based on the three layers PMA principle, let us now consider how to propose a broadband plane PMA. By the combination of ELCs (electrically coupled LC resonator) and SRRs (split ring resonators) a broadband gigahertz region MPMA has been described in the paper published by S. Gu [10]. Distinct circular patches with various radius, width of lumped element, hexagonal metal dendritic, multiplexed cross, lengths of conductive and loss cut-wires in plane can be added to propose an ultra-thin broadband PMA [11-27]. Another kind of design is to use metal stripes and trapezoid arrays that are periodically arranged on the dielectric layer [28-31]. In addition, there have been some efforts by using resistance frequency selective surface (FSS) structures to propose thin broadband absorber [32-33].

In this chapter, we first show numerically how a four-fold improvement of the bandwidth of a plasmonic-like flexible absorber can be achieved at millimeter waves with operation at W frequency band (75 - 110 GHz). Then an absorber prototype was subsequently fabricated in a coplanar configuration by ink-jet printing technology. Moreover, a flexible 100 μm-thick grounded dielectric layer, was chosen as the substrate, providing the absorber a significant potential to cover an object of arbitrary shape. Finally, an experimental verification of the broad band property of absorbers was performed under free space condition. Indeed, a quasi-optic setup based on vector network analyzer (Rohde & Schwarz ZVA 24) operating in the W-band (75 - 110 GHz) was used.

4.2 Bandwidth enhancement of flexible multi-size resonator arrays at millimeter waves

4.2.1 Design of the structure and simulation analysis

Fig.4.1 (a) shows a schematic of super-cells periodically arrayed with a square lattice constant (P = 2800 μm) while Fig.4.1 (b) displays the top view of a basic super-cell. The latter consists of four square-shaped resonators with the corresponding side lengths labeled d_1 = 1000 μm, d_2 = 945 μm, d_3 = 890 μm and d_4 = 850 μm and which were optimized by the design procedure outlined below. Each resonator is realized by means of three layers which are (i) a top silver patch (ii) a thin dielectric layer and (iii) an aluminum back-ground plate as illustrated in Fig.4.1 (c). All the patches are centered in each sub-cell. As a consequence the slots between two adjacent pads are S_1 = 427.5 μm, S_2 = 502.5 μm, S_3 = 455 μm, S_4 = 530 μm, respectively, whereas the thickness are for aluminum: $t_{Al} \sim 10$ μm, PET: t_{PET} = 100 μm and for silver: t_{Ag} = 1 μm. The relative permittivity of the PET dielectric layer is ε_r = 2.9 and dielectric loss tangent tanδ = 0.025. Conductivity of silver was assumed for these calculations $\sigma = 5\times10^6$ S/m. and hence one order of magnitude lower than the corresponding bulk silver conductivity reported in the literature (6.3×10^7 S/m at room temperature). The finite element based electromagnetic solver HFSS by ANSYS was used for calculating the scattering parameters (*Sij*) under normal and oblique incidences. Indeed the study under tilted incidence provides first pieces of information when the absorber is bent owing to the flexible substrate. For these calculations periodicity was mimicked by means of master-slave boundary conditions while electromagnetic plane wave excitation was supplied by means of a Floquet port. In addition a Perfect Electrical Conductor (PEC) was added at the bottom boundary of the simulation domain to describe the electromagnetic behavior of the thick aluminum ground plane.

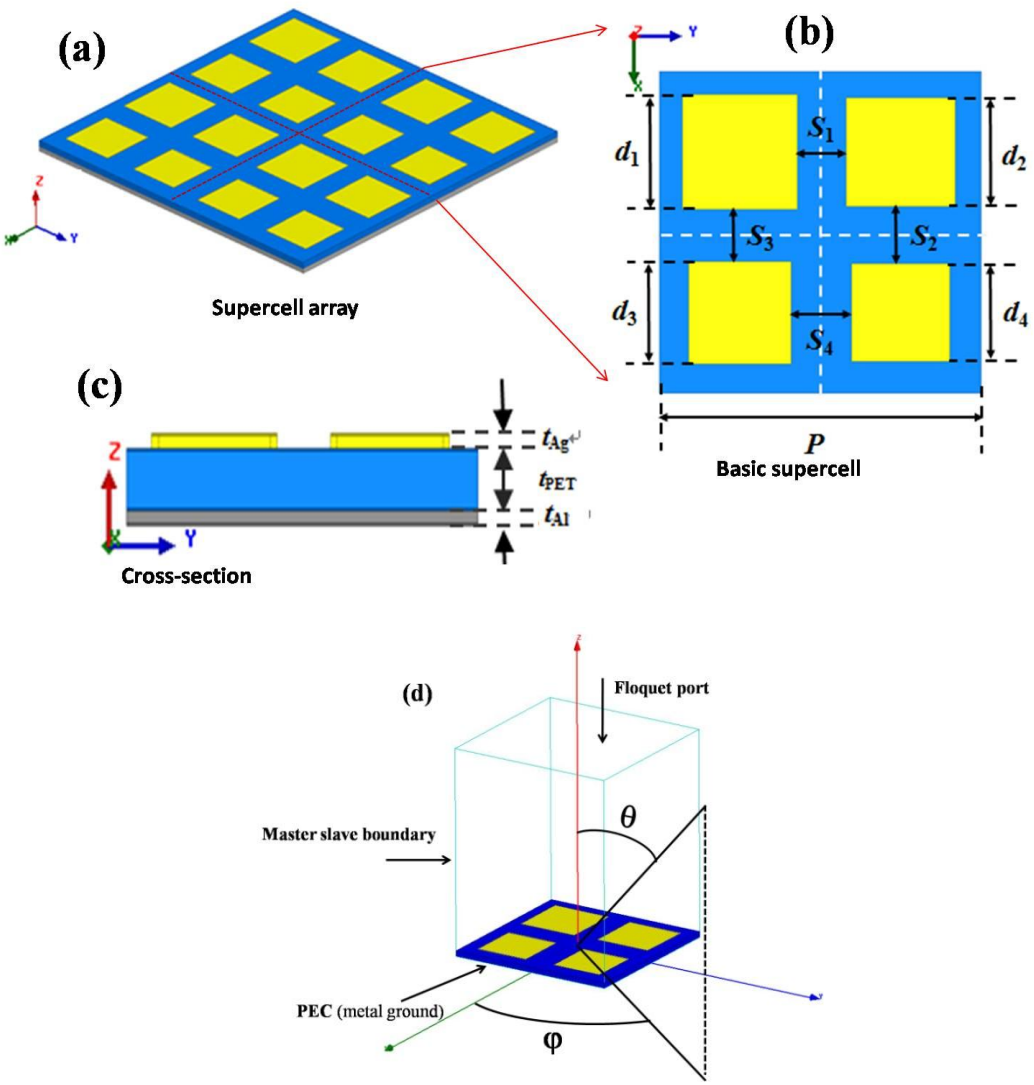

Fig.4.1 (a) 3D schematic of the super-cell square-lattice array with square-shaped metal/dielectric metal resonator (b) top view of the super-cell, (c) cross section of the three layered metal pattern /dielectric spacer layer/ ground metal plate, (d) the super-cell with its characteristic parameters and the simulation conditions.

The absorbance (A) was calculated as $A = 1 - R - T = 1 - |S_{11}|^2 - |S_{21}|^2$, where R and T are the reflectance and transmittance related to the square magnitude of the complex scattering parameters S_{11} and S_{21} calculated numerically. In the present case $S_{21} = 0$ whatever the frequency of interest due to the metal shield of the ground plane. From the above equation it is worth mentioning that a unit absorbance can be achieved providing a perfect impedance matching with free space ($Z_0 = 377\ \Omega$) is

satisfied. As a consequence, the key issue is the successful broadband matching of the impedance as further discussed in the equivalent circuit approach. The simulated reflection (*R*) and absorption (A) coefficients versus frequency between 65 and 105 GHz were calculated by full wave analysis.

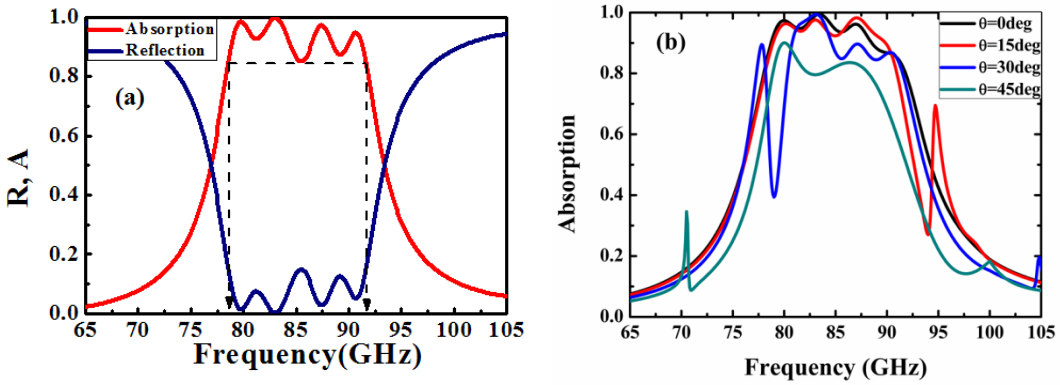

Fig.4.2 Absorbance spectrum (red line) determined from the scattering parameter S_{11} (blue line) calculated by full wave analysis (a), illustration of the influence of the incidence angle (θ) (b).

Fig.4.2 (a) shows the absorption and reflection curves with respect to the frequency. A strong absorption in excess of 85 % from 78.5 GHz to 91.7 GHz can be evidenced as the consequence of the overlap of four reflection dips and concomitant absorption peaks at 79.8 GHz, 83.4 GHz, 87.0 GHz and 90.7 GHz (with absorbance of 97.3 %, 99.5 %, 96.1 % and 86.9 %, respectively) which can be attributed to the four different resonators in the super-cell.

Fig.4.2 (b) compares the spectra calculated for various incidence angles (θ) ranging from θ = 0° to θ = 45 °. For this study of the sensitivity to the incidence direction, the angle ϕ (projection on the x-y plane according to the inset in Fig.4.1 (d) was set to ϕ = 0. Indeed, it can be shown that the sensitivity of *A* to ϕ is relatively weak owing to symmetry properties of the square-shaped resonance pattern. It appears that the asymmetry introduced by the super-cell configuration can be neglected. From Fig.4.2 (b) it can be noticed that a high absorbance in a broadband window is preserved at least up to θ = 30°.

To have a clear understanding of the absorbing mechanism, the surface current distribution was given in Fig.4.3 (a). The mapping of the surface current distribution at the four absorption peaks indicates that the surface currents flow in anti-parallel directions between the top and bottom metal layers. They thus form a current loop at the origin of a magnetic activity. An in-plane magnetic dipole is induced resulting from the wrapping around the magnetic field orientation of conduction current components in the metal films and displacement contribution through the dielectric layer. For a deeper understanding of the scattering of the impinging wave with a frequency selective trapping of the electromagnetic energy, Fig.4.3 (b) shows the Poynting vector map in the *x-y* plane at the middle of the dielectric layer at f_2 and f_3. Typical vortex-like patterns can be noticed with a selective spatial localization of the energy despite the fact that the device is uniformly illuminated by a plane wave. As for pyramidal-shaped stacked structures often referred as rainbow trapping devices in optics (see chapter 5) the wave is selectively trapped and hence subsequently absorbed according to the fit of the transverse dimensions to the incident wavelength. Also of prime importance is the fact that the energy stored in other (dark) resonators appears negligible with respect to the bright one. Therefore it can be assumed that the coupling mechanisms between resonators are not playing the major role in the broadening. We will come back about such an assumption that permits us to apply a superimposition principle in the next section where the equivalent circuit approach is addressed.

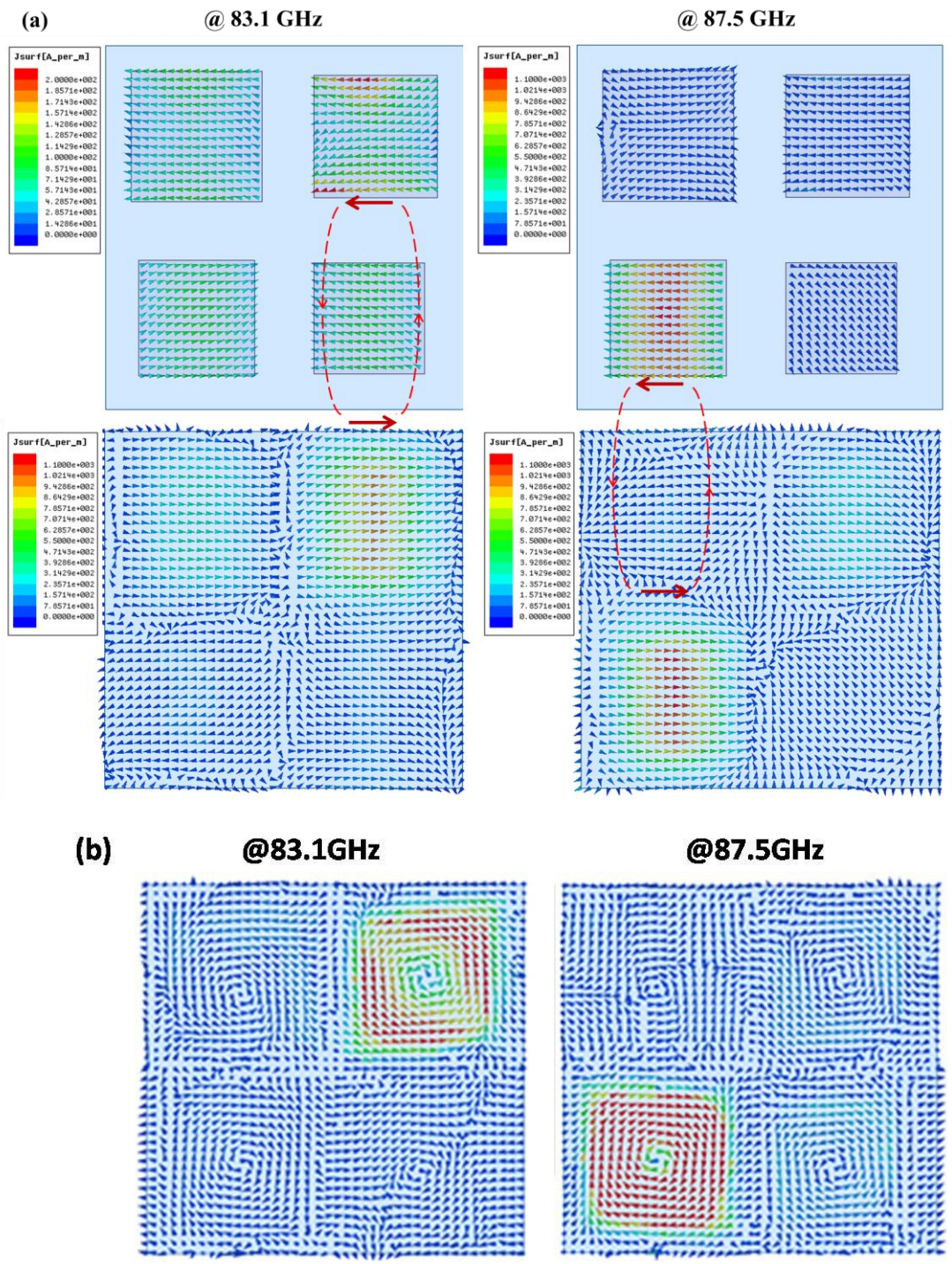

Fig.4.3 (a) The surface current distribution in the *x-y* plane on the top and bottom metal surface, (b) Poynting vector map in the *x-y* plane at the middle of the dielectric layer at f_2 (left-side) and f_3 (right-side) respectively.

4.2.2 Equivalent circuit mode analysis

We first applied TLM-based circuit approach to a single-size lumped absorber structure. The circuit approach is based on the assumption that the surface impedance (Z_{tot}) in the upper plane (air/absorber interface) of the stacked layers namely (i) silver patches (ii) dielectric and (iii) uniform aluminum plate can be modeled by considering separately the surface impedance of a frequency selective surface (Z_{FSS}) with only metal pads and the impedance of the grounded dielectric layer (Z_d) calculated in the upper plane [24-25], shown in Fig.4.4.

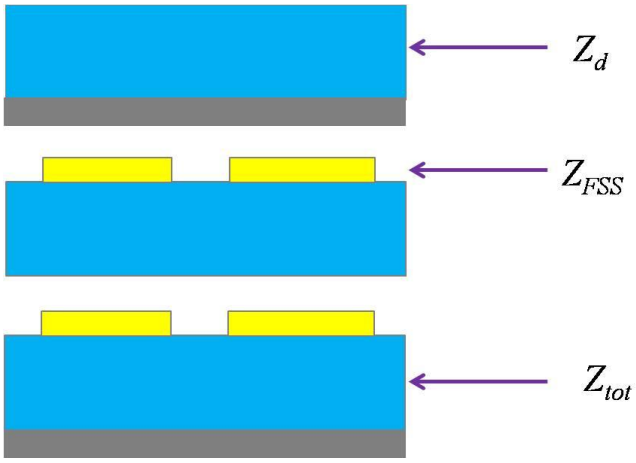

Fig.4.4 Schematic of the equivalent circuit mode.

On this basis, the surface impedance of the absorbing structure (Z_{tot}) is equal to the parallel connection of Z_{FSS} and Z_d formulated as:

$$Z_{tot} = Z_{FSS} /\!/ Z_d = Z_{FSS} \times Z_d / (Z_{FSS} + Z_d) \quad 4.1$$

$$Z_{FSS} = (1+S_{11}) / [Y_{air} - Y_{subs} - (Y_{air} + Y_{subs}) \times S_{11}] \quad 4.2$$

$$Z_d = Z_{02} \times \tanh(\gamma_{port2} \times d_{PET}) \quad 4.3$$

where, γ_{port2} is the propagation constant in the dielectric layer, $Y_{air} = 1/Z_{air}$, $Y_{subs} = 1/Z_{subs}$, induced from the full wave analysis approach. Fig.4.5 shows the schematic of the TLM-based simulation condition. Here, we set period P = 1.4 mm, side width a = 1 mm, permittivity of PET: $\varepsilon_r = 2.9\ (1+0.025i)$ and conductivity of silver: $\sigma = 4 \times 10^6$

S/m.

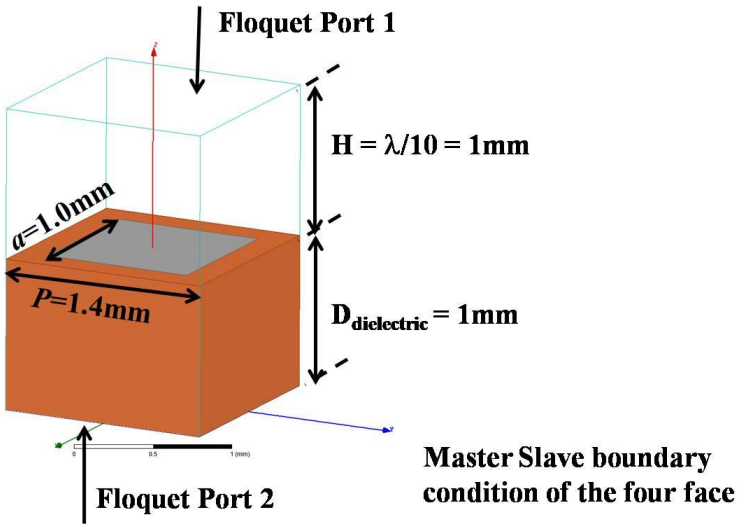

Fig.4.5 Schematic of the TLM-based simulation condition

The frequency dependence of the real and imaginary part of Z_{FSS}, Z_d and Z_{tot} displayed in Fig.4. 6.

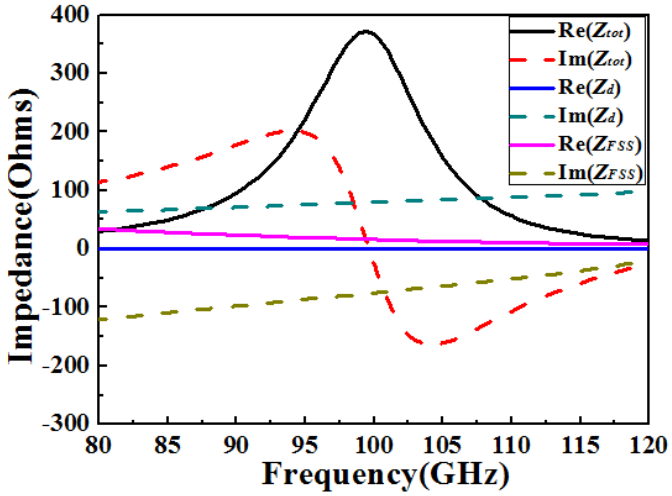

Fig.4. 6 Frequency dependence of the complex impedances Z_{FSS}, Z_d and Z_{tot}.

It can be noticed that the inductive part of Z_d varies linearly against the angular frequency ω in agreement with the results plotted in green dashed lines, while the real part Z_d is kept constant around zero plotted in blue solid lines. As the frequency increases, the real part of frequency selective surface Re(Z_{FSS}) is decreased to zero

until around 130 GHz. Below the resonance frequency of the FSS it can be noticed that Z_{FSS} is capacitive. At resonance frequency around 100 GHz the imaginary part of $Z_{tot} = \mathrm{Im}(Z_d) + \mathrm{Im}(Z_{FSS}) = 0$ is achieved with concomitantly a peak in the real part $\mathrm{Re}(Z_{tot}) \approx 377\ \Omega$ close to the free space impedance. Since impedance matching to the free space is achieved, the reflection decrease to zero and the unit absorption is achieved.

The same analysis can be applied for each of the four resonating elements of the super-cell. The fact to slightly increase the slot width as a consequence of the shrinking in the metal patch dimension, by keeping constant the super-cell lattice, modifies the resonance frequency which increases via the decrease of the capacitance (C). Fig.4.7 shows the total impedance of the four parts separately while in Fig.4. 8 was plot the total impedance for the association of multi-size resonators which is directly deduced from the full wave analysis.

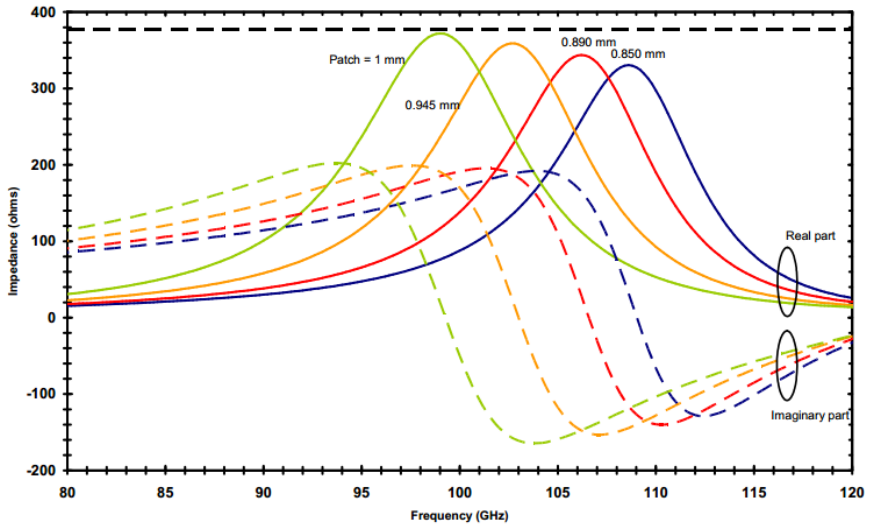

Fig.4.7 Total impedance of the four different size parts as d_i = 1 mm, 0.945 mm, 0.890 mm and 0.850 mm.

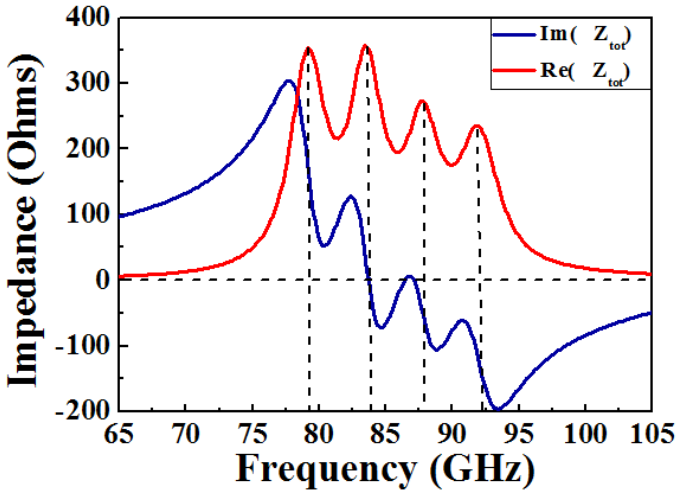

Fig.4. 8 Variation of the total complex impedance of the super-cell array.

By comparing the results of these approaches (TLM versus full wave) one can note that the trends in the frequency dependence of the total surface impedance are similar. In particular perfect matching is achieved around the central frequency with cancellation of the imaginary part and a real value close the free space impedance. Quantitatively however there is a blue shift of the resonance frequency for the FSS analysis method.

It is believed that this discrepancy stems from the fact that in the Transmission line method we neglect the influence of the ground plane for determining the frequency response of the FSS. In practice however the slot dimension between the FSS patches and the thickness of the dielectric layer are comparable. Under this condition one can expect some difference in the resonance frequency owing to the influence of the ground plane taken into account in a full wave analysis while it does not impact the frequency response of the FSS in a transmission line approach

4.2.3 Fabrication

The absorbance devices were fabricated by using ink-jet printing technology (Ceraprinter X-series of Ceradrop with a printing head Spectra128 of Dimatrix) and a polyethylene terephthalate (PET) dielectric substrate (Goodfellow corporation) which

was pre-metalized by the supplier with an aluminum layer. A 109 µm- thickness of the grounded substrate was measured with a Mitutoyo thickness gauge. Suntronic Ink: Solsys Jettable Silver *EMD5714* that contains 40 wt % silver nanoparticles was used for ink jet printing with a pulse voltage of 58 V and a jetting frequency of 1500 Hz. Subsequently sintering of samples during 40 minutes at 150 ℃ was performed to achieve acceptable conductivity of the printed patterns. A photograph of a 30 x 30 mm^2 absorber with 10 super-cells in the transverse directions is shown in Fig.4.9 (a). The device has been fixed onto a 2-inch semiconductor holder. The flexibility property, that constitutes one of the originality of the present work, can be checked by intentionally bending the device (Fig.4.9 (b)). Also, Fig.4.9 (c) gives the optical photograph of the four silver lumps after ink-jet printing.

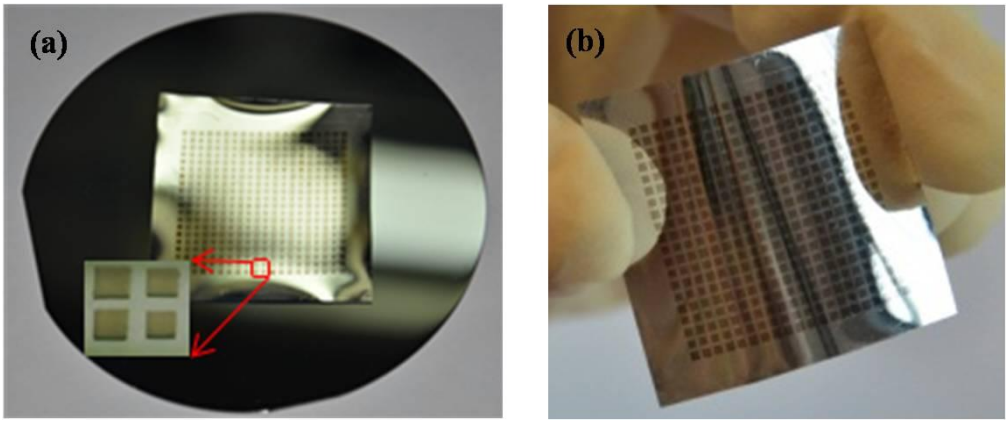

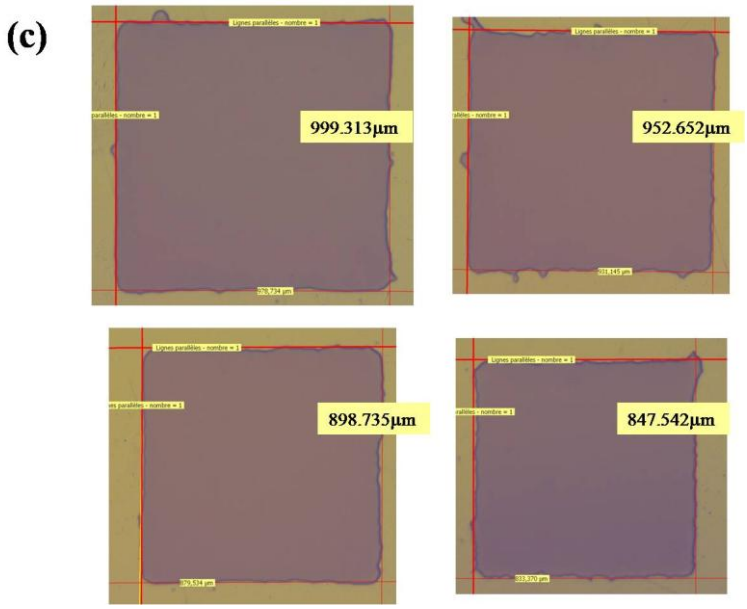

Fig.4.9 (a) Photograph of the absorbing device fabricated with a 30 × 30 mm^2 area. (b) Illustration of the flexibility of the sample, (c) optical photograph of the four silver lumps on top view.

4.2.4 Experimental verification in free space

As illustrated in Fig.4.9, a super-cell array was periodically printed on the PET substrate to form a 30×30 mm^2 absorber structure. In order to experimentally verify the broad band property of absorption, the scattering parameters (S_{ij}) were measured under free space condition. The photograph of the measurement equipment was depicted in Fig.4.10. Indeed, a quasi-optic setup based on vector network analyzer (Rohde & Schwarz ZVA 24) operating in the W-band (75 - 110 GHz) was used. This setup has been first calibrated in waveguide using a standard TRM (Thru, Reflect, Match) method. Then, the incident beam was radiated in free space by circular corrugated horns, as depicted in Fig.4.10. In order to create a collimated beam to probe the sample (normal incidence of electromagnetic field), we used a dielectric lens apparent in Fig.4.10. Verification of the collimation was performed via transmission experiment without any device with a similar lens/horn configuration.

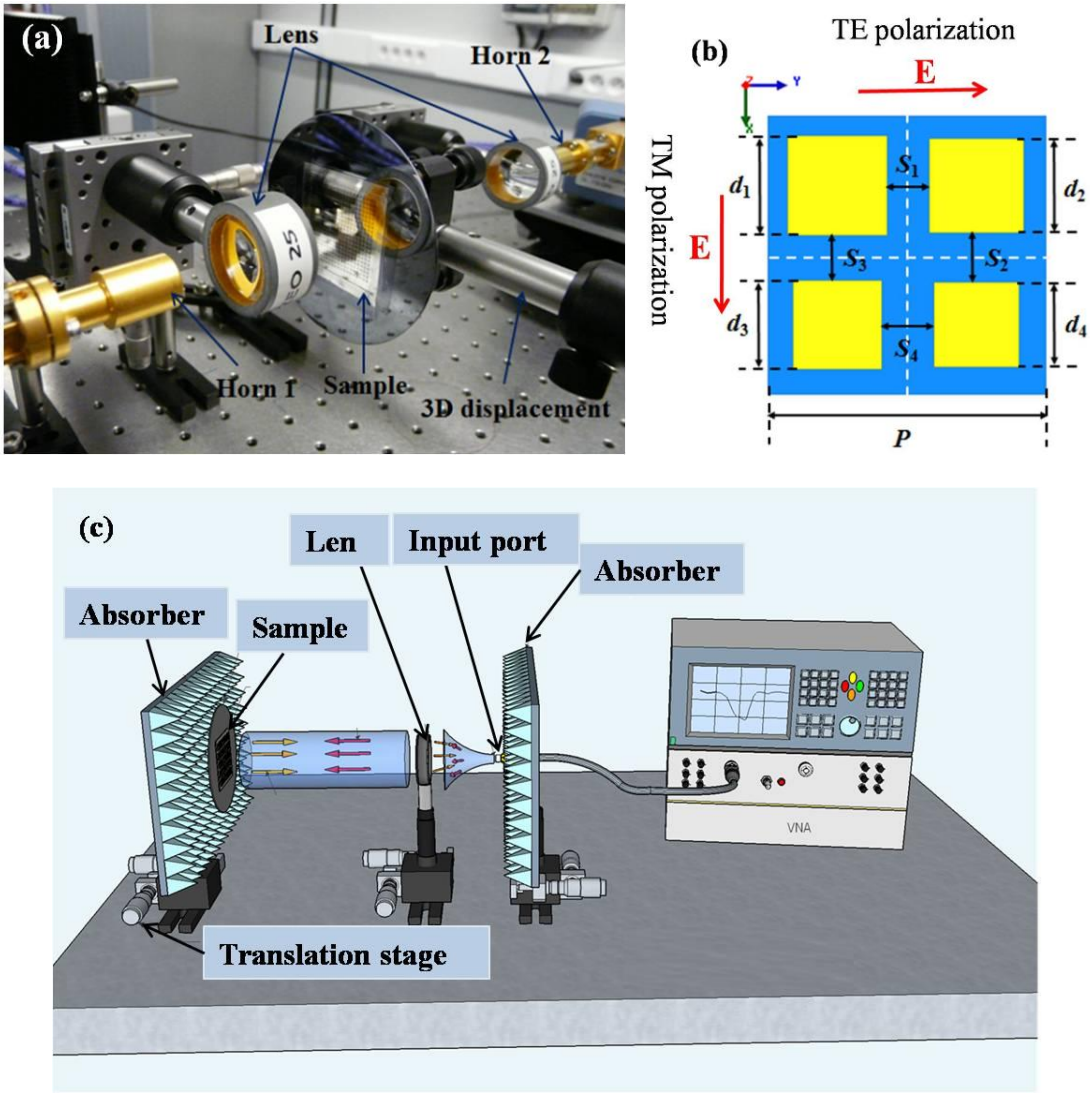

Fig.4.10 (a) Close view of the free-space set up used for the vector network analysis in the 75-110 GHz W-band, (b) illustration of the *TE* and *TM* polarization in the measurement, (c) schematic diagram of the free-space set up .

In the measurement procedure, for every test we measured 101 different positions of sample which varies along the *z* coordinate, then averaged the 101 different absorptions. Two polarizations were tested namely *TE* and *TM* polarization as defined in Fig.4.10 (b).

For the first stage, we measured the absorption under normal incidence. One of the key issue for free space reflection parameters measurement is to proper compare the sample with an appropriate reference. So firstly, we tested the S_{11} of the reference

plane. Here, we chose perfect reflection mirror or the PET substrate with Aluminum metallic ground as a reference. Secondly, we put the absorber sample in the same place as the reference and test the S_{ij} parameters. Finally, we subtracted the two measurement results. A series of absorption spectra were shown in Fig.4.11.

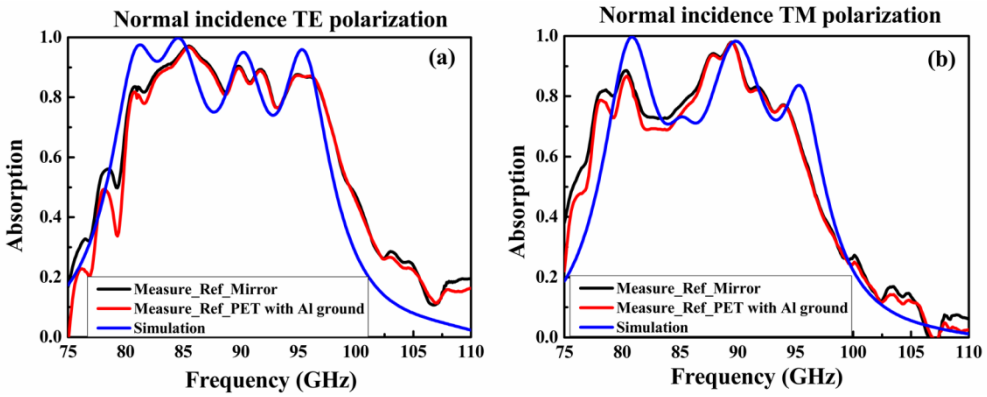

Fig.4.11 Experimental (blank line Mirror as reference, red line PET substrate with Al metallic ground as reference) and simulation (blue line) absorption spectra under normal incidence, (a) *TE* polarization, (b) *TM* polarization.

Comparing the black and red spectra both for *TE* and *TM* polarization, it can be noted that for the two different references, we obtain exactly the same absorption, which confirms that the aluminum metallic ground fully stops the transmitted wave. Furthermore, this shows an overall good agreement between experiment and simulation results despite the slightly broader absorption window which can be explained by fabrication tolerance.

For the second stage, reflection measurements under oblique incidence were carried out. The measurement method detailed below was used as normal incidence, and the photograph of the setup is shown in Fig.4.12. Let us remind that two horns were used: one for launching the energy and the other for receiving the reflection energy. Absorbers were used around the two horns in order to avoid any interference.

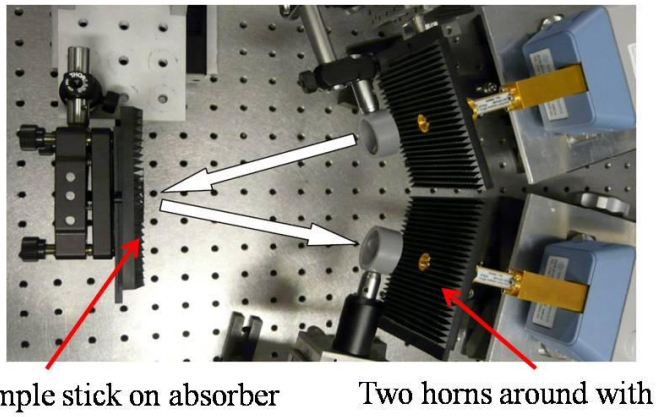

Fig.4.12 Photograph of the free-space set up of vector network analysis in the 75-110 GHz band used for the oblique incidence measurement.

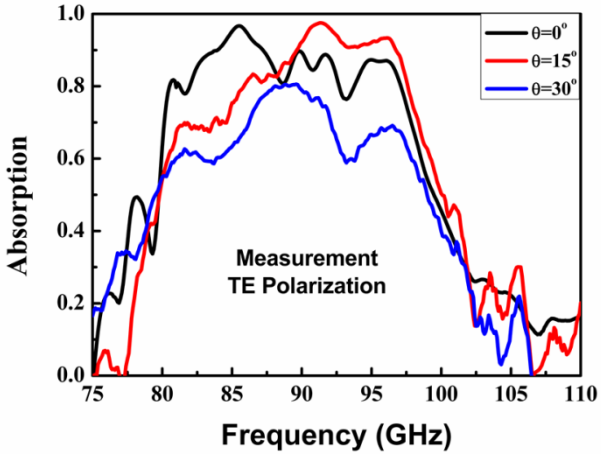

Fig.4.13 Experimental absorption spectra under obilque incidence θ vared from 0° to 30° of *TE* polarization.

As shown in Fig.4.13, the absorption is quite sensitive to the incidence angle since the maximum of absorbance around 90% for normal or low incidence angle (15 °) drops around 70 % for an incidence angle of 30 °. It is believed that these relatively poor performances in terms of sensitivity to the incidence angle are results of the multi-size pattern.

4.3 Conclusion

In summary, we demonstrated experimentally the possibility of fabricating a deep sub-wavelength (thickness ~ $\lambda_0/35$) absorber covering around 60 % of the

W-band (75 - 110 GHz) with mean absorbance values around 90 %. In addition, the devices were fabricated onto a flexible substrate by ink-jet printing technology paving the way for the realization of ultra-thin broad-band conformable large area absorbers operating at millimeter waves.

References

[1] H. Tao, E. Kadlec, A. Strikwerda, K. Fan, Willie J. Padilla, R. Averitt, E. Shaner and X. Zhang, Microwave and Terahertz wave sensing with metamaterials, Opt. Express, Vol.19, 21620-21626, 2011.

[2] F. Alves, D. Grbovic, B. Kearney, Nickolay V. Lavrik and G. Karunasiri, Bi-material terahertz sensors using metamaterial structures, Opt. Express, Vol. 21, 13256132571, 2013.

[3] N. Liu, M. Mesch, T. Weiss, M. Hentschel, and H. Giessen, Infrared perfect absorber and its application as plasmonic sensor, Nano Lett. Vol. 10, 2342-2348, 2010.

[4] B. Kearney, F. Alves, D. Grbovic and G. Karunasiri, Al/SiOx/Al single and multiband metamaterial absorbers for terahertz sensor applications, Opt. Eng., Vol.52, 013801, 2013.

[5] J. Rosenberg, R. V. Shenoi, T.E. Vandervelde, S. Krishna and O. painter, A multispectral and polarization-selective surface-plasmon resonant midinfrared detector , Appl. Phys. Lett., Vol. 95, 161101, 2009.

[6] R. Huang, Z. Li, L. Kong, L. Liu and S. Matitsine, Analysis and design of an ultra-thin metamaterial absorber, Prog. Electromagn. Res. B, Vol. 14, 407-429, 2009.

[7] J-J. Greffet, R. Carminati, K. Joulain, J.-P. Mulet, S. Mainguy and Y. Chen, Coherent emission of light by thermal sources, Nature, Vol. 416, 61-64, 2002.

[8] J. Chou, Y. Yeng, A. Lenert, V. Rinnerbauer, I. Celanovic, M. Soljačić, E. Wang and S-G. Kim, Design of wide-angle selective absorbers/emitters with dielectric filled metallic photonic crystals for energy applications, Opt. Express, Vol. 22, A144-A154, 2013.

[9] N. Landy, S. Sajuyigbe, J. Mock, D. Smith and W. Padilla, Perfect metamaterial absorber, Phys. Rev. Lett., Vol. 100, 207402, 2008.

[10] S. Gu, J. Barrett, TH. Hand, B. Popa and S. Cummer, A broadband low-reflection metamaterial absorber, J. Appl. Phys., Vol. 108, 064913,2010.

[11] Y. Liu, S. Gu, C. Luo and X. Zhao, Ultra-thin broadband metamaterial absorber, Appl. Phys. A., Vol. 108, 19-24, 2012.

[12] H. Wakatsuchi, S. Greedy, C. Christopoulos and J. Paul, Customised broadband metamaterial absorbers for arbitrary polarisation, Opt. Express, Vol. 18, 22187-22198, 2010.

[13] S. Chen, H. Cheng, H. Yang, J. Li, X. Duan, C.i Gu and J. Tian, Polarization insensitive and omnidirectional broadband near perfect planar metamaterial absorber in the near infrared regime, Appl. Phys. Lett., Vol.99, 253104, 2011.

[14] C. Cheng, M. Abbas, C. Chiu, K. Lai, M. Shih and Y. Chang, Wide-angle polarization independent infrared broadband absorbers based on metallic multisized disk arrays, Opt. Express, Vol. 20, 10376-10381, 2012.

[15] Y.Cheng, Y. Wang, Y. Nie, R. Gong, X. Xiong and X. Wang, Design, fabrication and measurement of a broadband polarization-insensitive metamaterial absorber based on lumped elements, J. Appl. Phys., Vol. 111, 044902, 2012.

[16] M. Pu, M. Wang, C. Hu, C. Huang, Z. Zhao, Y. Wang and X. Luo, Engineering heavily doped silicon for broadband absorber in the terahertz regime, Opt. Express, Vol. 20, 25513-25519, 2012.

[17] S. Gu, B. Su and X. Zhao, Planar isotropic broadband metamaterial absorber, J. Appl. Phys., Vol.114, 163702, 2013.

[18] W. Ma, Y. Wen and X. Yu, Broadband metamaterial absorber at mid-infrared using multiplexed cross resonators, Opt. Express, Vol. 21, 30724-30730, 2013.

[19] Yongzhi Cheng, Yan Nie, Rongzhou Gong, A polarization-insensitive and omnidirectional broadband terahertz metamaterial absorber based on coplanar multi-squares films, Opt. Laser Technol., Vol. 48, 415-421, 2013.

[20] F. Zhang, L. Yang, Y. Jin and S. He, Turn a highly reflective metal into an omnidirectional broadband absorber coating a purely-dielectric thin layer of grating, PIER, Vol. 134, 95-109, 2013.

[21] B. Wang, L. Wang, G. Wang, W. Huang, X. Zhai and X. Li, Tunable bandwidth of the terahertz metamaterial absorber, Opt. Commun., Vol. 325, 78-83, 2014.

[22] T. Jang, H. Youn, Y. Shin and L. Guo, Transparent and Flexible Polarization-Independent Microwave Broadband Absorber, ACS Photonics, Vol. 1, 279-284, 2014.

[23] H. Shi, J. Li, A. Zhang, J. Wang and Z. Xu, Broadband cross polarization converter using plasmon hybridizations in a ring/disk cavity, Opt. Express, Vol. 22, 20973-20981, 2014.

[24] T. Nguyen, S. Bui, T. Nguyen, T. Nguyen, Y. Lee, M. Nguyen and D. Vu, Metamaterial-based perfect absorber: polarization insensitivity and broadband, Adv. Nat. Sci.: Nanosci. Nanotechnol., Vol. 5, 2043-6262, 2014.

[25] X. Liu, G. Yang, E. TAO, L. Ma and Y. Lv, A broadband polarization-insensitive metamaterial absorber based on multi-mode resonance, IEEE APCAP, 1115-1118, 2014.

[26] B. Wang, L. Wang, G. Wang, W. Huang, X.i Li and X. Zhai, A simple design of a

broadband, polarization-insensitive, and low-conductivity alloy metamaterial absorber, Appl. Phys. Express, Vol.7, 082601, 2014.

[27] C. Shi, X.i Zang, Y. Wang, L. Chen, B. Cai and Y. Zhu, A polarization-independent broadband terahertz absorber, Appl. Phys. Lett., Vol. 105, 031104, 2014.

[28] K. Aydin, V. E. Ferry, R. M. Briggs and H. A. Atwater, Broadband polarization-independent resonant light absorption using ultrathin plasmonic super absorbers, Nature Commun., Vol. 10, 1-7, 2011.

[29] D. Kim, D. Kim, S. Hwang, and J. Jang, Surface relief structures for a flexible broadband terahertz absorber, Opt. Express, Vol. 20, 16815-16822, 2012.

[30] C. Wu and G. Shvets, Design of metamaterial surfaces with broadband absorbance, Opt. Express, Vol. 37, No. 3, 308-310,2012.

[31] S. Butun and K. Aydin, Structurally tunable resonant absorption bands in ultrathin broadband plasmonic absorbers, Opt. Express, Vol. 22, 19457-19468, 2014.

[32] M. Li, S. Xiao, Y. Bai, and B. Wang, An ultrathin and broadband radar absorber using resistive FSS, IEEE Antennas Wirel. Propag. Lett., Vol. 11, 748-751, 2012.

[33] H. Zhang, P. Zhou, H. Lu, Y. Xu, D. Liang and L. Deng, Resistance Selection of High Impedance Surface Absorbers for Perfect and Broadband Absorption, IEEE Trans. Antennas Propag., Vol. 61, 976-979, 2013

Chapter 5 Stacked Plasmonic resonator based millimeter wave absorber

5.1 Introduction

Recently, the applications in the millimeter wave band, high radio frequency band ranging from 30 to 300 GHz, are experiencing an unprecedented development not only in indoor communication at 60 GHz but in monitoring security system as well, particularly for automobile at 77 GHz and defense at 94 GHz. Nowadays, active and passive components are integrated into various systems which are developed to be more and more compact and robust. Together with high performance in terms of absorption coefficient, bandwidth, and insensitivity to polarization and angle of incidence, thin and flexible perfect absorbers are welcome and are even requisite in these systems. In this context, we addressed more particularly on the bandwidth issue to design an ultra-broadband millimeter wave metamaterial absorber by stacking multiple resonators with varying dimensions in transverse direction.

Stacking multilayered metamaterial structures is considered as a promising candidate for designing ultra-broadband absorbers. Jingbo Sun et al. proposed an extremely broadband metamaterial absorber based on destructive interference mechanism exhibited in a multilayered SRRs stack [1-2]. Their optimized structure contains four layers of dielectric substrate and three SRRs with different sizes. The four resonances yield optimal refractive index dispersion and realize a successive anti-reflection coating in a wide frequency band, while the bottom coating metallic ground plane stops all transmission wave. Finally, perfect absorption is thus obtained. MIM stack structure (Ag-Multilayer-AR layer) were also used in Ref. 3, 4, to design a THz broad band PMA. Multilayer spheres [5], multilayered lumped elements [6-8], stacked grating layers [9] and tapered hyperbolic stack arrays [10-11], can be found in the literature to propose different bandwidth broadband PMAs for desired applications.

S. He et al. have proposed a stacked structure shaped as pyramid, which can totally absorb waves in the microwave regime [12]. Since the size of the metal-dielectric unit layers is gradually increased along the transverse direction so that a pyramidal shape is achieved, this type of structures is generally called pyramid absorber. As well known, their resonant frequency is dominated by the size of the absorber once the material and the thickness of each layer are fixed. As a consequence, in the pyramid absorber each unit layer corresponds to a certain resonant frequency and an ultra-wide band absorption can be achieved by superposition of multiple resonances with small frequency interval. Beside the microwave broadband absorber an infrared ultra-broadband absorber which can also be regarded as a pyramid structure, namely sawtooth structure was presented by Y. Cui in 2012 [13]. Following these two proposed ultra-broad band absorbers, many articles based on pyramid broadband absorbers in microwave, THz, infrared and visible regions have been published [14-19]. Nevertheless millimeter wave absorber as a potential application has not been involved in these works. Thus in this chapter we mainly focus on developing a pyramid-type broadband absorber operating in the millimeter wavelength region.

Firstly, a structure composed of a periodic array of quadrangular frustum pyramids with 13 metal-dielectric layers was designed and the influence of geometry and material properties on absorbance was studied in detail using HFSS. In the following we first design the structure by considering each elementary cell. More over a dispersion diagram and the resonant frequencies will be obtained by using eigenmode analysis. Both techniques (driven and eigenmodes methods) will be helpful for a better understanding about the absorption mechanism. A brief conclusion is given in the last section.

5.2 Design of the pyramid millimeter wave ultra-broadband absorber

Fig. 5.1 (a) shows a schematic of the absorber structure, which consists of a

periodic array of pyramids with a quadrangular cross shape and a homogeneous metal ground in the bottom, the latter blocking any transmission of the incidence wave (S_{21} = 0)). The reflection coefficient (S_{11}) is minimized by properly structuring the shaped stack with square-based pyramids, taking advantage of the symmetry of the structure to ensure insensitivity to polarization. Each resonator is made of a stack metal and dielectric layers with respective thickness d_m = 15 μm, d_g = 35 μm (Fig. 5.1 (c)). Their operation was explained in section 1. 3.2. The metal is gold with the electric conductivity assumed to be $\sigma = 4\times10^7$ S/m. Germanium is used for the dielectric spacers with relative permittivity and loss tangent equal to 16 and 0.025, respectively. Here, 13 resonator layers are chosen.

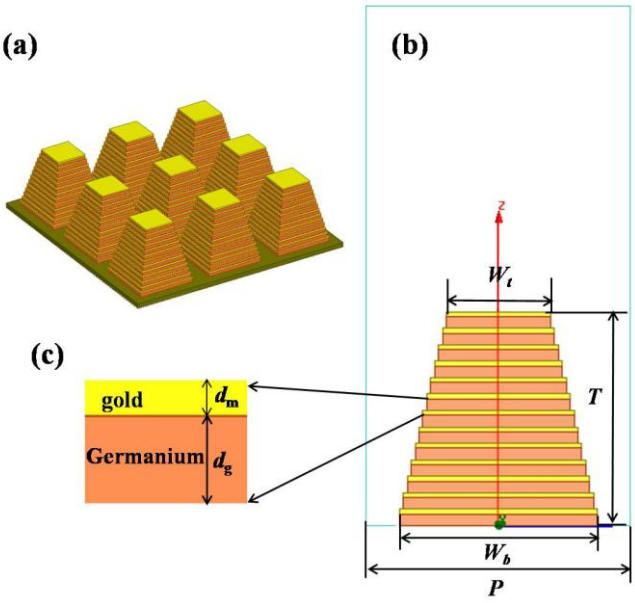

Fig. 5.1 Design of a millimeter wave ultra-broadband PMA, (a) 3-D illustration of the simulation PMA in periodic array, (b) schematic of a PMA unit cell, and (c) zoomed view of the sub-elemental cell.

In the simulation, periodic boundary condition is satisfied along the *x* and *y* direction and an incident, plane wave is launched along the *z* direction with ***E*** field polarized along the *y* direction. Absorption is calculated as $A = 1- R(|S_{11}|^2) - T(|S_{21}|^2)$. Owing to the metal ground, *T* equals to 0. The absorption and reflection coefficients as a function of frequency from 50 GHz to 150 GHz were shown in Fig. 5.2. There

exist 12 absorption peaks with absorbance above 90%, corresponding to the number of dielectric patches between two neighboring metal interfaces. Full width at half maximum (FWHM) is used to describe the absorption performance of such a PMA along with the central frequency so that a fractional bandwidth (FB) can be defined as FB =.$\Delta f/f_c$. FB equals to 72.3% for the designed PMA shown in Fig. 5.2, which thus exhibits excellent absorption performance.

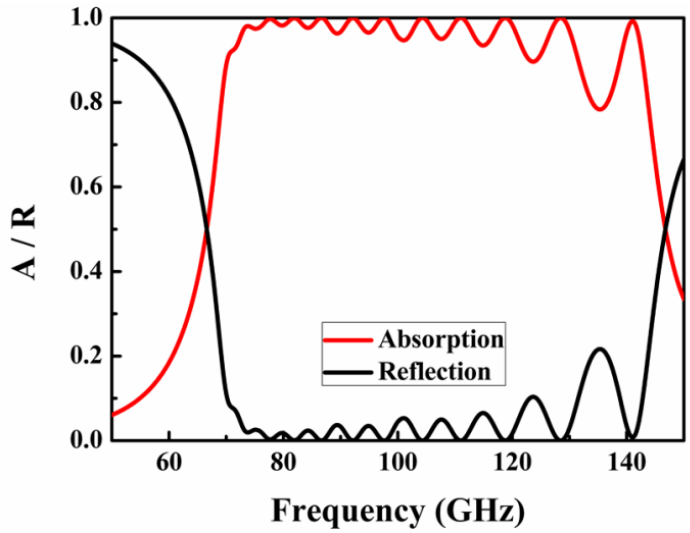

Fig. 5.2 Absorption and reflection curves with the dimensions of a unit are W_t = 0.315 mm, W_b = 0.6 mm , P = 0.8 mm, T = 0.65 mm, d_m = 15μm, d_g = 35μm.

To physically explain the origin of resonance effects of the ultra-broadband PMA, electric and magnetic field distribution are plotted at three frequencies (77.85, 118.9 and 141.2 GHz) as shown in Fig. 5.3.

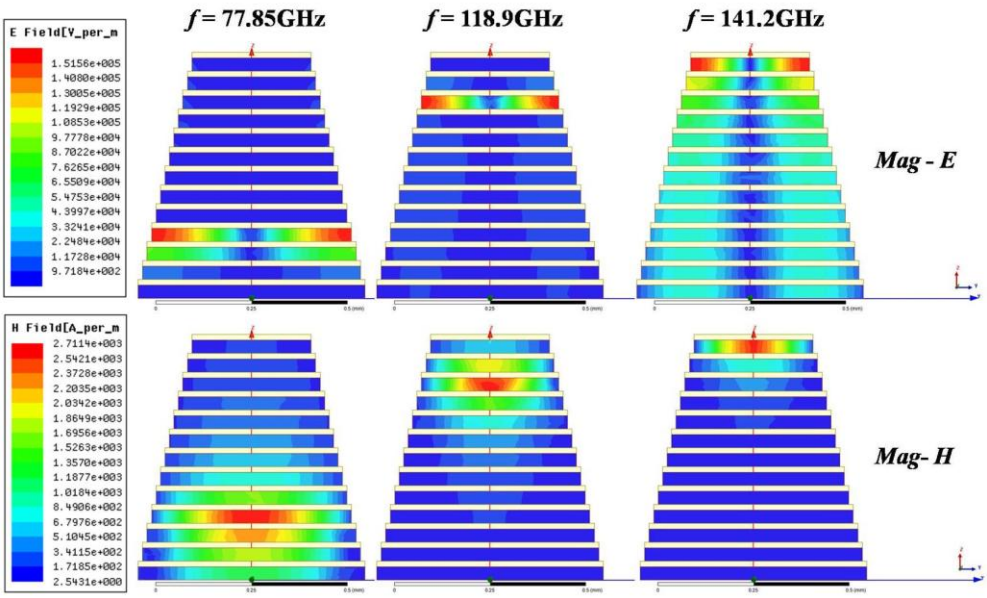

Fig. 5.3 Simulated electric and magnetic amplitude distributions at the central cross section of a unit cell in *y*-*z* plane at three resonance frequencies.

In this figure it is shown that the electromagnetic field is localized inside the dielectric layers at the relevant resonance frequency. Two adjacent metal layers spaced with a dielectric layer can localize the electric and magnetic field at special frequencies. Such resonances lead to zero-reflection and thus unit absorption is obtained by impedance matching to the free apace. At lower frequencies the electromagnetic field is localized at the bottom pyramid layers. As the frequency is increased, the electromagnetic field is localized in the top pyramid layers. As the pyramids absorbers gradually decrease in width from the bottom to the top, they resonate at different frequencies. Since the resonance frequencies of neighboring resonators overlapping to each other, this results in an ultra-broadband absorption.

5.2.1 Parametric analysis

In order to optimize the structure, we now turn to the study of the influence of the geometrical parameters such as period, thickness of metal and dielectric,

transverse dimensions of the resonators and number of layers. Also the material properties, particularly the imaginary part of the insulating layer which governs the dielectric absorption and the conductivity of metal films will be considered.

Geometrical parameters influence

Fig. 5.4 shows the absorption coefficient as a function of frequency for four periods ranging from 0.7 mm to 1.0 mm. Just to remind that in this simulation we kept the other parameters constant as used above, by only varying the period *P*. From this figure, it can be noted that there is an optimized period here *P* = 0.8 mm, and that the period have more influence at higher frequencies.

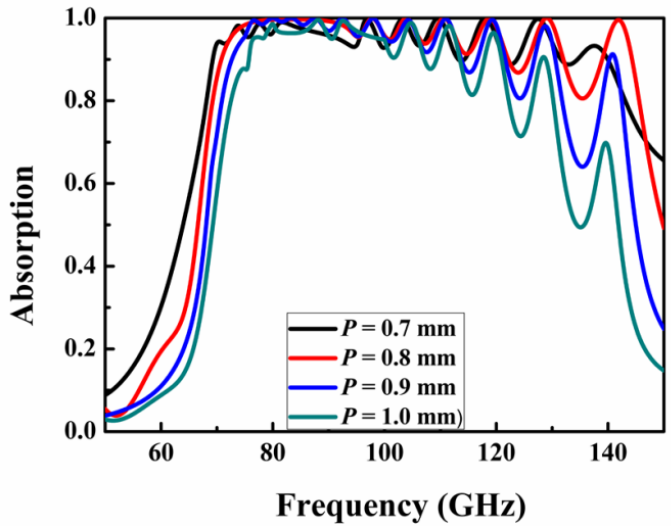

Fig. 5.4 Absorption coefficient with respect to frequency for four periods ranging from 0.7 mm to 1.0 mm.

The results of Fig. 5.5 (a) were obtained by keeping the thickness of metal as 15 μm constant and by varying the thickness of the dielectric layer from 15 μm to 55 μm, corresponding to ratio t_d/t_m of 1, 3/5, 3/7, 3/9 and 3/11 respectively.

Fig. 5.5 (b) gives the results of simulation by keeping the thickness of dielectric as 35 mm constant and by varying the thickness of the metal layers ranging here from 5 μm to 25 μm, which means ratio t_m/t_d ranging as 1/7, 2/7, 3/7 4/7 and 5/7. From this

figure, it can be noticed that the two parameters have more influence in the higher frequency, and that the thickness of dielectric plays a more important role with respect to the performance of ultra-broadband absorbers. We can find an optimized ratio t_m/t_d = 3/7 with t_m =15 μm, t_d =35 μm.

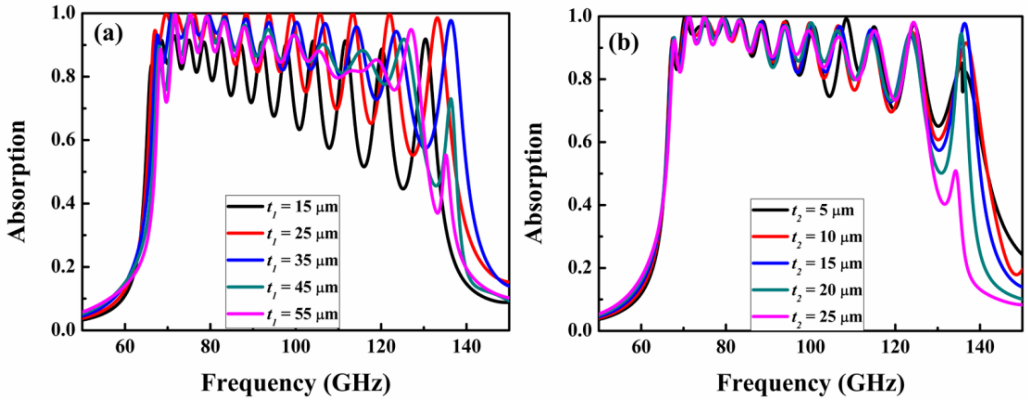

Fig. 5.5 Absorption coefficient with respect of frequency (a) for thickness of dielectric t_1 from 15 μm to 55μm while t_2 =15 μm constant, (b) for thickness of metal t_2 varied from 5 μm to 25 μm while t_1=35 μm constant.

Fig. 5.6 (a) shows the absorption spectra when the transverse dimension W_b was varied as 0.5 mm, 0.6 mm and 0.7 mm, by keeping W_b /P = 3/4 and the length difference between two adjacent resonators is kept constant as 9/380 m constant. As interpretation of Fig. 5.3 it can be concluded that the transverse dimensions govern the operating frequency with Fabry Perot type resonance condition in $l = \lambda_g/2$, where λ_g is the guided resonance wavelength, l is the transverse For example, when W_b = 0.6 mm, $f_r = c/(2W_b\sqrt{\varepsilon_r})$ = 62.5 GHz which is fixed as the first resonance frequency in Fig. 5.6(a) red line. It is also found that when the transverse bottom dimension increases the bandwidth window shifts towards lower frequency. It can be seen that as W_b is reduced, FB is increased. However, W_b cannot be too large, otherwise the width of neighboring metal patches in a unit will vary too abruptly. As a consequence the frequency difference between their supported resonant modes becomes too large and pronounced oscillation forms will appear in the absorption spectra. To conclude the

transverse dimension of resonator patches impacts dramatically the resonant frequencies and their variations has to be sufficiently gradual to avoid a multi-peak absorption spectrum rather that a low ripple broadband absorption window.

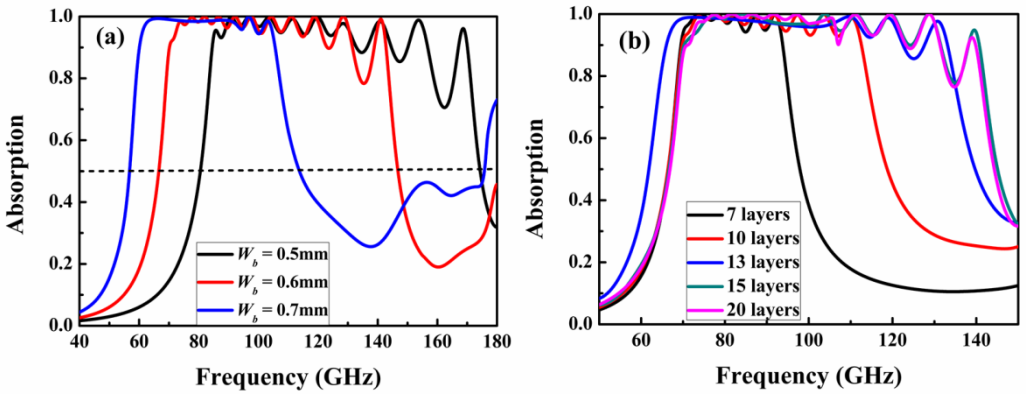

Fig. 5.6 Absorption coefficient with respect of frequency (a) for bottom lengths W_b ranging as 0.5 mm, 0.6 mm and 0.7 mm, (b) with different number of resonator layers ranging as 7, 10, 13 and 15 layers.

Fig. 5.6 (b) shows the absorption spectrum when the number of resonator layers is varied. In this simulation, the bottom length W_b = 0.6 mm, the difference length between two adjacent layer was kept constant as 9/380 mm. The number of layers varies from 7 to 20. One can see that, as the number of layer increases, the absorption window broadens gradually with however no significant improvement in the bandwidth for large number of resonators such as N = 20. Owing to the increasing difficulty to realize practical structure we limit the number of layers to 13 in our design.

Material properties influence

Fig. 5.7 summarizes the results of the study of the influence of the material parameters, Fig. 5.7 (a) shows the absorption spectrum by varying the loss tangent of the dielectric layer from 0 to 0.1. It is found that the introduction of higher losses broadens each elementary peak and thus increases the overall absorption bandwidth by increasing the imaginary part of relative permittivity.

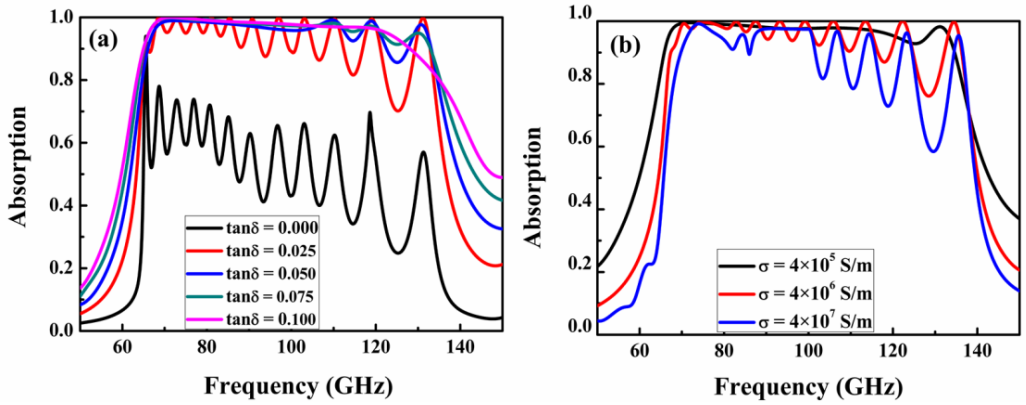

Fig. 5.7 Absorption coefficient with respect to frequency, (a) under influence of dielectric loss tangent varying from 0 to 0.1, (b) under influence of metal conductivity ranging from 4×10^5 S/m to 4×10^7 S/m.

Fig. 5.7 (b) shows the absorption spectrum as the conductivity of metal is varied from 4×10^5 S/m to 4×10^7 S/m, the latter value corresponding to the conductivity of a metal film such as copper or aluminum. There are similar effects with those observed by varying the dielectric losses with improved absorption qualities associated with the decrease of conductivity.

5.2.2 Dispersion diagram analysis

For a deeper understanding of the physical phenomena responsible of the absorption properties, the dispersion characteristic as a function of k vector (k_z) were calculated by means of the Eigenmode Solver of the HFSS numerical code.

Firstly, dispersion curves of separate resonators were calculated when the Bloch mode propagates along the z direction. Fig. 5.8 shows the diagram achieved with these simulation conditions.

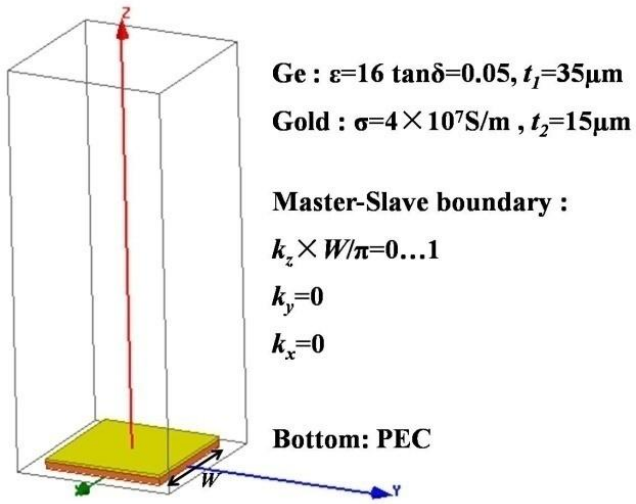

Fig. 5.8 Simulation domain used for the dispersion calculation.

The dispersion curves when W is varied as 0.3, 0.4, 0.5 and 0.6 mm respectively, are shown in Fig. 5.9 (a) along with the corresponding absorption lines displayed in Fig. 5.9 (b). The highly localized resonance frequency f_c = 65 GHz for W = 0.6 mm, 83 GHz of W = 0.5 mm, and so on, are found in agreement with the peak absorption frequencies deduced from the scattering parameters calculations (Fig. 5.9 (b)). When incidence wave frequency is near f_c, the Bloch mode is a slow wave that is trapped in the PMA structure. Due to the loss of gold and germanium the incidence wave then strongly absorbed at the resonance frequency.

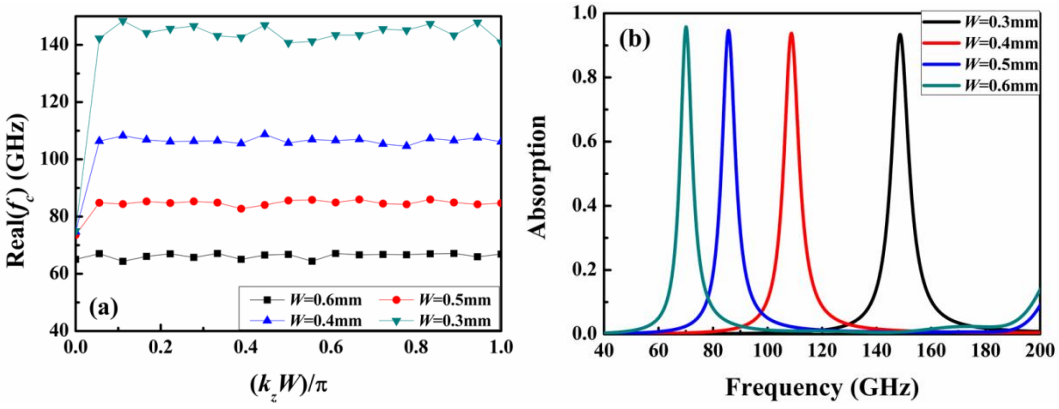

Fig. 5.9 (a) dispersion curves when W varied as 0.3, 0.4, 0.5 and 0.6 mm, (b) corresponding absorption lines.

Using the same calculation method in Fig. 5.8, the dispersion diagrams were studied for the pyramidal PMA. Calculation results are shown in Fig. 5.10.

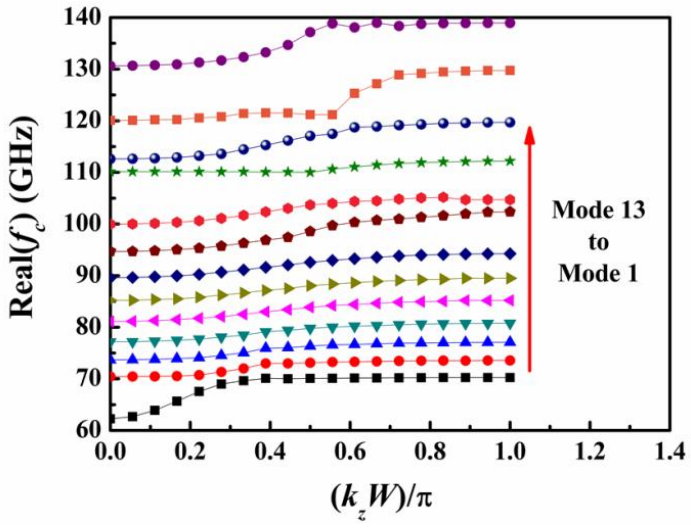

Fig. 5.10 Dispersion curves of the pyramid PMA.

As the widths of the pyramid-shaped layers decrease gradually from bottom to the top, the resonance frequencies vary from 65 GHz to 140 GHz in agreement as shown in Fig. 5.10, with the local resonance modes. As a consequence a broadband absorption of 65 – 140 GHz can be obtained.

5.3 Conclusion

In summary, we numerically demonstrated that 13 metal-dielectric layers staked in periodic arrays and shaped as quadrangular frustum pyramids can realize ultra-broadband PMA with a fractional bandwidth equals to 72.3 %. After properly designing the multilayered structure, the geometrical and material parameters influences were assessed to optimize the absorption quality. Moreover a dispersion diagram by using eigenmode analyze method, which is helpful for a better understanding about the absorption mechanisms, has been investigated.

References

[1] J. Sun, L. Liu, G. Dong and J. Zhou, An extremely broad band metamaterial

absorber based on destructive interference, Opt. Express, Vol. 19, 21155-21162, 2011.

[2] H. Xiong, J. Hong, C. Luo and L. Zhong, An ultrathin and broadband metamaterial absorber using multi-layer structures, J. Appl. Phys., Vol. 114, 064109, 2013.

[3] T. Corrigan, D. Park, H. Drew, S. Guo, Paul W. Kolb, W. Herman and R. Phaneuf, Broadband and mid-infrared absorber based on dielectric-thin metal film multilayers, Appl. Opt., Vol. 51, 1109-1113, 2012.

[4] P. Zhu and L. Guo, High performance broadband absorber in the visible band by engineered dispersion and geometry of a metal-dielectric-metal stack, Appl. Phys. Lett., Vol. 101, 241116, 2012.

[5] D. Kim, D. Kim, S. Hwang and J. Jang, Broadband terahertz absorber realized by self-assembled multilayer glass spheres, Opt. Express, Vol. 20, 13566-13572, 2012.

[6] J. Wang, C. Fan, Pei Ding, J. He, Y. Cheng, W. Hu, G. Cai, E. Liang and Q. Xue, Tunable broad-band perfect absorber by exciting of multiple plasmon resonances at optical frequency, Opt. Express, Vol. 20, 14871- 14878, 2012.

[7] B. Wang, S. Liu, B. Bian, Z. Mao, X. Liu, B. Ma and L. Chen, A novel ultrathin and broadband microwave metamaterial absorber, J. Appl. Phys., 116, 094504, 2014.

[8] B. Wang, L. Wang, G. Wang, W. Huang and X. Zhai, Broadband, polarization-insensitive and wide-angle terahertz metamaterial absorber, Phys. Scr., Vol. 89, 115501, 2014.

[9] J. Wu, C. Zhou and J. Yu, TE polarization broadband absorber based on stacked metal-dielectric grating structure, Opt. Commun., Vol. 341, 85-90, 2015.

[10] J. Zhou, A. F. Kaplan, L. Chen and L. Jay Guo, Experiment and Theory of the Broadband Absorption by a Tapered Hyperbolic Metamaterial Array, ACS Photonics, Vol. 1, 618-624, 2014.

[11] D. Ji, H. Song, X. Zeng, H. Hu, K. Liu, N. Zhang and Q. Gan, Broadband absorption engineering of hyperbolic metafilm patterns, Sci. Rep., Vol. 4, 4498, 2014

[12] F. Ding, Y. Cui, X. Ge, Y. Jin and S. He, Ultra-broadband microwave metamaterial absorber, Appl. Phys. Lett., Vol.100, 103506, 2012.

[13] Y. Cui, K. Fung, J. Xu, H. Ma, Y. Jin, S. He and N. X. Fang, Ultra broadband light absorption by a saw tooth anisotropic metamaterial slab, Nano Lett., Vol.12, 1443-1447, 2012.

[14] M. Lobet, M. Lard, M. Sarrazin, O. Deparis and L. Henrard, Plasmon hybridization in pyramidal metamaterials: a route towards ultra-broadband absorption, Opt. Express, Vol. 22, 12678-12690, 2014.

[15] Q. Liang, W. Yu, W. Zhao, T. Wang, J. Zhao, H. Zhang and S. Tao, Numerical study of the meta-nano pyramid array as efficient solar energy absorber, Opt. Mater. Express, Vol.3, 1187-1196, 2013.

[16] Q. Liang, T. Wang, Z. Lu, Q. Sun, Y. Fu and W. Yu, Metamaterial-based two dimensional plasmonic subwavelength structures offer the broadest waveband light harvesting, Adv. Opt. Mater., Vol. 1, 43-49, 2013.

[17] J. Zhu, Z. Ma, W. Sun, F. Ding, Q.He, L. Zhou and Y. Ma, Ultra-broadband terahertz metamaterial absorber, Appl. Phys. Lett., Vol. 105, 021102, 2014.

[18] J. Zhou, A. F. Kaplan, L. Chen and L. J. Guo, Experiment and theory of the broadband absorption by a tapered hyperbolic metamaterial array, ACS Photonics, Vol.1, 618-624, 2014.

[19] Y. J. Kim, Y. J. Yoo, K. W. Kim, J. Y. Rhee, Y. H. Kim and Y. P. Lee, Dual broadband metamaterial absorber, Opt. Express, Vol. 23, 3861-3866, 2015.

Chapter 6 Wave controlling device: the example of a woodpile structure

6.1 Introduction

The main topic which was addressed all along the previous chapters concerns the realization of low-profile perfect absorbers. In particular, it was shown that metamaterial technology by structuring either full dielectric structure with high permittivity (ferroelectric) components or metal/low permittivity dielectric/metal tri-layer enable total absorbance metasurfaces to be manufactured. In this chapter, we are considering additional functionality by also considering from the technological side the possibility of prototyping by means of the so-called 3D printing technology. This study will be conducted by considering the so-called woodpile electromagnetic band gap. This structure was subsequently fabricated by additive fabrication technique and experimentally assessed by vector analysis in free space. By this preliminary experimental study of a band gap structure, supported by numerical analysis, it will be shown the possibility to tailor locally the constitutive parameters (in the case of a wood pile structure the effective permittivity). In a second stage, we will discuss more generally how to design low profile phase front controlling devices.

6.2 Primary results of woodpile structures

Artificial materials on the scale of wavelength, namely photonic bandgap (PBG) structure, exhibit many new features or give many freedoms in the improvement of their Electro-Magnetic (EM) properties [1-3]. Since this kind of metamaterials can manipulate the propagation of EM waves [4], it can be widely used for designing optical devices such as invisibility cloaks, novel lens and field rotators [5-8].

In this general context, we show here the potential of 3D printing techniques to fabricate full dielectric 3D woodpile photonic crystal structures, composed of

thermoplastic polymer (ABS) square rods with permittivity ε_r=3, reproduced in three directions with a constant period as shown in Fig. 6.1 (left). From the numerical point of view, by calculation of complex transmission and reflection coefficients of the sample, we access a complete gap in the millimeter wave band (V band) with a fraction bandwidth of about 20%. By considering the long wave length regime, it is shown the possibility to modulate the value of the effective index by varying the Bragg gap cutoff frequency through modification of a relevant dimension of the sample. After the prototype was 3D printed, the transmission coefficient was measured in free space for assessing the existence of a forbidden gap in the transmission spectrum.

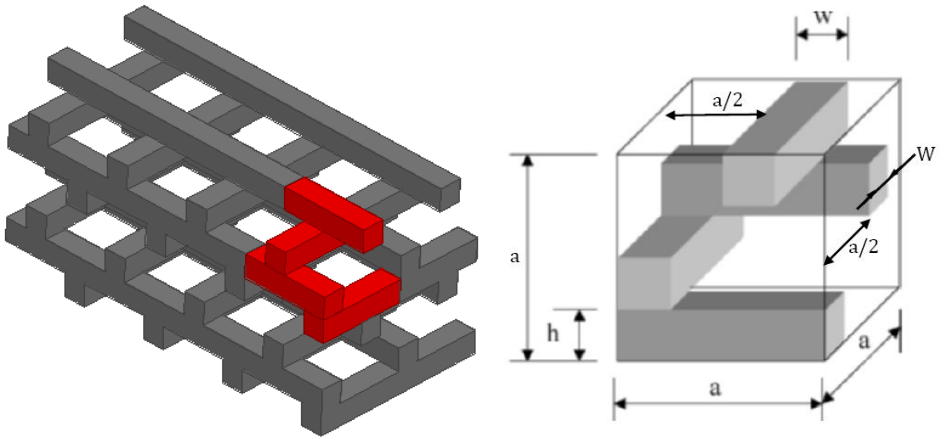

Fig. 6.1 Schematic of woodpile photonic crystal structures (left), diagram of the super-unit cell (right).

Fig. 6.1 (right) shows a schematic of the unit cell. It consists of a periodic arrangement of dielectric rods stacked in three directions by alternating the directions of alignment layer by layer. In the following we chose a period a =2.5mm.The height of the rods (h) is also taken constant with a value equal to 1.25 mm constant, while the side width (w) of the dielectric rods is considered as an adjustment variable parameter to realize gradient index metasurfaces.

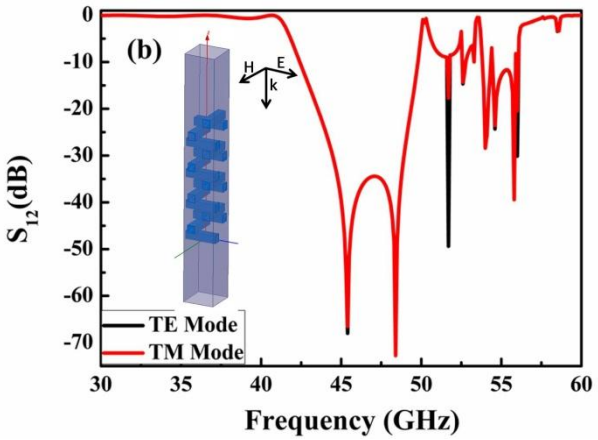

Fig. 6.2 The transmission spectrum of *k* along the direction parallel to the stacking(16 rods) direction, with *w* = 1.25mm, for *TE* and *TM* modes, respectively, insert is the simulation schematic with the Master and Slave period boundary conditions.

In Fig. 6.2, we plotted the results of the frequency dependence of the magnitude of transmittance S_{12} by means of the HFSS software. As expected, a deep rejection (Bragg band gap) can be noted in this figure roughly between 42 GHz and 50 GHz. The fractional bandwidth is around 20%. Owing to the symmetry in the orientation of alternating rods, the structure is found insensitive to polarization. These first simulation results performed for a constant value *w* = 1.25 mm shows the existence of a gap whose cut-off frequencies are directly related to the period of the rod array. The question is to know whether these frequencies that define the band where the wave propagation is forbidden, can be structurally tuned by varying the width *w*, while keeping constant the height *h* of the dielectric rods. By such a parametric study on the parameter w, we aim to design a gradient lens by a *local* modulation of the effective index that is adjusted by the sole variation of *w*, while maintaining the height *h* constant.

Fig. 6.3 shows the modulation of effective index transmission coefficient as a function of the frequency for *w* varying from 0.25 mm to 1.25 mm.

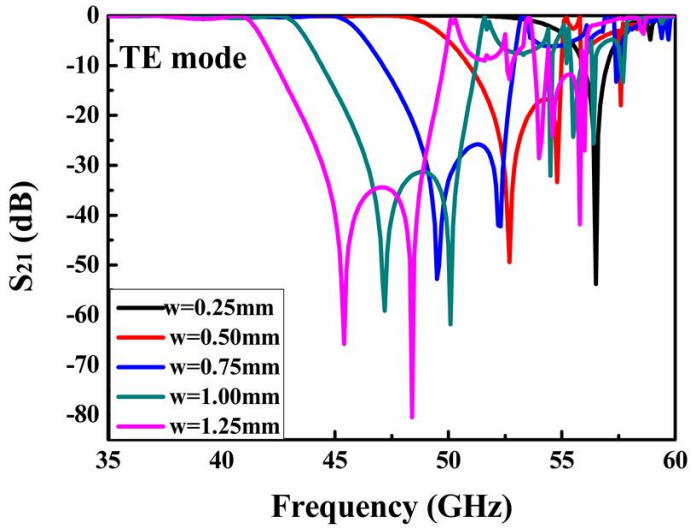

Fig. 6.3 Transmission spectra for incident *k* vector parallel to the stacking direction for *TE* mode, for rods widths *w* varying from 0.25 mm to 1.25 mm.

From Fig. 6.3, it can be seen that as *w* increases, subsequently the cutoff frequencies of the band gap decrease. For instance the low frequency cut-off increases from about 42 GHz to 49 GHz by decreasing *w* from 1.25 mm down to 0. 5 mm. Further decreasing *w* yields a higher frequency shift but at the detriment of the band gap that shows only one peak and thus a narrow forbidden frequency band.

Such a modulation of the low frequency cut-off is the underlying idea of a modulation of the effective index in the long wavelength regime. This condition is met namely in the low frequency pass band in contrast to the stop band for which the wavelength are comparable to the relevant dimension. By neglecting the dispersion effect and thus assuming a linear variation of the angular frequency versus k vector in the dispersion diagram, it is straight ward to demonstrate that the effective index can be estimated from the following approximation:

$$n = \frac{c}{2f_{c1}a}$$

Where c is the speed of light, f_{c1} is the low frequency cut-off and a is the period

Application of the above formula gives a propagation velocity of 2×10^8 ms^{-1} for a cut off frequency of 40 GHz corresponding to an effective index of 1.5 while for f_{c1} = 50 GHz gives a value of 1.2 for the effective index.

In practice, the prototype was fabricated by using 3D printer HP design jet, using ABS polymer. The print volume is 655cm^3 with a maximum height of 153mm. The maximum resolution is 250 μm, which can be in principle sufficient for satisfying the minimum side width *w* (here taken as variable) of the structure. The deposition technique is based on FDM (Fuse Deposition Method) type. The rods were sequentially stacked and bonded starting from the bottom layer by thermal heating.

Fig. 6.4 (a) shows a photograph of a prototype of five unit cells corresponding to the alternation of 20 sub-structured layers for *w*= 1.25 mm . Layer by layer the rods are translated of *a*/2 and their axes are reoriented of 90 °. Fig. 6.4 (b) gives the zoomed view of one of the structured surface. The visual inspection of the prototype confirms the periodic arrangement of the rod array without important defects such as clogged structures. ABS polymer residues are however visible on the finished demonstrator.

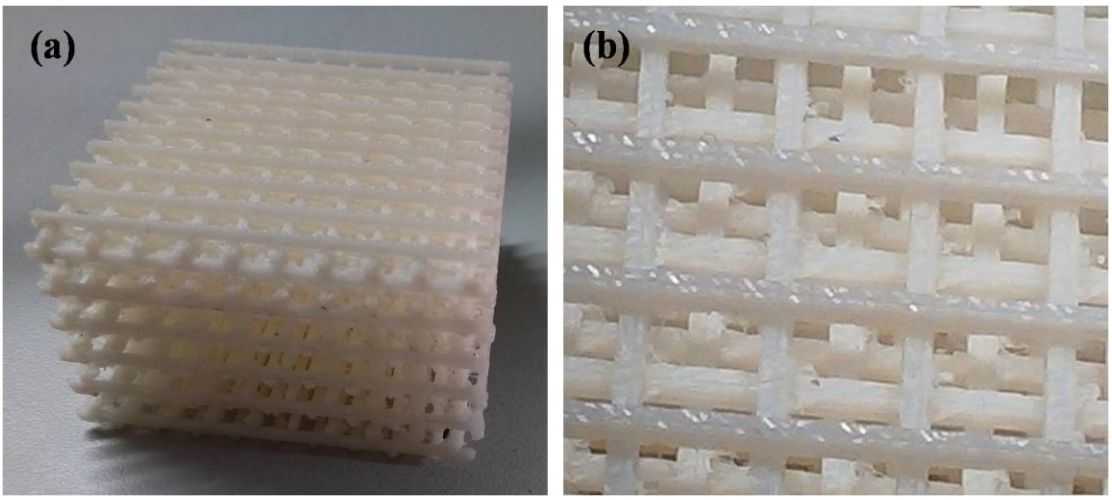

Fig. 6.4 Photograph of the prototype(a), details of the alternating structure(b).

The characterization of the structures was carried out in free space using a vector network analyzer. This technique is similar to the one we used for the characterization of negative refraction including tensor aspects [5] and the measurement setup was

shown in Fig. 6.5. In addition the sample was surrounded by Ecosorb AN77 absorbing foams in order to limit the influence of parasitic reflections.

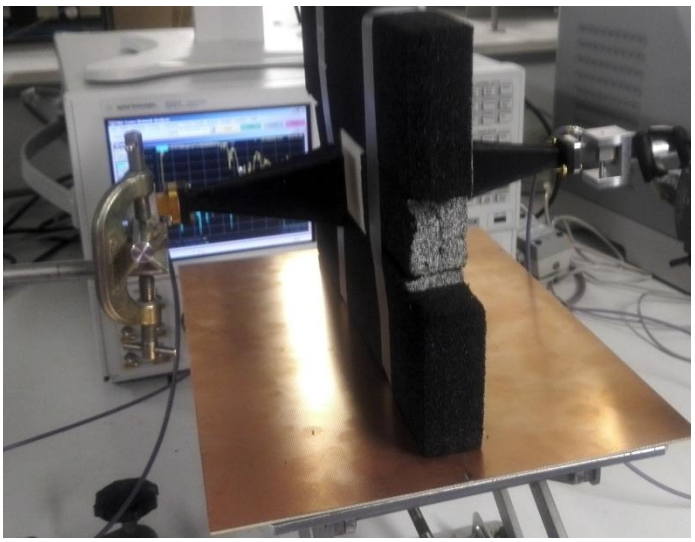

Fig. 6.5 Photograph of the free-space set up of vector network analysis in V-band

Fig. 6.6 displays the transmission coefficients which were measured with and without the sample inserted across the EM wave beam. S_{21}_Ref was the transmission coefficient measured without sample by using two rectangular horns operating in the frequency band 20-70 GHz. In this configuration a flat transmission is achieved up to around 45 GHz with a transmission level around -5 dB. Above this frequency, and hence out of the band of the dominant mode of the horns, the transmission coefficient is lower that the reference of -5 dB and exhibit multi peak spurious resonances. The transmission coefficient measured by inserting the woodpile structure under test is labeled S21_sample. At low frequency and hence in the pass band the transmission level is of the same order of magnitude than the one previously obtained without the sample. At higher frequencies a deeper rejection is noted with respect to the mean level of the transmitted signal without the sample.

The measured transmission level of the woodpile structure achieved by subtracting the reference and labeled Sample-S21_Reference is finally plotted in this figure and compared with the numerical results. Only a qualitative agreement is

achieved notably for the rejection of the transmitted signal in the band gap. From the point of view of cut-off frequencies, they are comparable at least for the lowest one. For the upper frequency of the band gap, a comparison between measured and calculated data is more problematic. Any way it appears that an experimental confirmation of the existence of a forbidden gap in the transmission was pointed by these first measurements, opening the way to modulate the effective index by varying the width of the rods *w*. It is believed however that further experimental effort has to be devoted in the future to specific measurements in the high frequency part of the transmission spectrum. In particular the use of dominant mode circular horns operating in the V band associated with improvement of the quality of the probing Gaussian beam should provide a better understanding of the underlying physical effects.

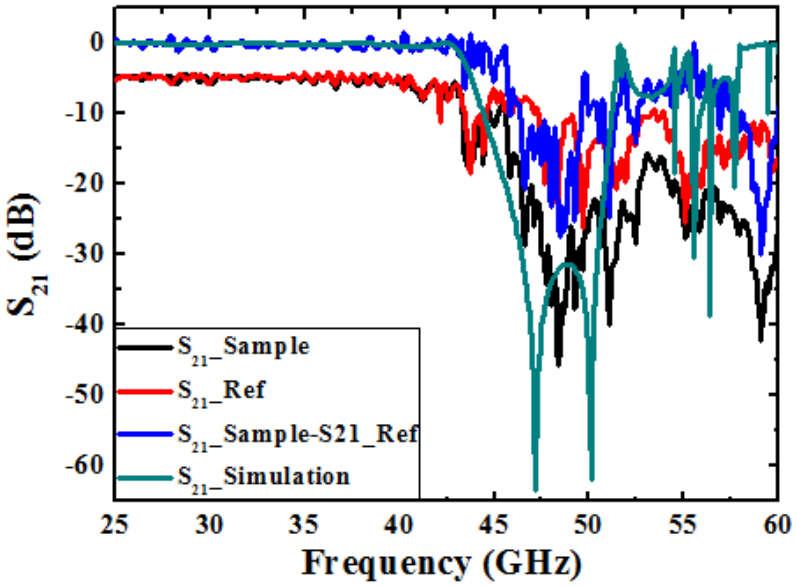

Fig. 6.6 Transmission coefficients S21_Sample of measuring with sample, S21_Ref of without sample, for incidence wave impinge parallel to the stacking direction.

6.3 Discussion about GRIN lens

In this section, we consider more generally the various solutions to control the phase front of an incident para-axial electromagnetic wave with the requirement to

preserve a low thickness of the device. From the previous section devoted to the electromagnetic properties of 3 D printed wood pile structure, it was shown that some index variation can be introduced by width variation of the dielectric rods that make up the artificial composite material. Far from the forbidden gap and hence in the long wavelength regime the structures is non-resonant. As a consequence an analysis on the basis of simple mixing laws can predict the average value of the permittivity in the effective medium approximation. The two components are air and ABS with a permittivity around 2.2 for ABS as experimentally assessed in our characterization of the dielectric dispersion of this thermoplastic carried out by Transient Time Domain (TDS) spectroscopy [9]. In terms of refractive index value this means that variations between 1 and ~ 1.5 can be introduced locally. Such a difference appears quite suitable for manufacturing conventional GRIN lens but seems limited if high numerical aperture gradient index lens are targeted. The aforementioned arguments raise the following question: how to increase the difference between the edge and the core index values of a graded index lens so that an efficient curvature of the phase front can be introduced by means of local index engineering. For solving such a difficulty, a possible solution is to increase the relative permittivity of the background substrate. By this means any variation of the filling factor between air- and basic- cells made of this high permittivity material increase dramatically the index difference [10]. If this solution seems natural and simple in its implementation, the practical realization of such composite structures seems much more problematic notably in the current context of additive technology.

Beyond the mixing concepts another way to increase this difference seems, here again, to exploit resonance effect and more particularly artificial magnetic response in composite structures comparable to those described in the first chapters of this thesis. However in contrast to perfect absorber the idea is to transmit totally or with minimum losses an incident wave impinging a resonator tailored locally in order to fit a predefine gradient index profile;

As before, manipulating the phase front requires from an application point of view to minimize as far as possible the return losses by simultaneously optimizing the transfer of the incident wave from the input to the output sections. The critical coupling criteria as pointed out in Chapter 2 and 3 for total absorber made of BST cubes or MIM microstructures with the balance between coupling and dissipation quality factor should be applied as well.

6.4 Conclusion

To summarize, a preliminary numerical study of a wood pile microstructure that exhibits a forbidden gap (stop band) in the V band of the millimeter wave spectrum was reported. This theoretical work showed the possibility to tailor the value of the refractive index in the pass band by varying the dimension of dielectric pillars that are configured in a wood pile scheme. Some samples were manufactured subsequently by additive fabrication technique (3D printing technology) by using the thermoplastic ABS whose dielectric losses are moderate in this frequency band. As expected high transmissivity was measured in the low frequency pass band and the existence of the forbidden gap was pointed out above 40 GHz. A first analysis is reported in connection with the possible variation of the index through the offset of the Bragg cut off frequencies. In a last section, we discussed some of the solutions that can be implemented to design low profile gradient index lens with a high numerical aperture.

References

[1] K. M. Ho, C. T. Chan, C. M. Soukoulis, R. Biswas and M. Sigalas, Photonic band gaps in three dimensions: new layer-by-layer periodic structures, Solid State Commun., Vol. 89, 413-416, 1994.

[2] E. Ozbay, A. Abeyta, G. Tuttle, M. Tringides, R. Biswas, C. T. Chan, C. M. Soukoulisand K. M. Ho, Measurement of a three-dimensional photonic band gapin a crystal structure made of dielectric rods, Phys. Rev. B, Vol. 50, 1994.

[3] B. Gralak, M. de Dood, G. Tayeb, S. Enoch and D. Maystre, Theoretical study of photonic band gaps in woodpile crystals, Phys. Rev. E, Vol. 67, 066601, 2003.

[4] I. Ederra, J. C. Iriarte and R. Gonzalo, Surface waves of finite size electromagnetic band gap woodpile structure, PIER B, Vol. 28, 19-34, 2011.

[5] M. Yin, X. Tian, L. Wuand D. Li, A Broadband and omnidirectionalelectromagnetic wave concentrator with gradient woodpile structure, Opt. Express, Vol. 21, 19082, 2013.

[6] Y. Urzhumov, N. Landy, T. Driscoll, D. Basovand David R. Smith, Thin low-loss dielectric coatings for free-space cloaking, Opt. Letters, Vol. 38, 1606-1608, 2013.

[7] M. Yin, X. Tian, L. Wu and D. Li, All-dielectric three-dimensional broadband Eaton lens with large refractive index range, Appl. Phys. Lett., Vol.104, 094101, 2014.

[8] Z. Wu, R. England, C. Ng, B. Cowan, C. McGuinness, C. Lee, M. Qiand and S. Tantawi, Coupling power into accelerating mode of a three-dimensional siliconwoodpile photonic band-gap waveguide, Phys. Rev. ST Accel. Beams, Vol. 17, 081301, 2014.

[9] F. Garet, V. Sadaune, J. L. Coutaz and D. Lippens, Impression 3D : Dispersion de la permittivité de l'Acrylonitrile Butadiène Styrène (ABS) aux fréquences Térahert, Proceeding of the Journées caractérisation des matériaux micro-ondes, Calais 2016.

[10] F. Gaufillet and É. Akmansoy, Design and experimental evidence of a flat graded-index photonic crystal len, J. Appl. Phys. Vol. 114, 083105, 2013.

Conclusions and Prospects

In this thesis, we studied the possibility to broaden the absorbance bandwidth of Perfect Metamaterial Absorbers by considering first ferroelectric resonators arrayed on a metallic plate suppressing by this way any transmitted wave and in a second stage plasmonic-type structures consisting of periodically patches printed on a grounded dielectric layer.

With respect to the first technological route exploiting high κ full dielectric resonators, the conditions of total absorbance was first established by pointing out the requirement of a balance of the quality factors that depict the radiation and the intrinsic losses. The former is directly related to the period while the latter depends on the loss tangent of the dielectric layer. For Ferroelectric dielectric layer with permittivity in excess of 100 and loss tangent around 2 %, it was thus found that ferroelectric cubes with a side around 2 mm resonates at X band (8-12 GHz for a dominant mode). The selectivity of this resonance that allows the achievement of a unit transmission can be estimated as a few percent of fractional bandwidth. Further improvement was demonstrated via the idea to introduce a dispersion of the longitudinal dimension so that resonance frequency distribution can be introduced as the result of a modification of the current loop responsible of magnetic resonance. This engineering of one of the relevant dimension, by preserving the periodicity, was assessed experimentally via wave guide measurements. On the other hand, full distribution of the resonator dimension in the 3 directions of space shows an ultra-wide band by combining size and position dispersion.

The conclusion about the development of plasmonic-type structure whose generic structure consists in a bi-layered metal pattern sandwiched with a low permittivity layer (typically FR4 for a Printed Circuit Technology) shows the same magnetic resonance behavior than the one evidenced in Mie resonance–type structure. The main difference stems in the current loop responsible of the artificial magnetic, combining anti-parallel

conduction current on the metal patches (plate) and displacement current in the dielectric layer. Despite this difference in the underlying physic mechanisms, the electromagnetic behavior responsible of a unit absorbance window is quite comparable with the ferroelectric technology. Therefore magnetic resonance in X band is found for typically 10 mm diameter patch and FR4 layer thickness of the order of 1 mm. Here again, with a disorder in position it was pointed a dramatic improvement between 3 and 4 of the absorbance bandwidth ensuring by the frequency shift of the electrical and magnetic dipole-dipole interactions. In addition at high filling factor it was found numerically and assessed experimentally a transition of a single absorption band to a multiple one, further broadening the absorption window. This transition attributed to the change between inductive and conductive coupling, has motivated the development of a four size super-cell absorber operating at millimeter wave. Due to this increase in frequency, the prototypes were fabricated by ink jet technology so that ultra-thin flexible absorbers were assessed experimentally by means of free space experiment in the 75-110 GHz frequency band. Also in this frequency band, the design of pyramidal stacks of multi-size absorbers was addressed by means of numerical simulations

The last part of this thesis is devoted to the preliminary study on the manipulation of the wave front by means of low profile lens. In contrast to absorbers for which the main performance relies on the achievement of a unit absorbance over the widest frequency band, high transmissivity has to be preserved in this case. As a consequence the criterion on critical coupling pointed out theoretically and experimentally has to be extended to meta-device with simultaneously minimum reflection and maximum transmission. From the technological side, special attention was paid on the possibility of using 3D printing technology for the realization of meta-surfaces. The device that was chosen to exemplify the possibilities afforded by this technology was the so-called wood pile technology. Successful realization of the structure was carried out with preliminary evidence of the stop band that start typically above 40 GHz by comparing simulation and experiment.

With respect to the main conclusions drawn above, the prospects of this research work are the following:

Targeting a broadband absorber, let us say one octave or even one decade over which an absorbance in excess of 90 % is achieved, it seems difficult to satisfy this criteria with single resonator array. We learned from the studies on random media that some disorder in position permits one to broaden significantly the width of the absorption window (typically a factor of three) on the other hand by keeping constant the relevant resonant dimension (in practice the diameter for ring shaped plasmonic resonator or the cube side for ferroelectrics absorbers). In addition, we showed that the thickness of the dielectric layer or the longitudinal dimension of BST cuboids can afford an extra degree of freedom for shifting the resonance frequency by a proper distribution of this dimension that can be consider as a new degree of freedom. The next step would be to continue in this direction for optimizing the absorption window by reminding that a critical coupling of the impinging energy has to be satisfied for unit absorbance through impedance matching. From the fabrication side, it is also worth-mentioning that implementing such height-distributed resonator is challenging. Some preliminary experimental demonstrations were reported in the framework of this thesis by taking benefit of the tolerance in the fabrication of BST resonators in the case of Giant Causey-like absorbers. Extending such a concept to plasmonic type structures whose fabrication is based on thin metal film technology, raises a number of additional difficulty requiring local thinning of the dielectric layer with post - printing of top metal layers.

The second orientation will concern the investigation of 2-D absorbers made of multi-layered MIM microstructures. The calculations of the absorbance spectrum of pyramidal-shaped structured dimensioned for operating at W-band have shown that such a development solution is very promising in terms of band. Again, the main difficulty stems from their practical realization. While no real difficulty is faced for operation at microwave frequency typically in X band with the Printed Circuit

Technology (PCB), the fabrication of such a structure is far to be trivial at terahertz frequency even in the lower part of the far infra-red spectral band. For the prospects foreseen in this field, it is believed that main efforts have to be brought to the development of technological processes by reminding that one of the main challenges of absorbing devices is the tradeoff between large area sample (in practice $A>>\lambda^2$) and subwavelength patterns ($d<<\lambda$). As a last comment, let us mention that multiplying the number of stack layer can raise the problem of flexibility that is sought for conformal absorbers.

The third orientation concerns the potential applications. Starting from the finding that one of the main limitations of the so-called invisibility devices is their narrow transparency bandwidth most of the studies reported here have concerned absorbing layers by suppressing any transmission of the absorber screen via a backside metallic plate. Despite the two technologies that were implementing namely metallic or high dielectric permittivity technologies, it appears that the underlying physical effects, which explain total absorption in the resonance band, are very similar. In particular the frequency dependence of the scattering parameter S_{11} shows zero reflection at the resonance frequency and total reflection out of absorption band. Zero reflection is achieved under the condition of a balance between the qualities factors that describes the energy escaping from the resonator (radiative quality factor Q_r) and the energy dissipated in the resonator (dielectric or metal losses $Q_{d,m}$). It is believed that this control of the impedance matching and thus of the zero reflection via Q_r and $Q_{d,,\mathrm{m}}$ can provide a means to adjust the total absorption frequency either by structural of material engineering or dynamically via for instance voltage-controlled ferroelectrics or liquid crystal technology. At last multi-functionality of the metal/dielectric/metal schemes can be foreseen by reminding that the so-called High Impedance Surfaces(HIS), that can be compared to the PMC (Perfect Magnetic Conductor) are fabricated from mushroom–type pillars arrayed on a metal plate.

List of publications

Journal:

[1] J. Hao, R. Niemiec, L. Burgnies, É. Lheurette, and D. Lippens, Broadband absorption through extended resonance modes in random metamaterials, J. Appl. Phys., Vol. 119, 193104, 2016.

[2] J. Hao, É. Lheurette, L. Burgnies, É. Okada and D. Lippens, Bandwidth enhancement in disordered metamaterial absorbers, Appl. Phys, Lett., Vol. 105, 081102, 2014.

[3] J. Hao, V. Sadaune, L. Burgnies, and D. Lippens, Ferroelectrics based absorbing layers, J. Appl. Phys., Vol. 116, 043520, 2014.

Conference:

[1] J. Hao, É. Lheurette, L. Burgnies, V. Sadaune, and D. Lippens Broadband metamaterial absorber based on random arrangement of metallic rings, GDR ondes 2015.

[2] J. Hao, É. Lheurette, L. Burgnies et D. Lippens Caractérisation des propriétés d'absorption de métamatériaux à arrangement aléatoire, 19èmes Journées Nationales Microondes -JNM Bordeaux 2-5 Juin 2015**.**

[3] G. Ducournau, J. Hao, C. Mismer, É. Lheurette, L. Burgnies and D. Lippens, Métamatériaux absorbants imprimés par jet d'encre et caractérisés en espace libre en bande W, 19èmes Journées Nationales Microondes -JNM Bordeaux 2-5 Juin 2015**.**

[4] V. Sadaune, J. Hao, L.Burgnies, É. Lheurette and D. Lippens, Couplage critique dans les métasurfaces à base de cubes ferroélectriques, 19èmes Journées Nationales Microondes -JNM Bordeaux 2-5 Juin 2015**.**

[5] V. Sadaune , J. Hao, E. Lheurette et D. Lippens, Matériaux artificiels structurés par

technique d'impression 3D, 19èmes Journées Nationales Microondes -JNM Bordeaux 2-5 Juin 2015.

[6] E. Lheurette, L. Burgnies, V. Sadaune, J. Hao, E. Okada and D. Lippens, Broadband Metamaterial Absorber Based On Random Arrangement of Barium Strontium Titanate Cubes , *The 8th International Congress on Advanced Electromagnetic Materials in Microwaves and Optics-Metamaterials*, Copenenhagen, Dermark, 25-30 August, 2014.

[7] J. Hao, L. Burgnies, M. Missner, G. Ducournau, E. Lheurette, D. Lippens, Bandwidth improvement of multi-scale metal resonators arrays in a coplanar configuration, *The 8th International Congress on Advanced Electromagnetic Materials in Microwaves and Optics-Metamaterials*, Copenenhagen, Dermark, 25-30 August, 2014.

[8] L. Burgnies, J. Hao, C. Mismer, G. Ducournau, E. Lheurette, D. Lippens, Métasurfaces absorbantes flexibles en ondes millimétriques, 13èmes Journées de Caractérisation Microondes et Matériaux, JCMM 2014.

[9] V. Sadaune, L. Burgnies, E. Lheurette, J. Hao, D Lippens, Métasurface absorbante parfaite à base de cubes ferroélectriques distribués aléatoirement13èmes, Journées de Caractérisation Microondes et Matériaux, JCMM 2014.

[10] J. Hao, V. Laur, A. Maalouf, V. Sadaune, L. Burgnies, J.L. Mattei, E. Lheurette, P. Queffelec et D. Lippens, "surfaces absorbantes très large bande à base de métamatériaux", *18èmes Journées Nationales Microondes*, Paris, France, 15-17 Mai, 2013.

[11] J. Hao, F. Zhang, V. Sadaune, L. Burgnies, E. Lheurette et D. Lippens, surfaces absorbantes à base de ferroélectriques, *18èmes Journées Nationales Microondes*, Paris, France, 15-17 Mai, 2013.

[12] J. Hao, V. Sadaune , L. Burgnies , E. Lheurette and D. Lippens, Ferroelectric

Metamaterial Perfect Absorber, *The Seventh International Congress on Advanced Electromagnetic Materials in Microwaves and Optics-Metamaterials*, Bordeaux, France, 16-19 September, 2013**.**